

REPORT DOCUMENTATION PAGE				Form Approved OMB No. 0704-0188	
Public reporting burden for this collection of information is estimated to average 1 hour per response, including the time for reviewing instructions, searching existing data sources, gathering and maintaining the data needed, and completing and reviewing this collection of information. Send comments regarding this burden estimate or any other aspect of this collection of information, including suggestions for reducing this burden to Department of Defense, Washington Headquarters Services, Directorate for Information Operations and Reports (0704-0188), 1215 Jefferson Davis Highway, Suite 1204, Arlington, VA 22202-4302. Respondents should be aware that notwithstanding any other provision of law, no person shall be subject to any penalty for failing to comply with a collection of information if it does not display a currently valid OMB control number. PLEASE DO NOT RETURN YOUR FORM TO THE ABOVE ADDRESS.					
1. REPORT DATE (DD-MM-YYYY) 05-03-2015		2. REPORT TYPE Final Report		3. DATES COVERED (From - To) 01-04-2012 - 31-03-2015	
Development of N- and P- Types of Semiconducting Polymers				5a. CONTRACT NUMBER	
				5b. GRANT NUMBER FA9550-12-1-0061	
				5c. PROGRAM ELEMENT NUMBER	
6. AUTHOR(S) Luping Yu				5d. PROJECT NUMBER	
				5e. TASK NUMBER	
				5f. WORK UNIT NUMBER	
7. PERFORMING ORGANIZATION NAME(S) AND ADDRESS(ES) Department of Chemistry, The University of Chicago, 929 E 57 th Street, Chicago, IL 60637				8. PERFORMING ORGANIZATION REPORT	
9. SPONSORING / MONITORING AGENCY NAME(S) AND ADDRESS(ES) AF OFFICE OF SCIENTIFIC RESEARCH 875 N. RANDOLPH ST. ROOM 3112 ARLINGTON VA 22203				10. SPONSOR/MONITOR'S ACRONYM(S) AFOSR	
				11. SPONSOR/MONITOR'S REPORT NUMBER(S)	
12. DISTRIBUTION / AVAILABILITY STATEMENT Approved for Public Release, Distribution is Unlimited					
13. SUPPLEMENTARY NOTES					
14. ABSTRACT In the past three years, our research project sponsored by AFOSR has been focused on developing low bandgap semiconducting polymers as both the donor and acceptor materials for BHJ solar cells. Research effort were also devoted to establish structure-property relationship and develop approaches to optimize light harvest, charge separation and charge collection, thus the overall power conversion efficiency (PCE). We have made very important contributions to the field and developed a series of new semiconducting polymers for highly efficient ternary polymer solar cells. We also discovered cooperative plasmonic effect of dual precious metal nanoparticles in enhancing PCE of BHJ solar cells. Multiwall carbon nanowire were introduced to significantly enhance the charge collection. These results have had significant impact to the area. Several polymers developed in our lab are now widely investigated around world. Seven of the papers published are highly cited as indicated by SCI.					
15. SUBJECT TERMS Low band gap polymers, organic solar cells, bulk heterojunction, photovoltaic effect.					
16. SECURITY CLASSIFICATION OF:			17. LIMITATION OF ABSTRACT SAR	18. NUMBER OF PAGES	19a. NAME OF RESPONSIBLE PERSON Dr. Charles Lee
a. REPORT Unclassified	b. ABSTRACT Unclassified	c. THIS PAGE Unclassified			19b. TELEPHONE NUMBER (include area code) (703) 696-7779

To: technicalreports@afosr.af.mil
Subject: Final Performance Report to Dr. Charles Lee

Contract/Grant Title: "Development of N- and P- Types of Semiconducting Polymers"
Contract/Grant #: FA9550-12-1-0061
Reporting Period: April 01, 2012 to March 31, 2015
Prepared by Luping Yu
Department of Chemistry, The University of Chicago, 929 E 57th Street, Chicago, IL 60637.

Abstract:

In the past three years, our research project sponsored partially by AFOSR has been focused on developing low bandgap semiconducting polymers as both the donor and acceptor materials for BHJ solar cells. Research effort were also devoted to establish structure-property relationship and develop approaches to optimize light harvest, charge separation and charge collection, thus the overall power conversion efficiency (PCE). We have made very important contributions to the field and developed a series of new semiconducting polymers for highly efficient ternary polymer solar cells. We also discovered cooperative plasmonic effect of dual precious metal nanoparticles in enhancing PCE of BHJ solar cells. Multiwall carbon nanowire were introduced to significantly enhance the charge collection. These results have had significant impact to the area. Several polymers developed in our lab are now widely investigated around world. Seven of the papers published are highly cited as indicated by SCI.

Accomplishments:

In the past three years, we made significant progress in four research directions in OPV solar cells.

1. Establishing structure property relationship between Low Bandgap Polymers and Their Organic Solar Cells Performance.

A key challenge of the development of organic photovoltaic devices is obtaining a predictive understanding of the relationship between polymeric structure of the donor material and device performance. Among the factors that may influence solar energy conversion, the nature of electron donating and accepting materials and the morphology of the composites play the crucial roles in determining the final performance of the devices. In recent years, fullerene derivatives such as [6,6]-phenyl C₇₁-butyric acid methyl ester (PC₇₁BM) have been widely adopted as electron acceptors due to their low lying energy levels and relatively high electron affinity and mobility. It was also found that addition of a small amount of high boiling point solvent, generally 1,8-diiodooctane (DIO), can reliably improve the morphology of most of the composite systems.^{19,20} Thus, we focus our main effort on understanding the structure/property correlation of electron donor materials in order to develop innovative strategies for achieving high performance solar cells.

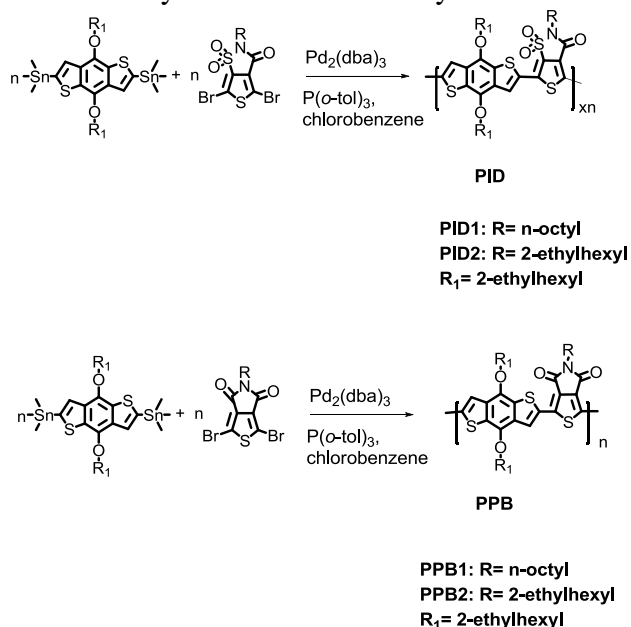
In previous studies, a linear correlation of the calculated dipole moment change between the ground and excited states $\Delta\mu_{ge}$ of single repeating units in charge transfer polymers was established, suggesting a larger local $\Delta\mu_{ge}$ could defray a part of exciton binding energy, leading to a higher power conversion efficiency (PCE). We further synthesized a new low bandgap polymers incorporating an artificial sweetener derivatives, *N*-alkyl, 3-oxothieno[3,4-*d*]isothiazole 1,1-dioxide (TID). Semi-empirical calculations on the local dipole moment change between ground and excited states ($\Delta\mu_{ge}$) in the repeating units of the new polymer indicate that the replacement of the carbonyl by a sulfonyl group leads to larger $\Delta\mu_{ge}$ values. The resulting polymers exhibit diminished power conversion efficiency (PCE) from bulk heterojunction (BHJ) solar cells with PC₇₁BM as acceptor, which extends the correlation between PCE and $\Delta\mu_{ge}$ of

single repeating units in p-type polymers to a new regime. Detailed studies show that the strongly electron withdrawing sulfonyl group is detrimental to charge separation in alternating copolymers containing TID unit.

Semi-empirical calculations on the local dipole moment change between ground and excited states ($\Delta\mu_{ge}$) in the repeating units of the new polymer indicate that the replacement of the carbonyl by a sulfonyl group leads to larger $\Delta\mu_{ge}$ values. The resulting polymers exhibit diminished power conversion efficiency (PCE) from bulk heterojunction (BHJ) solar cells with PC₇₁BM as acceptor, which extends the correlation between PCE and $\Delta\mu_{ge}$ of single repeating units in p-type polymers to a new regime. Detailed studies show that the strongly electron withdrawing sulfonyl group is detrimental to charge separation in alternating copolymers containing TID unit.

1.1. Synthesis of polymers: The TID unit was prepared according to a modified literature procedure.²⁶ In order to anchor alkyl side chains on the original artificial sweetener unit, the phase transfer catalyst 15-crown-5 was used to achieve a relatively high conversion yield. Two different solubilizing alkyl side chains were used, octyl and 2-ethylhexyl (used in PID1 and 2, respectively). The final monomer TID was prepared via a modified bromination procedure in the presence of strong Brønsted acids (See Scheme S1 for synthetic details). The BDT and TPD units were synthesized according to previous published procedures.^{7,27} Polymers were synthesized via Stille polycondensation using Pd₂(dba)₃/P(o-tolyl)₃ catalyst in refluxing chlorobenzene (CB) for 48 hrs.^{6,28} For comparison, another known polymer with a relatively large $\Delta\mu_{ge}$ value (PPB) was also synthesized and characterized in the same conditions as Scheme 1.

Scheme 1 Synthetic routes of Polymers.

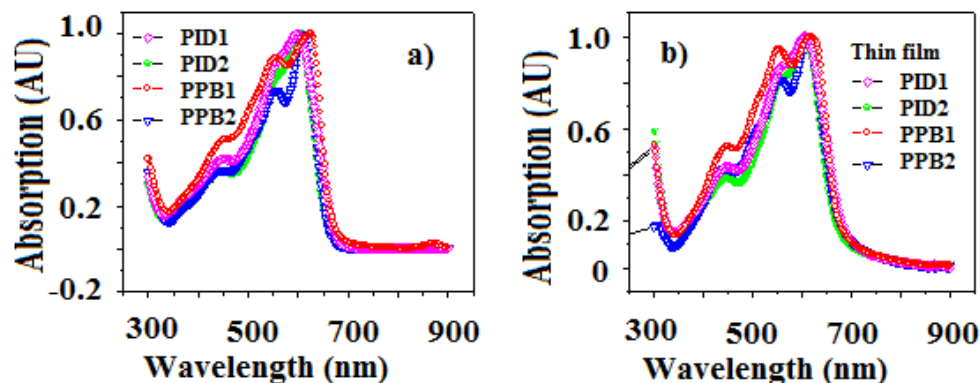


1.2 Optical and electrical properties of polymers

As shown by Gel permeation chromatography (GPC) measurements, these polymers exhibit number-averaged molecular weights between 12.0 and 18.6 kg/mol with a dispersity index (\bar{D}) around 2 (Table S1). The structures of polymers were confirmed by ¹H NMR spectra (Figure S1-S11) and elemental analyses (Table S2). Both the solution and thin-film optical absorption spectra of the polymers are presented in Figure 1. All polymers showed similar absorption range from 320 to 700 nm, and the absorption edge was nearly identical. The absorption maximum of the PID polymers was slightly blue-shifted compared to the PPB polymers. The cyclic voltammetry (CV) (Figure S12) studies indicated that the HOMO energy levels of PID1 and PID2 were at -5.44 and

-5.52 eV, approximately 0.1 eV lower than their corresponding PPBs; while the LUMO energy levels were at -3.55 eV and -3.50 eV, respectively.

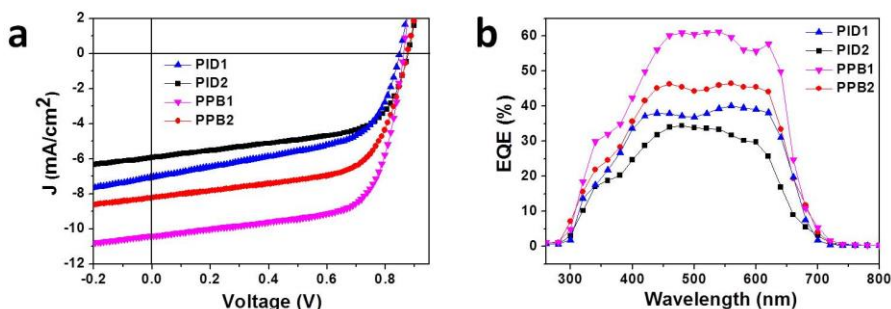
Figure 1. Normalized UV-vis absorption spectra of the polymers (a) in diluted chloroform solution and b) in pristine polymer films.



1.3 Current-Voltage (*J-V*) characteristics of the polymer solar cells

The photovoltaic properties were investigated in the device structure ITO/PEDOT:PSS/polymer:[6,6]-phenyl-C71-butyric acid methyl ester (PC₇₁BM)/Ca/Al. All solar cell data used in comparison of physical properties were determined based on this device structure. The active layers of ~100 nm were spin-coated from 10 mg/mL chlorobenzene (CB) and DIO (v/v, 97:3) solutions. The corresponding *J-V* curves of the four polymer solar cells under AM 1.5G condition at 100 mW/cm² are presented in Figure 2a. Representative characteristics of solar cells are summarized in Table 1. Devices fabricated from PID1, PID2, PPB1 and PPB2 showed best PCE values at 3.28%, 3.05%, 5.97%, and 4.48%, respectively. Figure 2b depicts the external quantum efficiency (EQE) curves of the four solar cells. The PPB1 showed highest EQE values around 60% within the spectral range from 450 to 650 nm while PID2 showed the lowest EQE values ca 30%. Changes in EQE curves are in good agreement with the observed *J_{sc}* values from the four polymers. Hole mobility of all four polymers, measured using space charge limited current (SCLC)²⁹ method, were $\sim 2.42 \times 10^{-4}$, 2.71×10^{-4} , 3.69×10^{-4} and 3.34×10^{-4} cm² V⁻¹ s⁻¹ for PID1, PID2, PPB1 and PPB2, respectively (Figure S13). Along with the EQE curves, the mobility values match with the *J_{sc}* trend well. Although PIDs exhibits high open circuit voltage due to a low HOMO energy level, small current density and low fill factor limit the overall solar cell performance.

Figure 2. (a) Characteristic J - V curves of the four solar cells and (b) EQE curves of the four solar cells.



To ensure that the comparison of solar cell performance is meaningful, the morphologies of these polymer films were optimized for the device performance by using organic additive in the film fabrication.³⁰ As shown in the transmission electron microscopy (TEM) images of blend films with and without DIO in Figure S14, all four solar cells with DIO exhibit fine phase separations while severe phase segregation was observed in the blend films without DIO, leading to almost zero photovoltaic effect (Figure S15).

Table 1. Comparison of Photovoltaic Parameters of TID and TPD-containing Polymers in the Blend with PC₇₁BM (CB/DIO, Polymer/PCBM = 1:1.5 Weight ratio).

Polymer	HOMO* (eV)	LUMO* (eV)	V_{oc} (V)	J_{sc} (mA/cm^2)	FF (%)	PCE (%)
PID1	5.44	3.55	0.85	7.06	54.7	3.28
PID2	5.52	3.40	0.88	5.94	58.6	3.05
PPB1	5.38	3.55	0.86	10.40	66.6	5.97
PPB2	5.40	3.55	0.88	8.23	62.2	4.48

Note: * From CV data.

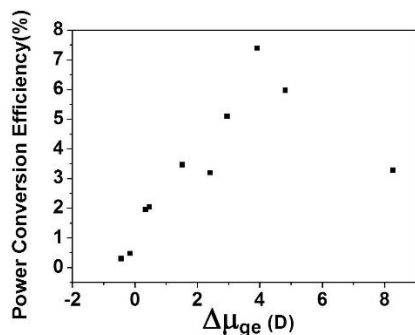
1.4. Correlation of $\Delta\mu_{ge}$ change and solar cell performance

The results shown are those for the optimized solar cells and therefore it is believable to use them to compare with other similarly optimized systems. The dipole moments of single repeating units in PID1 and PPB1 were calculated using the procedure in our previous study.¹⁸ The results are presented together with the optimized PCE values in Table 2 along with data for other polymers previously reported. To simulate the randomized orientation of the asymmetric TID unit, the average dipole moment for each polymer repeating unit was determined and used for the analysis of dependence of PCE values on dipole changes. Both the ground and excited state dipole moments were calculated for each polymer repeating unit in the series. The overall change $\Delta\mu_{ge}$ was calculated by accounting for the changes of the dipole along each coordinate axis. Our previous data indicated that a linear correlation between $\Delta\mu_{ge}$ and PCEs exists, where the PTB7 showed the highest values of both PCE (7.4%) and $\Delta\mu_{ge}$ (3.92 D). Such a trend was explained as an indication of local electron density gradient that defrays a part of the exciton binding energy, which enabled the cation generation in these polymers via intra-chain charge transfer even in solution.³² However, the results shown here indicate that further increasing $\Delta\mu_{ge}$ actually lowers PCE in the corresponding solar cell. PPB1 has a larger $\Delta\mu_{ge}$, but a lower PCE value of 5.97% than PTB7. The most notable dipole moment change $\Delta\mu_{ge}$ comes from the TID-based polymer PID1 which is almost twice as large as PTB7. However, it exhibits a PCE value only slightly above 3%, indicating that the linear relationship of $\Delta\mu_{ge}$ vs PCE did not extend (Figure 3) into the larger $\Delta\mu_{ge}$ regime.

Table 2. Calculated Single Repeating Unit Dipole Moments and the Corresponding Optimized PCE Values.

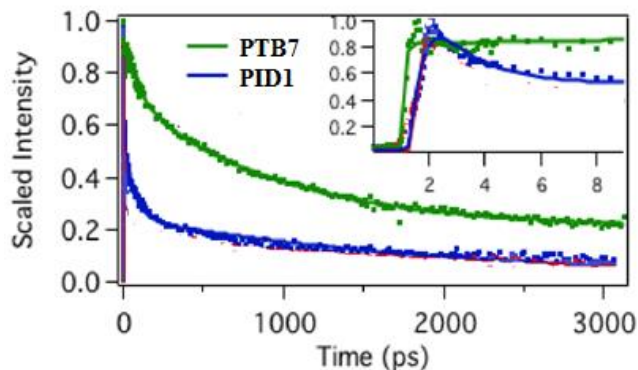
Polymer	μ_g (D)	μ_e (D)	$\Delta\mu_{ge}$ (D)	PCE (%)
PTB2	3.60	6.37	2.96	5.10
PTB7	3.76	7.13	3.92	7.40
PTBF2	3.35	5.45	2.41	3.20
PBB3	0.61	0.82	0.47	2.04
PBIT1	4.46	4.80	0.34	1.96
PBIT3	6.99	6.83	-0.16	0.47
PBTZ1	0.88	2.41	1.52	3.46
PBTZ2	1.92	1.48	-0.44	0.29
PPB1	3.58	7.60	4.82	5.97
PID1	4.69	12.08	8.26	3.28

Figure 3. Correlation of PCE values with calculated dipolar changes of polymer repeating unit.



To explain these trends, we can reason that a higher $\Delta\mu_{ge}$ implies a larger displacement of hole-electron pair in an exciton, lower Coulombic interactions between charges, and hence a reduced exciton binding energy. In addition, the introduction of strong electron withdrawing group simultaneously enhances the polarizability of excitons and lowers the polymer LUMO energy level. Ideally, the polarized exciton facilitates an electron transfer from the polymer blocks with lower electron affinity to the adjacent blocks with higher electron affinity and then to fullerene. However, the sulfonyl group exhibits strong electron accepting ability, leading to a much larger $\Delta\mu_{ge}$ (8.26 D) than PTB7 (3.92 D) and a highly polarized exciton with a larger effective separation of charges within a polymer repeating unit and beyond. When $\Delta\mu_{ge}$ is too large, the polarized polymer repeating units could also acts as trapping or recombination centers for electrons and compete with the electron injection to the fullerene. This happens in the PPB and PID series of polymers, particularly PID1, with LUMO energy nearly 0.24 eV lower than that of PTB7. Ultrafast spectroscopic results, taken at 840 nm at which the cationic state absorption of the PID or PPB polymer in blended films dominates, confirmed this hypothesis. Although the rising time of the PID1 cation signal is still nearly 1 ps, the intramolecular charge separation (CS) dynamics in PID1 are slower than those of PTB7. The charge recombination (CR) of the cationic state, however, is relatively fast for the PID1 polymer. The CR traces of the PID1 polymer were fit to a tri-exponential decay of 2 ps, 60 ps, and > 2 ns. At 3 ns, the cationic signal of only <10% remains, which is much smaller than those in PTB7 (Figure 4). The increased recombination rate is attributed to the increased binding energy of the bound charge transfer state within the polymer, which enhance the recombination probability. These results seem to indicate that the TID unit is too strong in electron-withdrawing ability to be useful in heteropolymers used as donor materials. An optimized polarizability in polymer repeating units is achieved with a $\Delta\mu_{ge}$ around 4 Debye.

Figure 4. The charge separation (rise) and recombination (decay) dynamics monitored at the signals of the cationic state in the PID1 polymer. For comparison, the CS and CR of PTB7 are also shown.



1.5. Further synthetic effort was focused on the roles of quinoidal character and regioregularity in determining the optoelectronic and photovoltaic properties of conjugated copolymers.

An efficient synthetic method for creating ladder-type, oligomeric donor monomers with fused thienobenzothiophene structures. These monomers are copolymerized with fluorinated thieno[3,4-b]thiophene ester to form a series of polymers which were investigated as donor materials in polymer/fullerene solar cells. Photophysical and electrochemical characterizations are used in conjunction with quantum-chemical calculations to identify the interplay of quinoidal and charge transfer character in the optical gaps of conjugated copolymers, providing broadly applicable design rules for tuning the excitation character of conjugated copolymers. X-ray diffraction, mobility measurements, and solar cell device characterization are used to analyze neat films and bulk heterojunctions of these copolymers, demonstrating the importance of the spatial symmetry of the donor and acceptor unit in determining the charge transport characteristics of conjugated copolymers.

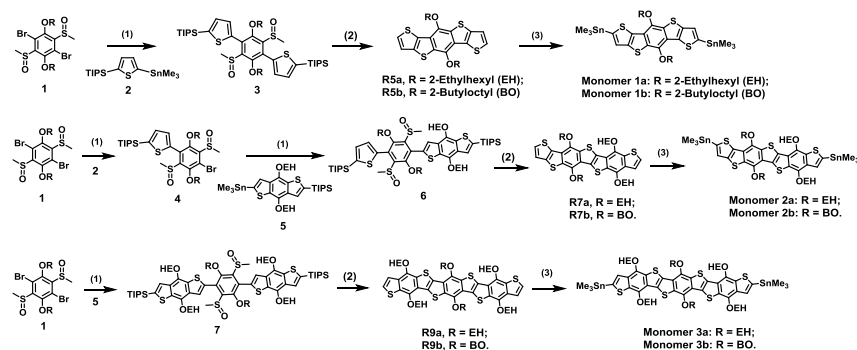
An issue in conjugated copolymers that is not often discussed, but is of vital importance, is the regioregularity of these polymers. While this issue was at the forefront of polymer design in previous generations of materials, notably **P3HT**,^{49,50} this topic has lost interest in recent studies of novel copolymer materials, although some careful studies have examined these effects in donor-acceptor polymers.⁵¹ In recent work, we have computationally examined the effects of conformational and structural dispersion in the optoelectronic properties of conjugated copolymers⁵² and found that copolymers synthesized via non-selective cross coupling reactions such as Stille Coupling, can exhibit dispersion in their optoelectronic properties when the comonomers do not possess the appropriate symmetry operations. The exact role of this energetic dispersion in the charge transport properties of conjugated copolymers is unclear, though it is known that the tail of the density of states primarily determines V_{oc} ,⁵³ and that energetic disorder localizes charge carrier wavefunctions, which should decrease J_{sc} . Consequently, the dispersion of these properties that results from such structural and conformational isomerism is fundamental to interpreting the bulk device properties of these materials, and could benefit from an experimental study of charge transport characteristics in polymers that possess variable amounts of structural dispersion.

Fused thienobenzothiophene polymers have demonstrated much success when employed in conjugated polymer/fullerene based BHJs. The original design idea for the highest performing fused thienobenzothiophene polymer, **PTB7**, was to create a low band gap polymer with enhanced quinoidal structure resulting from the thienothiophene (TT) moiety, which would facilitate charge delocalization and transport by increasing the π -conjugation, as well as improved π - π stacking capability resulting from the introduction of the conjugated fused aromatic ring moiety,

benzodithiophene. Furthermore, these types of conjugated copolymers have demonstrated high versatility for fine-tuning energy levels as well as electronic properties via fluorination⁵⁴ and side-chain substitution effects. Given our experience with these materials, we can use these chemical motifs as models for examining the general properties of conjugated copolymer chemistry and physics. It is well known that materials with extended conjugation in structure were studied extensively as candidates in organic field effect transistor when they showed appreciable charge carrier mobility.⁵⁵⁻⁵⁷ Previous work on small oligomers has examined the effects of the thienothiophene quinoidal character on optoelectronic functionality in these materials.⁵⁸ However, how the thienothiophene quinoidal character propagates in a periodically repeating polymer system as a function of comonomer size and chemical identity represents a fundamental gap in the knowledge base of these systems. Additionally, these chemical motifs present an excellent opportunity for the examination of the previously mentioned dependencies on regioregularity by simply altering the symmetry of the donor comonomer. By perturbing the original **PTB7** chemical structure, we are positioned to answer a variety of important questions in the physics and chemistry of conjugated copolymers.

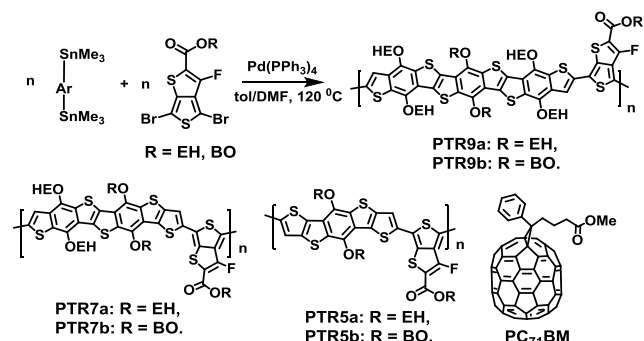
Previous work has shown that a polymer made from five-ring heteroacene donor units exhibits a similar PCE as **PTB7** in a simple solar cell device.⁵⁹ To investigate the effect of the electron delocalization, a generic method was developed to synthesize oligo-heteroacenes with varied number of fused rings (Scheme 1). The key building block is the compound **1**, 1,4-dibromo-2,5-dialkoxy-3,6-bis(methylsulfinyl)benzene (SI). Pd-mediated coupling reaction between compound **1** and compound **2** in 1:2 ratio yielded precursor **3**, which was cyclized by a ring closing reaction to form **R5**. Lithiation of **R5** followed by stannylation generates monomer **1**, which has five fused rings. Similar coupling reaction between compounds **1** and **2** in 1:1 ratio yielded compound **4** that can be further coupled with compound **5** to yield precursor **6**. Identical cyclization and stannylation reactions lead to monomer **2**. When compounds **1** was coupled with 2 equivalent of compound **5**, the precursor **7** was formed, which can be cyclized to fused nine rings (**R9**) and then be stannylated to form monomer **3**.

Scheme 2: Synthesis of monomers



Among these conversions, the key step is the ring-closing reaction, which is an intramolecular electrophilic substitution by using trifluoroacetic acid (TFA) and P₂O₅ as the reagent, followed by elimination reaction in pyridine. The triisopropylsilyl (TIPS) group played a vital role, since it not only enriched the electron density of the aromatic system, favoring the electrophilic addition, but also prevented the active alpha position of thiophene unit from intermolecular side reactions. Interestingly, the TIPS group attaching to the BDT unit had been mostly removed during ring-closing step, while that on the thiophene unit remained intact, until TBAF was added as observed in the synthesis of **R7**.

Scheme 3 Synthesis of polymers and the structure of PC71BM



The resulting monomers were polymerized with F-substituted dibromo-thienothiophene ester monomer via the Stille polycondensation (Scheme 3). GPC measurements showed sizable molecular weights for these polymers (Table 3). NMR spectra and elemental analysis support the structure as proposed. It was found that **PTR5a** polymer, with 2-ethylhexyloxy (O-EH) side chains was barely soluble in common organic solvents like THF, chloroform and chlorobenzene, and was not further studied. When the side chains were changed to bulkier 2-butyloctyloxy (O-BO) groups, the resulting polymer **PTR5b** exhibited good solubility. Both **PTR7** and **PTR9** show good solubility in organic solvents with both the EH and BO side chains, simply because **R7** (4 side chains/7 rings) and **R9** (6 side chains/9 rings) bear more side chains than the **R5** (2 side chains/5 rings).^{60,61} The TGA studies indicated that the polymers are stable up to around 310 °C at which weight losses of 5% were observed (SI).

Table 3: Molecular weight and UV-vis absorption properties of polymers

Polymers	Mn (kg/mol)	PDI	λ_{peak} (nm)	λ_{onset} (nm)	E_g^{opt} (eV)
PTR5b	35.6	2.15	659	747	1.66
PTR7a	12.6	1.57	595,627	703	1.77
PTR7b	12.3	1.54	586,624	696	1.78
PTR9a	11.0	2.62	580,620	675	1.84
PTR9b	14.7	2.82	580,625	678	1.83

2. Optical and electrochemical properties

The optical absorption spectra of **PTR5**, **PTR7**, and **PTR9** were recorded in both chlorobenzene solution and the neat film, the results of which are similar, as in the case of **PTB7**, which is suggestive of solution-phase aggregation. Those for the neat film are summarized in Table 3. By looking at the red edge of the neat film absorption spectra for **PTR5**, **PTR7**, and **PTR9** (Figure 5a), an apparent blue-shift is observed in the optical absorption as the length of the donor unit is increased from **PTR5** to **PTR9**. The electronic band gaps of these polymers were measured with cyclic voltammetry (CV), using thin films coated on a glass carbon electrode with a scan rate of 50 mV/s and electrolyte Bu₄NPF₆ in CH₃CN solution (0.10 M). The measured electronic band gaps (Figure 5b) demonstrated a similar overall blue shift in going from **PTR5** to **PTR9**. However, this trend is in contrast with the absorption spectra of donor monomers, which showed a red-shift from **R5** to **R9** (Figure 5c).

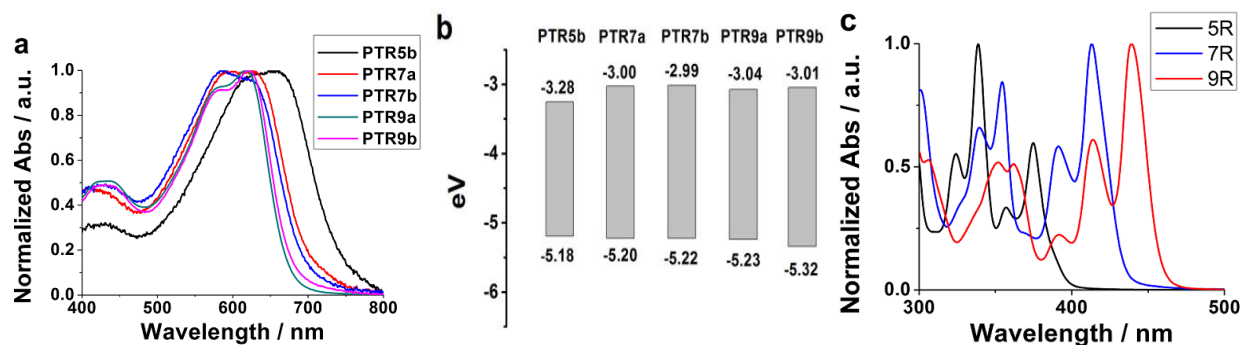


Figure 5 (a) UV-vis absorption spectra of polymers in films gained from spin-coating of their chlorobenzene solution to clean glass. (b) Energy level diagram of polymers. (c) UV-vis absorption spectra of donor monomers in dilute chloroform solution.

The observed shift in the optical gap of polymers and donor monomers seems to be counterintuitive that increasing the size and rigidity of the pi-electron system does not reduce the optical gap of conjugated polymers. However, it is important to pay close attention to the nature of the molecular units along the backbone, as many potential mechanisms for lowering the optical gap of conjugated polymers exist.⁶² All polymers studied here consist of copolymers of the highly quinoidal thienothiophene unit^{63,64} and the highly aromatic fused benzodithiophene donor units. As the number of fused benzodithiophene units of the donor grows, the energy penalty becomes too large to be overcome by the quinoidal character of the thienothiophene unit. As a result, the longer donor moieties prefer fused aromatic rings to the quinoidal form, thus preventing the band gap from further narrowing. In the extreme limit of infinite donor length, the optical absorption should reach the limit of the donor monomer unit. Consequently, by increasing the size of the fused benzodithiophene donor units in an attempt to enhance pi-stacking and decrease the optical gap, it appears that we have fundamentally altered the nature of the optical excitation by changing the quinoidal/aromatic character of the backbone

3. Computational work

Ground and excited-state density functional theory (DFT) calculations were performed to support the above hypothesis. An oligomer of each repeat unit was chosen (SI), and a ground-state geometry optimization was performed at the EDF1/6-31G* level of theory. In these calculations, all alkoxy groups were simplified to methoxy groups. These ground-state oligomer structures were then used as input to ground-state DFT and excited-state time-dependent DFT (TDDFT) calculations at the OT-BNL/6-31G* level of theory.⁶⁵ These results are summarized in Table 4. Excitations on ground-state vacuum structures should not match up quantitatively with the absorption edge, due to polarization and flattening effects in the film.⁶⁶ However, the OT-BNL method has been used to accurately determine the excitation energies in studies on similar materials.⁶⁷ While the absolute values of our computed optical gaps are shifted from experimental results, the relative blue-shift of each structure was accurately predicted, and compares favorably with the experimental spectrum, confirming that the blue-shift is indeed due to the changes in chemical structure, and not solely the result of differential polymer aggregation in the film.

Table 4 Calculated energy levels and gaps for polymers

Polymers	HOMO (eV)	LUMO (eV)	Eg ^{opt} (eV)
PTB7	-5.09	-1.06	2.14
PTR5	-5.03	-1.01	2.12
PTR7	-5.14	-0.94	2.25
PTR9	-5.12	-0.82	2.32

In order to quantify this further, DFT calculations (OT-BNL/6-311G**) were performed to determine the energy level alignment of the donor and acceptor units used in these copolymers. It was determined that indeed the band gaps of the donor monomers become narrow as they become longer, which is consistent with the optical absorption spectra of monomers as present in Figure 1c. However, when comparing with the acceptor monomer thienothiophene, it is clear that as the conjugation of the donor unit increases above the 5-ring (**PTR5**), the lowest unoccupied molecular orbital (LUMO) level of the donor drops below the LUMO of thienothiophene (Figure 6). Consequently, the conjugation in the resulting polymers (**PTR7** and **PTR9**) between the donor monomer and acceptor monomer becomes less efficient, decreasing the charge transfer nature of the excitation, resulting in a less quinoidal structure, and the blue shift of the polymers relative to **PTB7**.

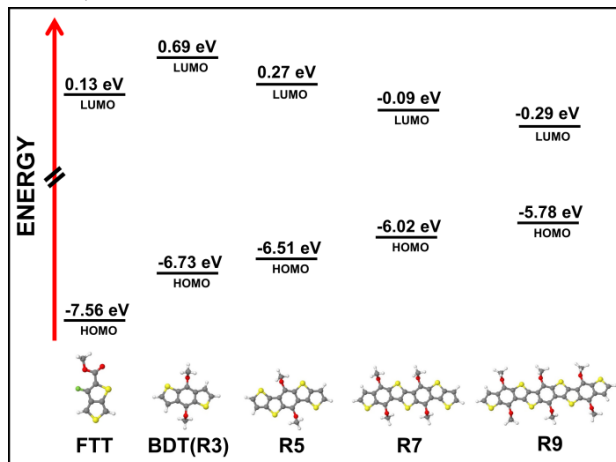


Figure 6. Calculated energy levels of monomers. Geometry was optimized at EDF1/6-31G* and energy levels were calculated at OT-BNL/6-31G*.

4. X-Ray Diffraction

The blend films of polymers show uniform and fine features according to TEM studies (SI). The GIWAXS studies (Figure 7) indicate that neat and blend **PTR5**, **PTR7**, and **PTR9** films all exhibit scattering between $q = 0.32\text{--}0.38 \text{ \AA}^{-1}$ which relates to d-spacings of $20 \text{ \AA} - 17 \text{ \AA}$ corresponding to **PTR** lamellar stacked regions and is determined by the type and orientation of the alkyl side chains. This scattering can be divided into two distinct regions: an arc growing from $q_{xy} = 0.32\text{--}0.36 \text{ \AA}^{-1}$ and a more localized peak at $q_z = 0.33\text{--}0.38 \text{ \AA}^{-1}$. In general, features along the horizontal, q_{xy} , axis describe the in-plane structure while features along the vertical, q_z , axis roughly describe the out-of-plane structure,⁶⁸ so the presence of lamellar stacking in both the horizontal and vertical suggest that two different orientations and crystal packing are present in the **PTR** thin films. The out-of-plane lamellar stacking indicates an edge-on orientation of the polymer and a smaller d-spacing, while the in-plane lamellar stacking indicates a face-on orientation of the polymer and a larger d-spacing. For neat films of **PTR9a** and **PTR9b**, in addition to the lamella scattering peaks, an out-of-plane scattering peak appears at $q = 0.54 \text{ \AA}^{-1}$ (1.1 nm) and $q = 0.49 \text{ \AA}^{-1}$ (1.2 nm), respectively, consistent with the change to larger side chains in **PTR9b**. We attribute this peak to different polymorphs of the edge-on lamellar stacking in **PTR9** which can be attributed to different side chain orientations. While it is possible these polymorphs exist in the **PTR5** and **PTR7** polymers, we suggest that they are more highly ordered in the **PTR9** polymers due to the increased backbone rigidity. These polymers also exhibited $q = 1.61\text{--}1.65 \text{ \AA}^{-1}$ corresponding to a $\pi\text{-}\pi$ d-spacing around $3.8\text{--}3.9 \text{ \AA}$. Note that the $\pi\text{-}\pi$ stacking is only present in the vertical direction, so while edge-on lamellar stacked domains are present, the edge-on domains do not create 3-dimensional $\pi\text{-}\pi$ stacked crystals. In the neat films, a broad isotropic scattering peak at $q = 1.0\text{--}1.3 \text{ \AA}^{-1}$ is attributed to amorphous scattering, while in blend films, the isotropic ring at $q = 1.4 \text{ \AA}^{-1}$ is due to the PCBM structure

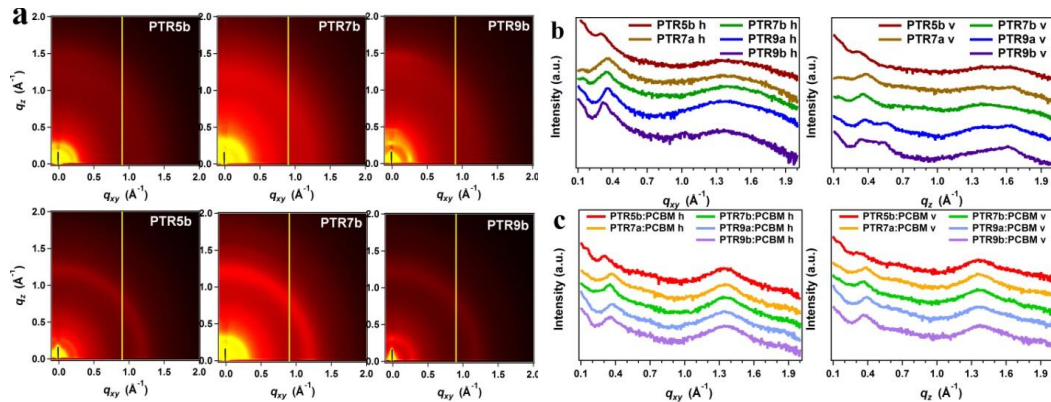


Figure 7: (a) 2D GIWAX images for neat polymer films (upper) and polymer/PCBM blend films (lower). (b) Linecut of GIWAX images of neat polymer films on horizontal (left) and vertical (right) direction. (c) Linecut of GIWAX images of polymer/PCBM blend films on horizontal (left) and vertical (right) direction.

Scherrer analysis is used to measure trends in the crystalline domain size of the lamellar stacked domains and the π - π stacked domains. Neat **PTR5** and **PTR7** films exhibit small face-on lamellar crystalline domains of 4-6 nm while both PTR9 films contain domains of 8-10 nm. The π - π stacked domain size follows a similar trend (Table 5) and we attribute the increased domain sizes in **PTR9** to its increased backbone rigidity, leading to more ordered polymer domains. In blend films, the reverse trend is observed and the face-on lamellar domain size is smaller for **PTR9** (~4 nm) than for **PTR7** (5.6-7 nm) and **PTR5** (~8 nm). The π - π stacked domain size cannot be confidently calculated due to its low intensity and overlap with the PCBM peak. After forming blend film with PCBM, all of polymer domains are homogenized to 2-5 nm, indicating that the polymer phase separation is ideal for exciton migration.

Table 5: Lamellar and π - π d-spacing and domain size for both neat and blend films of polymers

Polymers	Lamellar (\AA)	Domain size (\AA)		π - π (\AA)	Domain size (\AA)	
	neat	neat	blend	neat	neat	blend
PTR5b	19.91	65	84	3.83	18	23
PTR7a	17.60	42	56	3.80	41	33
PTR7b	18.14	49	72	3.83	12	32
PTR9a	17.78	102	40	3.84	49	50
PTR9b	19.13	83	45	3.88	46	31

5. Hole mobility

The hole mobilities of polymers were measured according to the Space Charge Limited Current (SCLC) model, and the results were plotted in Figure 4, from which hole mobilities of 5.02×10^{-4} , 2.50×10^{-6} , 5.56×10^{-6} , 1.32×10^{-4} , $1.11 \times 10^{-4} \text{ cm}^2/\text{V}\cdot\text{s}$ were observed for **PTR5b**, **PTR7a**, **PTR7b**, **PTR9a** and **PTR9b**, respectively (Figure 8). **PTR5b** exhibits similar mobility with **PTB7**. A significant decrease occurred when the polymer's donor moiety changed to larger conjugated system. The hole mobility of **PTR9** dropped to about 1/5~1/4 of that of **PTR5**, and that of **PTR7** was even 2 orders of magnitude smaller than that of **PTR5**. While one would expect increased conjugation and rigidity of the donor moiety to favor for charge carrier transport, the decrease in mobilities appears to correlate with the side-chain to fused ring ratio of **PTR5** through **PTR9**. As the fused ring system is made longer, the ratio of side-chains to fused rings grows. More alkyl side-chains would disrupt π - π stacking, and decrease charge transport by lowering intermolecular

charge transfer couplings. While this explanation is capable of explaining the general trend of decreasing polymer mobility as the length of the donor unit grows, it is not capable of explaining the drastic decrease in the mobility observed for **PTR7**. Upon examination, it becomes clear that **PTR7** differs from **PTR5** and **PTR9** in that it exhibits only C1 symmetry. As shown in recent work,⁵² whether or not the donor and acceptor units possess appropriate symmetry in a Stille condensation process determines the width of the distribution of structural and conformational isomers. While most copolymers in the literature consist of symmetric donor and a symmetric or asymmetric acceptor, **PTR7** consists of asymmetric donor and an asymmetric acceptor. The backbone of the copolymer then will exhibit 2^n (where n is the length of the copolymer) more potential regioisomers than the corresponding **PTR5** and **PTR9**. Given the similarity of the XRD data regarding these materials, it is likely that the increase in disorder of the backbone's electronic system resulting from this regioirregularity is leading to localization of the wave function, and decreasing the mobility of charge carriers, in agreement with the observed mobilities. With the same backbone, a slight decrease of hole mobility was observed after introducing bulky side chains if we compare that of **PTR9a** and **PTR9b** due to the increase in the steric hindrance for intermolecular packing. GIWAXS studies (Figure 7) indeed showed that the lamellar d-spacing for **PTR9b** was larger than that of **PTR9a**.

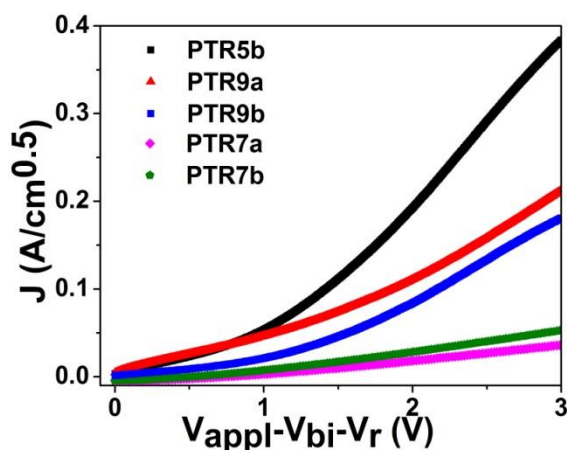


Figure 8: $J^{0.5}$ vs V plots for the polymer films.

6. Photovoltaic properties

Photovoltaic properties of polymers were investigated in a device structure of ITO/PEDOTS:PSS/polymer:PC₇₁BM (1:1.5, wt ratio)/Ca/Al. The active layer was prepared by spin-coating polymer solution in mixed solvent of CB/DIO (97/3, v/v). Figure 9a showed the J-V response of polymer solar cells under AM 1.5 condition at 100 mW/cm². Representative characteristics were summarized in Table 4. The cell made from **PTR5b** gave a PCE of about 5% with moderate J_{sc} (12.2 mA/cm²) and V_{oc} (0.65 V). The **PTR9** polymers exhibited slightly higher V_{oc} (0.71 V), which might be due to their deeper HOMO, but showed inferior efficiency because of the lower J_{sc} and fill factor. The corresponding EQE spectrum in Figure 9b indicates that **PTR5b** had a higher EQE value with over 40% in the 400 nm to 700 nm range than that of **PTR9**, which was consistent with their J-V performance. However, the performance of polymer solar cells can be improved by modifying the side chain attached to the backbone. For example, replacement of the dialkoxy benzodithiophene (2-ethylhexyloxy, O-EH) in the **PTB7** with alkyl analogue (CH₂EH), generated a new polymer **PTB10** (Scheme 3), which showed slightly higher V_{oc}, but slightly lower J_{sc}, and overall, almost the same PCE (7.3%) as **PTB7** (7.4%). But for **PTDBD**, it triumphed over **PTR5b** in all aspects and the PCE increased from about 5% to 7.6%. The same trend is observed for **PTR9c**, which had an efficiency of 5.5%, doubled that of the other two **PTR9** polymers. It is not surprising that even though the structure of **PTR7** polymers is very similar to those of **PTR5** or **PTR9**, their solar cell performances are extremely low with nearly 0%

efficiency. As discussed above, the asymmetric nature of donor monomer leads to the regioirregularity of **PTR7** polymer, which should account for their low charge carrier mobilities, and thus poor performance in OPV cells is predicted

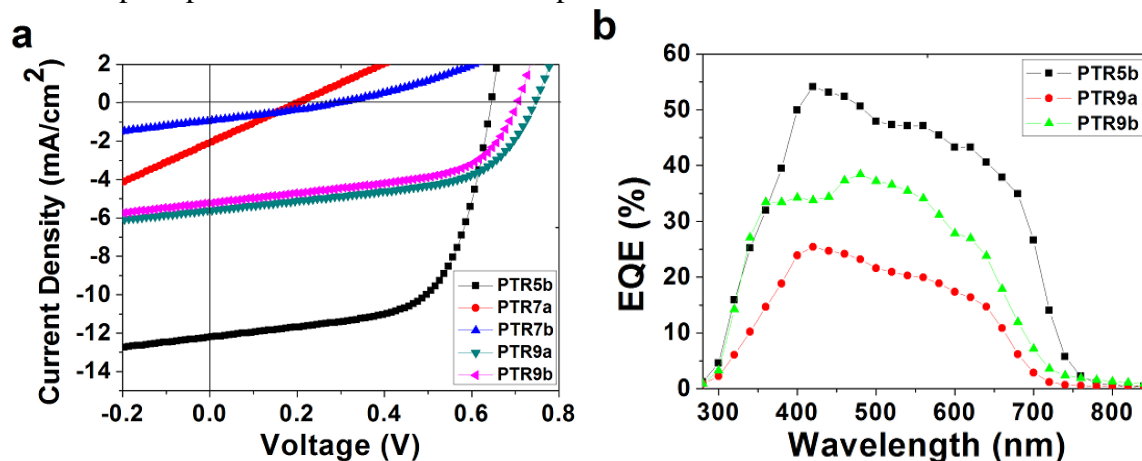


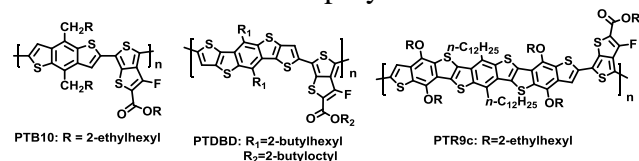
Figure 9: (a) J-V characteristics of polymer solar cells under AM 1.5 condition (100 mW/cm²), (b) EQE of polymer/PC₇₁BM device. No result was obtained for **PTR7** polymers because of the low current of devices.

Table 6. J-V characteristics of polymer solar cells

Polymers	Jsc (mA/cm ²)	Voc (V)	FF (%)	PCE (%)
PTB7a	14.5	0.74	69.0	7.4
PTR5b	12.2	0.65	63.0	5.0
PTR7a	0.28	0.20	25.0	0.014
PTR7b	0.96	0.30	28.8	0.083
PTR9a	7.23	0.71	54.6	2.8
PTR9b	5.22	0.71	54.0	2.0
PTB10	13.6	0.77	69.1	7.3
PTDBD^b	13.0	0.89	65.3	7.6
PTR9c	11.2	0.72	67.9	5.5

a: ref [⁴⁵]; b: ref [⁵⁹]

Scheme 5. Structures of polymers after modification



2. Enhance light harvest via cooperative plasmonic effect of dual precious metal nanoparticles: The major achievement in the past year in Yu's lab is the demonstration of a cooperative plasmonic effect on improving the performance of polymer bulk heterojunction (BHJ) solar cells. When mixed Ag and Au nanoparticles are incorporated into the anode buffer layer, dual nanoparticles show superior behavior on enhancing light absorption in comparison with single nanoparticles, which led to the realization of a polymer solar cell with a power conversion efficiency of 8.67%, accounting for a 20% enhancement from that without nanoparticles. The cooperative plasmonic effect aroused from dual resonance enhancement of two different NPs. The idea was further unraveled by comparing Au nanorods with mixed nanoparticles for solar cell application. A similar enhancement of nanorods mixture with that of mixed Au and Ag

nanoparticles was observed because the plasmonic absorption spectra of gold nanorods also exhibit dual peaks in the visible region. Detailed studies shed light into the influence of plasmonic nanostructures on exciton generation, dissociation and charge recombination and transport inside thin film devices. We believe that the results of our study offer an effective approach to enhance the efficiency of organic BHJ solar cells.

3. Facilitate charge separation via Ternary Blend Polymer Solar Cells

Ternary blend PSCs with two donor materials and one fullerene acceptor are emerging as an attractive strategy to overcome the PCE bottleneck for binary devices while maintaining the simplicity of processing condition as for single active layer compared to tandem cells. Recently, dye sensitizers²⁰⁻²², polymer sensitizers²³⁻²⁶, small molecular sensitizers²⁷ and quantum dot sensitizers^{28,29} have been utilized as the additional donor material in ternary blend solar cells to extend the absorption of solar spectrum. However, most of these systems are based on P3HT as the dominating donor polymer and still exhibit poor performance compared with the state of the art binary counterparts. Not to mention the even reduced device performance in some cases with the third component acting as recombination centers or defects within the active layer^{30,31}. In addition, although it has been reported that adding PCPDTBT into P3HT:PCBM blend would lead to decreased crystallinity of PCBM³² or smooth surface morphology³³, no experimental evidence of positive changes in bulk morphology inside the ternary blend system after the incorporation of the third component has been reported.

In this work, we demonstrate for the first time, efficient ternary blend BHJ solar cells with PCEs larger than 8% by incorporating poly-3-oxothieno[3,4-*d*]isothiazole 1,1-dioxide/benzodithiophene (PID2) as the additional donor material into polythieno[3,4-*b*]-thiophene/benzodithiophene (PTB7) : [6,6]-Phenyl C71 butyric acid methyl ester (PC₇₁BM) host binary blend. Unlike common ternary blend systems, where the enhancement in PCE mainly comes from extended light harvesting in solar spectrum by the third component^{24,25,28,34}, we show for the first time that a high efficient ternary blend solar cell could also be developed with the third component not only improving photon absorption range but more importantly, facilitating charge separation and transport while suppressing charge recombination through a combination of cascade energy levels and optimized device morphology.

Chemical structures of PTB7, PID2 and PC₇₁BM are shown in Figure 11a. The synthesis and characterization of PID2 will be published elsewhere. The highest occupied molecular orbital (HOMO) energy level and lowest unoccupied molecular orbital (LUMO) of PID2 are -5.52 eV and -3.50 eV, determined from cyclic voltammetry curve. PID2 used in this work has a molecular weight at 32 kg/mol. The cascade energy levels of the three components are shown in Figure 1b. Solar cells used in this work have a simple structure that we always used to evaluate the material's properties:

ITO/poly(3,4-ethylenedioxythiophene):poly(styrenesulfonate) (PEDOT:PSS)/PTB7:PID2:PC₇₁BM /Ca/Al (Figure 11c).

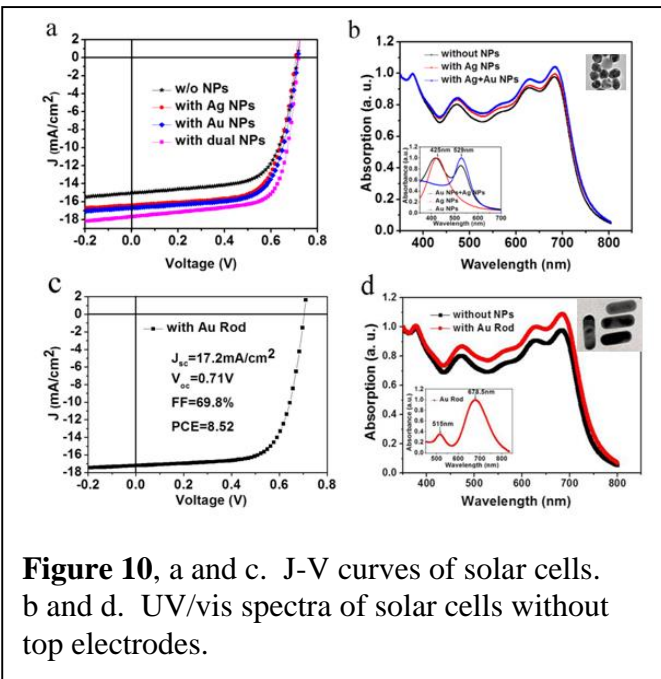


Figure 10, a and c. J-V curves of solar cells. b and d. UV/vis spectra of solar cells without top electrodes.

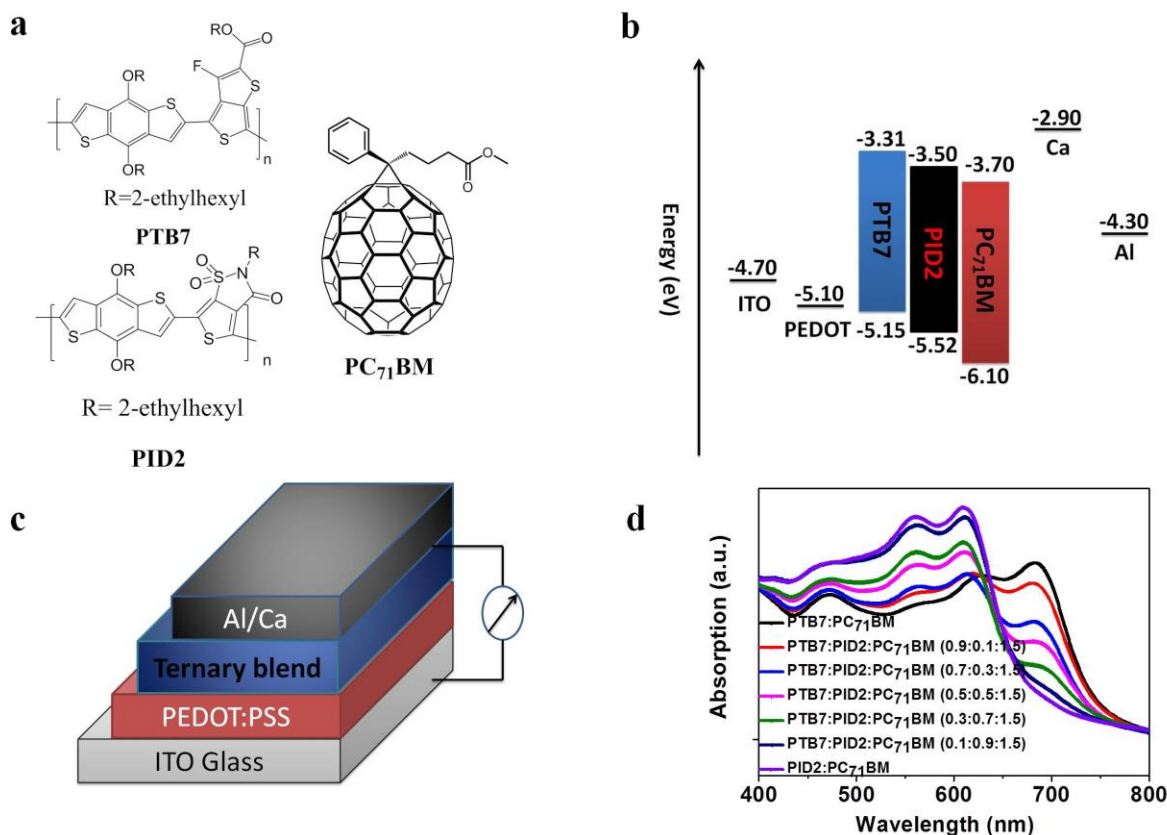


Figure 11: | Material properties and device structure. **a**, Chemical structures of PTB7, PID2, PC₇₁BM. **b**, energy levels of electrodes and active layer materials used in ternary blend solar cells. **c**, device structure of solar cells used in this work. **d**, UV-vis absorption spectra of ternary PTB7:PID2:PC₇₁BM blend with different ratios of PTB7:PID2.

We first measured the UV-vis absorption of the ternary blends with different PID2 contents to study the changes in absorption upon incorporation of the third component. Figure 11d indicates that increasing the content of PID2 in PTB7:PC₇₁BM host blend gradually enhanced the absorption from 450 nm to 650 nm while simultaneously decreased the absorption from 650 nm to 750 nm, consistent with the fact that the PID2 showed maximum absorption at 610 nm and the absorption maximum of PTB7 was at 683 nm.

The overall polymer to PC₇₁BM ratio was kept at 1:1.5 in this work. Figure 12a shows the corresponding current density versus voltage (*J*-*V*) characteristics of ternary blend solar cells with different PID2 contents under AM 1.5 G illumination at 100 mW/cm². Table 7 summarizes the photovoltaic parameters for those devices. The PTB7:PC₇₁BM used as a reference device gave a PCE of 7.25% with an open circuit voltage (*V*_{oc}) at 0.72 V, a short circuit current density (*J*_{sc}) at 15.0 mA/cm² and a fill factor (*FF*) at 67.1%. It is clear from Figure 12a that *J*_{sc} was enhanced significantly after the incorporation of a small amount of PID2 (10% or 30%) into the host blend and decreased later when PID2 became the dominating donor polymer in the system. The decreased performance at high PID2 content should be ascribed to the poor performance of PID2, which only gave a PCE of 2.01% when mixed with PC₇₁BM. Meanwhile, *V*_{oc} of the ternary blend solar cells was pinned to the smaller *V*_{oc} of PTB7:PC₇₁BM host blend at all PID2 contents. This is attributed to the fact that *V*_{oc} is mainly determined by the smallest difference between HOMO energy levels of donor materials and LUMO energy level of PC₇₁BM²⁴. The HOMO energy levels of PTB7 and PID2 are -5.15 eV and -5.52 eV, respectively (Figure 11b). In particular, with a 9:1 ratio between PTB7 and PID2, we achieved a *V*_{oc} at 0.72 V, a *J*_{sc} at 16.8 mA/cm² and a *FF* at

68.7%, resulted in a very promising PCE of 8.22%. An average PCE of 8.01% was attained over 10 identical devices under this condition with a mean V_{oc} at 0.71 ± 0.01 V, a J_{sc} at 16.7 ± 0.36 mA/cm² and a FF at $67.9 \pm 0.70\%$. To the best of our knowledge, this is the highest PCE reported for ternary blend PSCs so far. When the content of PID2 was increased to 30%, J_{sc} of the device was improved to 16.3 mA/cm², yielding a PCE of 7.88%. Solar cell with 50% of PID2 showed comparable PCE compared to the reference device. Further increasing the content of PID2 beyond 50% resulted in decreased solar cell performance due to inferior J_{sc} and FF compared to PTB7:PC₇₁BM reference device. Since incorporation of 10% and 30% PID2 showed better solar cell performance than the reference device, the two conditions are used in the following measurements to unravel the mechanism for the increase in J_{sc} and FF in our ternary blend system.

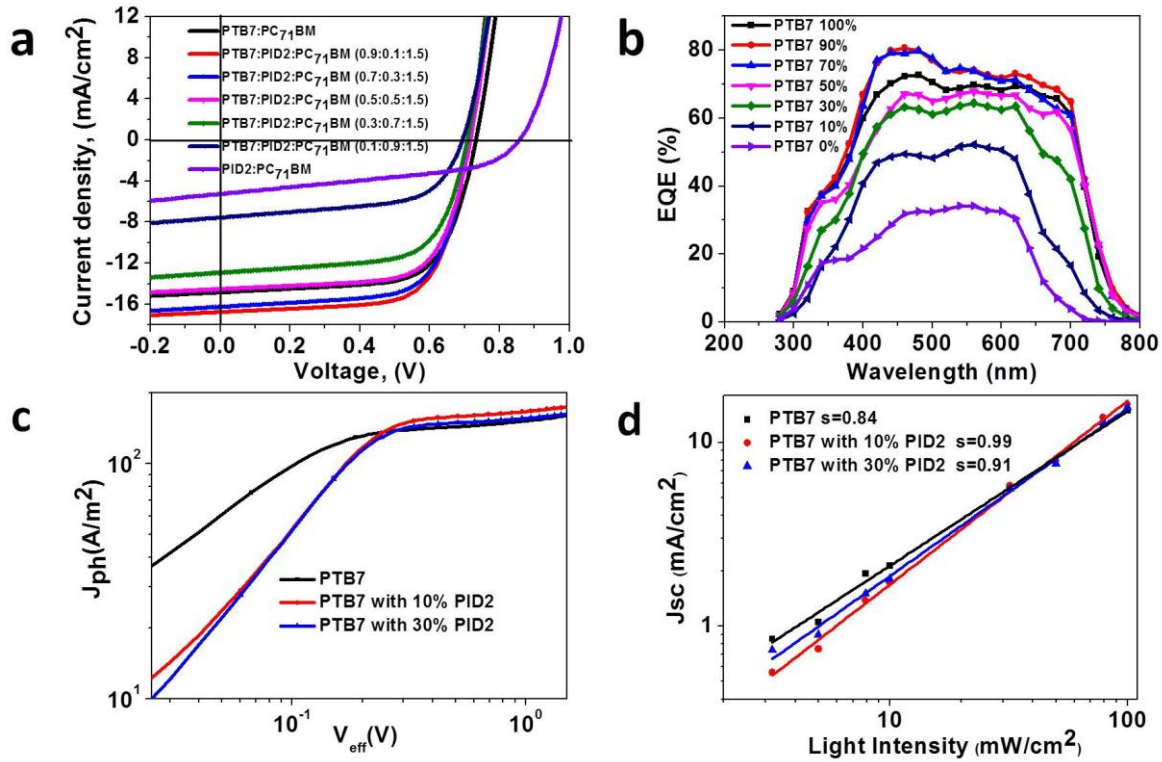


Figure 12 | Photovoltaic performance. **a**, Current-voltage characteristics of ternary solar cells with different polymer mixture ratios. **b**, EQE curves of ternary PTB7:PID2:PC₇₁BM blend different PID2 contents. **c**, Photocurrent density (J_{ph}) versus effective voltage (V_{eff}) characteristics. **d**, Dependence of J_{sc} on light intensity of ternary system with different polymer ratios.

Table 7 | Summary of solar cell parameters of ternary PTB7:PID2:PC₇₁BM blend with different ratios of PTB7:PID2.

<i>PTB7:PID2:PC₇₁BM</i>	<i>J_{sc} (mA/cm²)</i>	<i>V_{oc} (V)</i>	<i>FF (%)</i>	<i>PCE (%)</i>
1:0:1.5	15.0	0.72	67.1	7.25
0.9:0.1:1.5	16.8	0.72	68.7	8.22
0.7:0.3:1.5	16.3	0.71	68.0	7.88
0.5:0.5:1.5	14.5	0.72	68.3	7.10
0.3:0.7:1.5	12.9	0.71	66.1	6.04
0.1:0.9:1.5	7.56	0.70	59.5	3.12
0:1:1.5	5.27	0.86	44.4	2.01

To study changes in J_{sc} , external quantum efficiency (EQE) of the ternary blend devices was measured and the results are illustrated in Figure 12b. Ternary systems with up to 30% PID2 incorporation showed similar thicknesses (around 130 nm) to PTB7:PC₇₁BM binary device. Thus direct comparison between the EQE results is meaningful. Unlike the trend we observed in the UV-vis absorption spectra, incorporation of 10% PID2 into PTB7:PC₇₁BM blend led to increased EQE values over the whole wavelength region. The EQE values were enhanced most in the region between 400 nm to 550 nm where PC₇₁BM exhibits high absorption. Since incorporation of 10% PID2 only led to better absorption from 500 nm to 620 nm in Figure 1d, the increase in EQE between 400 nm to 550 nm at low PID2 content should not result from additional absorption enhancement of PID2. Instead, this result indicated that the small amount of PID2 played the role of hole relay between PC₇₁BM and PTB7 via its HOMO orbital. The energy diagram clearly showed that the HOMO energy level difference between PC₇₁BM and PTB7 is about 0.95 eV, too large for an effective hole transfer. The HOMO energy level of PID2 is almost positioned in the middle of the PTB7 and PC₇₁BM, forming the cascade HOMO energy levels for more effective extraction of holes from PC₇₁BM (Figure 11b)³⁵. To prove this, we measured film photoluminescence (PL) of PID2, PTB7 and PTB7:PID2 (both 0.9:0.1 and 0.7:0.3 ratios) excited at 610 nm (maximum absorption for PID2). The results are shown in Figure S7a. Generally, if energy transfer between PID2 and PTB7 exists, one would expect increased PL emission for PTB7 with decreased PL emission for PID2 assuming that the quantum yields of the two polymers are similar. On the other hand, if photoinduced electron transfer from HOMO energy level of PTB7 to HOMO energy level of excited PID2 exists (hole transfer from PID2 to PTB7) (Figure S7b), emission of PID2 would be quenched without increase of PTB7 PL signal. PID2 showed a strong emission with a maximum at 680nm while PTB7 exhibited a weak PL emission signal with a peak at 760 nm. PL of PID2 was completely quenched while PL of PTB7 remained almost the same in PTB7:PID2 blends (both 0.9:0.1 and 0.7:0.3). The results confirmed that photoinduced electron transfer from PTB7 to PID2 (hole transfer from PID2 to PTB7) existed other than energy transfer between PID2 and PTB7. Since hole transfer from PC₇₁BM to PID2 was already demonstrated by 2.01% device performance for PID2:PC₇₁BM, we could conclude that holes could transfer from PC₇₁BM to PID2 and finally to PTB7. In addition, we fabricated a solar cell using PTB7 and PID2 at 1 to 1 ratio only and achieved a PCE at 0.051%, with a V_{oc} at 0.65 V, a J_{sc} at

0.192 mA/cm² and a *FF* at 40.8%. Although the PCE was poor due to the fact that PID2 was designed as a donor material instead of an acceptor, it again proved that charge separation and transport between PTB7 and PID2 happened at their interfaces. This point is further reinforced by an improved EQE values from 400 nm to 650 nm while remained similar values from 650 nm to 750 nm when PIB2 content was increased to 30%. The integrated J_{sc} values from EQE spectrum for PTB7:PC₇₁BM (1.0:1.5), PTB7:PID2:PC₇₁BM (0.9:0.1:1.5), PTB7:PID2:PC₇₁BM (0.7:0.3:1.5) devices were 15.1 mA/cm², 16.3 mA/cm², 15.8 mA/cm², respectively. This is within 3% difference from measured J_{sc} values, indicating that *J-V* measurements in this work are reliable. In addition, since devices with low PID2 content (10% and 30%) showed higher or comparable EQE values from 650 nm to 750 nm compared to PTB7:PC₇₁BM while higher PID2 content (>30%) led to lower EQE values from 400 nm to 650 nm, we can again conclude that changes in light absorption is not the only cause for J_{sc} changes in our ternary blend system, the cascade energy levels is also important to PCE changes.

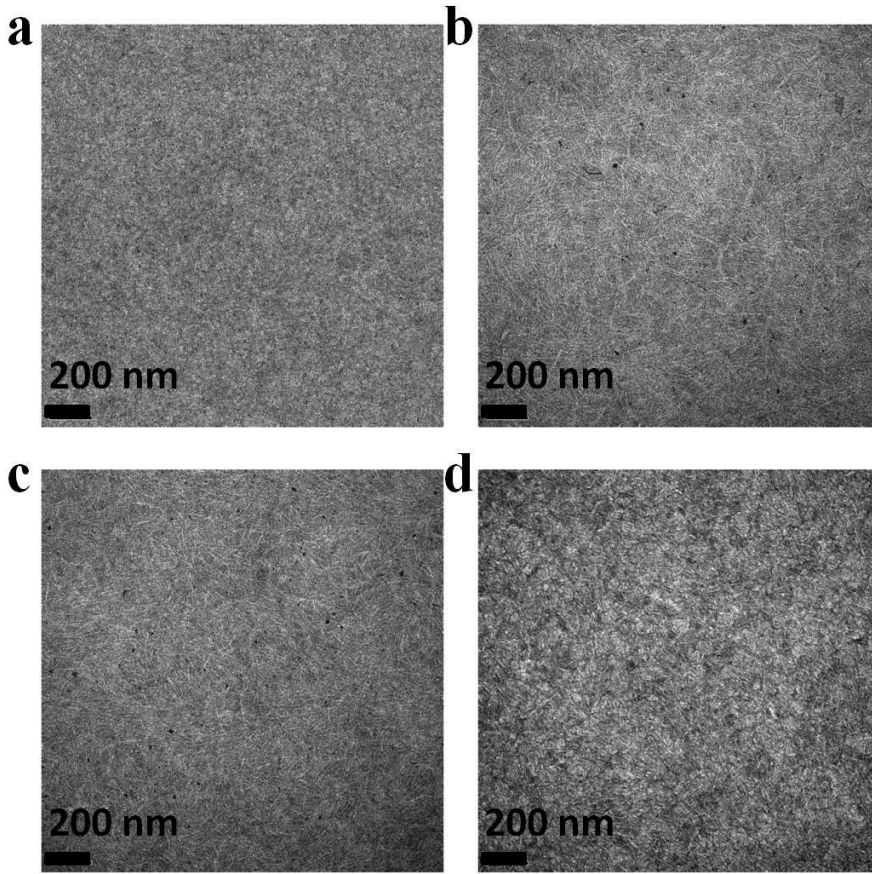


Figure 13 | TEM characterization. TEM images of **a**, PTB7:PC₇₁BM (1:1.5). **b**, PTB7:PID2:PC₇₁BM (0.9:0.1:1.5). **c**, PTB7:PID2:PC₇₁BM (0.7:0.3:1.5). **d**, PID2:PC₇₁BM (1:1.5).

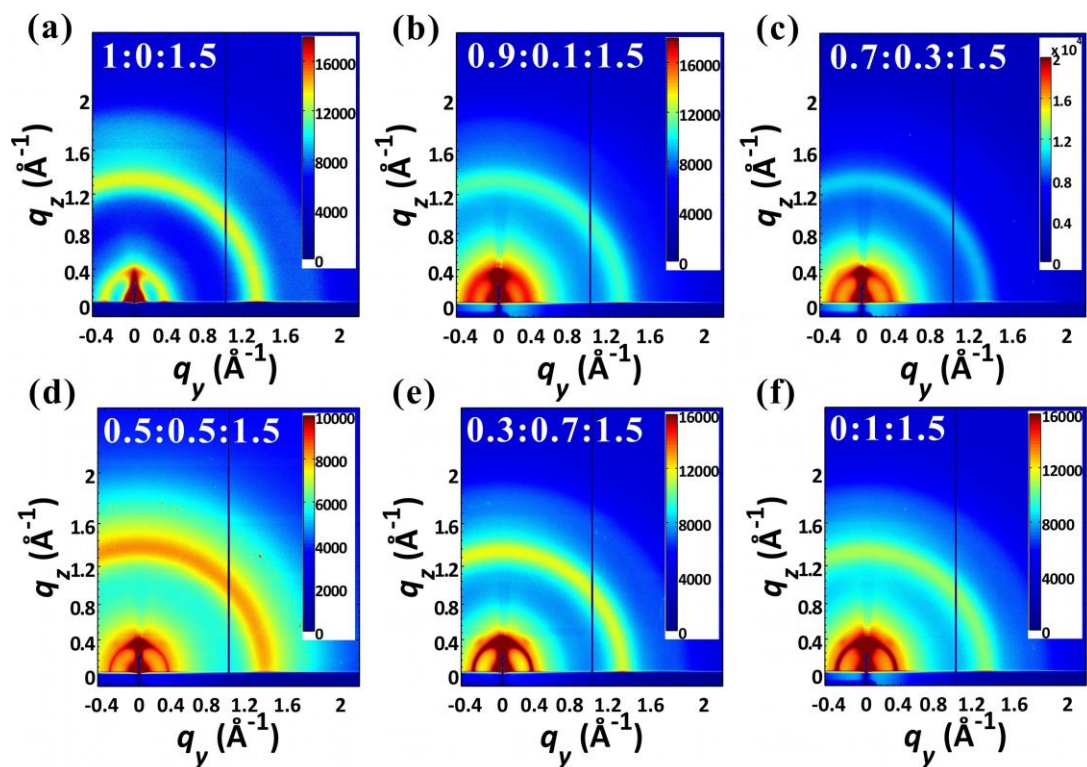
To gain more insight into light absorption and exciton dissociation process, we determined the saturation current density (J_{sat}) and charge dissociation probabilities $P(E,T)$ of PTB7:PC₇₁BM (1:1.5), PTB7:PID2:PC₇₁BM (0.9:0.1:1.5), PTB7:PID2:PC₇₁BM (0.7:0.3:1.5) devices. Figure 12c reveals photocurrent density (J_{ph}) versus effective voltage (V_{eff}) curves for solar cells used in this work. Here J_{ph} is defined as $J_{ph} = J_L - J_D$, where J_L and J_D are the photocurrent densities under illumination and in the dark, respectively. V_{eff} is defined as $V_{eff} = V_0 - V_a$, where V_0 is the voltage where J_{ph} equals zero and V_a is the applied bias voltage³⁶. If we assume that all the photogenerated

excitons are dissociated into free charge carriers and collected by electrodes at a high V_{eff} (i.e. $V_{eff} = 2$ V), saturation current density (J_{sat}) will only be limited by total amount of absorbed incident photons. The J_{sat} values for the three devices were 169 A m^{-2} (0% PID2 content), 180 A m^{-2} (10% PID2 content) and 169 A m^{-2} (30% PID2 content), respectively. Further increasing the content of PID2 showed dramatic decrease in J_{sat} values (Figure S8). The larger J_{sat} value of device with 10% PID2 content would suggest enlarged overall exciton generation while the unchanged J_{sat} value of device with 30% PID2 content suggested the same overall exciton generation compared to the control device^{13,35}. It should be pointed out that even though J_{sat} increased at 10% PID2 content by 6.5%, the increased J_{sat} was still not enough to account for the overall enhancement in J_{sc} (12%). Since both 10% and 30% contents of PID2 showed much larger J_{sc} values than the control device, the J_{ph} results further confirmed the assertion that both absorption change and energy cascade contributed to the change in current density in this work. The $P(E, T)$ is determined by normalizing J_{ph} with J_{sat} (J_{ph} / J_{sat})³⁷. The $P(E, T)$ values under J_{sc} condition for the three devices were 88.0%, 90.2%, 91.2%, respectively, while the $P(E, T)$ value for PID2:PC₇₁BM device was only 65.6%. The results showed that incorporation of PIB2 at low contents facilitated charge dissociation in ternary devices.

In addition to light absorption and exciton dissociation, we also measured J_{sc} as a function of illumination intensities for the three devices to monitor the changes in recombination kinetics. Quantitatively, J_{sc} follows a power-law dependence on light intensity ($J_{sc} \propto P_{light}^S$)^{38,39}. In general, linear scaling of photocurrent with P_{light} would suggest weak bimolecular recombination while sublinear scaling of photocurrent with P_{light} indicates partial loss of charge carriers during charge transport process due to bimolecular recombination. As shown in Figure 12d, the exponential factors of PTB7:PC₇₁BM (1:1.5), PTB7:PID2:PC₇₁BM (0.9:0.1:1.5), PTB7:PID2:PC₇₁BM (0.7:0.3:1.5) devices were 0.84, 0.99, 0.91, respectively. Thus, bimolecular recombination was weakest in devices with 10% of PID2. Compared to PTB7:PC₇₁BM, device with 30% of PID2 also showed decreased bimolecular recombination. Changes in bimolecular recombination help to explain the increased J_{sc} and FF in the ternary blend system. This is in good agreement with hole mobility data of these devices, measured with the structure ITO/ PEDOT:PSS/ PTB7:PID2/ Al using space-charge-limited current (SCLC) model⁴⁰. As shown in Figure S9, hole mobility increased from $5.42 \times 10^{-4} \text{ cm}^2 \text{ V}^{-1} \text{ s}^{-1}$ (PTB7) to $7.75 \times 10^{-4} \text{ cm}^2 \text{ V}^{-1} \text{ s}^{-1}$ (PTB7:PID2 /0.9:0.1) and $8.72 \times 10^{-4} \text{ cm}^2 \text{ V}^{-1} \text{ s}^{-1}$ (PTB7:PID2 /0.7:0.3), while hole mobility of PID2 was only $2.71 \times 10^{-4} \text{ cm}^2 \text{ V}^{-1} \text{ s}^{-1}$. The improved charge transport property is the result of the cascade energy levels in the ternary system and improved morphology as discussed below³⁵.

Transmission electron microscopy (TEM) was first used to probe morphology of the ternary blend (Figure 13). Both PTB7:PID2:PC₇₁BM (0.9:0.1:1.5) and PTB7:PID2:PC₇₁BM (0.7:0.3:1.5) films showed fibrous features while no such structure was observed in PTB7:PC₇₁BM or PID2:PC₇₁BM devices. This seems to indicate that the PID2 plays the role of template for the formation of fibrous structure in PTB7. The fine dispersed fibrils were previously found beneficial to exciton separation and charge transport^{41,42}. Tapping mode atomic force microscopy (AFM) height and phase images of the ternary system showed that the root-mean-squared (RMS) roughness of the four devices based on PTB7:PC₇₁BM (1:1.5), PTB7:PID2:PC₇₁BM (0.9:0.1:1.5), PTB7:PID2:PC₇₁BM (0.7:0.3:1.5) and PID2:PC₇₁BM (1:1.5) was 0.87 nm, 1.06 nm, 1.02 nm and 2.31 nm, respectively. Although PID2 showed higher roughness than PTB7 when mixed with PC₇₁BM, blending PID2 into PTB7:PC₇₁BM up to 30% did not cause any significant change of surface roughness of the host blend. X-ray scattering techniques helped to understand changes in molecular packing, structure ordering and domain sizes in our devices. Shown in Figure 4 and 5 are the 2D grazing incidence wide-angle X-ray scattering (GIWAXS) patterns and resonant soft X-ray scattering (RSoXS) profiles of the ternary PTB7:PID2:PC₇₁BM blend films with different PID2 content. In the 2D GIWAXS pattern of PTB7:PC₇₁BM (1:1.5) blend film (Figure 14a), a broad arc-like

scattering arising from the Bragg diffraction of periodic PTB7 layers was observed at $q_y \sim 0.36 \text{ \AA}^{-1}$, suggesting the preferential face-on conformation, whereas the 2D GIWAXS pattern of PID2:PC₇₁BM (1:1.5) blend film (Figure 14f) exhibited a ring-like layering peak at $q_z \sim 0.34 \text{ \AA}^{-1}$ and two off-axis scattering spots located at $(\pm 0.27, 0.38) \text{ \AA}^{-1}$, indicating the formation of PID2 bilayer ordering with a preferential edge-on orientation similar to that observed in PCDTBT⁴³. Since the full width at half maximum (FWHMs) of scattering peak, Δq , correlates to the nanocrystallite size *via* Scherrer equation⁴⁴⁻⁴⁶, the narrower Δq of PID2 layering peak indicated that PID2 could form larger nanocrystallite sizes in the blend film than PTB7. Further RSoXS studies provided access to the spatial dimensions of phase-separated domains^{45,46}. The RSoXS profile of the PTB7:PC₇₁BM blend film showed a diffuse scattering at $q \sim 0.006 \text{ \AA}^{-1}$, while that of the PID2:PC₇₁BM blend film exhibited a well-defined peak centered at a larger q value of $\sim 0.003 \text{ \AA}^{-1}$ (Figure 5). This illustrates that the phase-separated domains in PID2:PC₇₁BM blend film were larger than those in PTB7:PC₇₁BM blend film. However, upon incorporating a small amount of PID2 copolymers into PTB7:PC₇₁BM blend film (PTB7:PID2:PC₇₁BM (0.9:0.1:1.5)), PID2 copolymers showed little influence on the crystalline structures of both conjugated polymers and PC₇₁BM while induced the formation of smaller phase separated domains. These smaller domains would increase the area of interfaces between polymer donors and fullerene acceptors, thus facilitating exciton dissociation and lead to an improved performance. This is in accordance with our exciton dissociation results. Further increasing the amount of PID2 copolymers, PID2:PC₇₁BM blends gradually phase separated out of the PTB7:PC₇₁BM blends and formed individual blend region in the films. Both larger conjugated polymer nanocrystallites and phase-separated domains formed in the ternary blend films and low PID2 mobility resulted in decreased device efficiency at high PID2 content. Taken together, these observations of morphological changes in the ternary blend films support our hypothesis that the incorporation of PID2 at low contents could facilitate charge dissociation and transport. This also helps to explain the tendency of performance change as a function of the PID2 contents in our device.



PTB7:PID2:PC ₇₁ BM	q_r (\AA^{-1})	Δq_r (\AA^{-1})	D_L (\AA)	q_z (\AA^{-1})	Δq_z (\AA^{-1})	D_L (\AA)
1:0:1.5	0.363 ± 0.009	0.172	34.4	—	—	—
0.9:0.1:1.5	0.350 ± 0.009	0.175	33.8	—	—	—
0.7:0.3:1.5	0.332 ± 0.009	0.216	27.4	0.329 ± 0.009	0.076	77.7
0.5:0.5:1.5	0.349 ± 0.009	0.140	42.3	0.333 ± 0.009	0.046	128.4
0.3:0.7:1.5	0.344 ± 0.009	0.073	81.2	0.348 ± 0.009	0.043	138.8
0:1:1.5	0.344 ± 0.009	0.033	180.8	0.336 ± 0.009	0.041	145.5

Figure 14 | 2D GIWAX patterns of ternary films on PEDOT:PSS-modified Si substrates. a, PTB7:PC₇₁BM (1:1.5). **b,** PTB7:PID2:PC₇₁BM (0.9:0.1:1.5). **c,** PTB7:PID2:PC₇₁BM (0.7:0.3:1.5). **d,** PTB7:PID2:PC₇₁BM (0.5:0.5:1.5). **e,** PTB7:PID2:PC₇₁BM (0.3:0.7:1.5). **f,** PID2:PC₇₁BM (1:1.5).

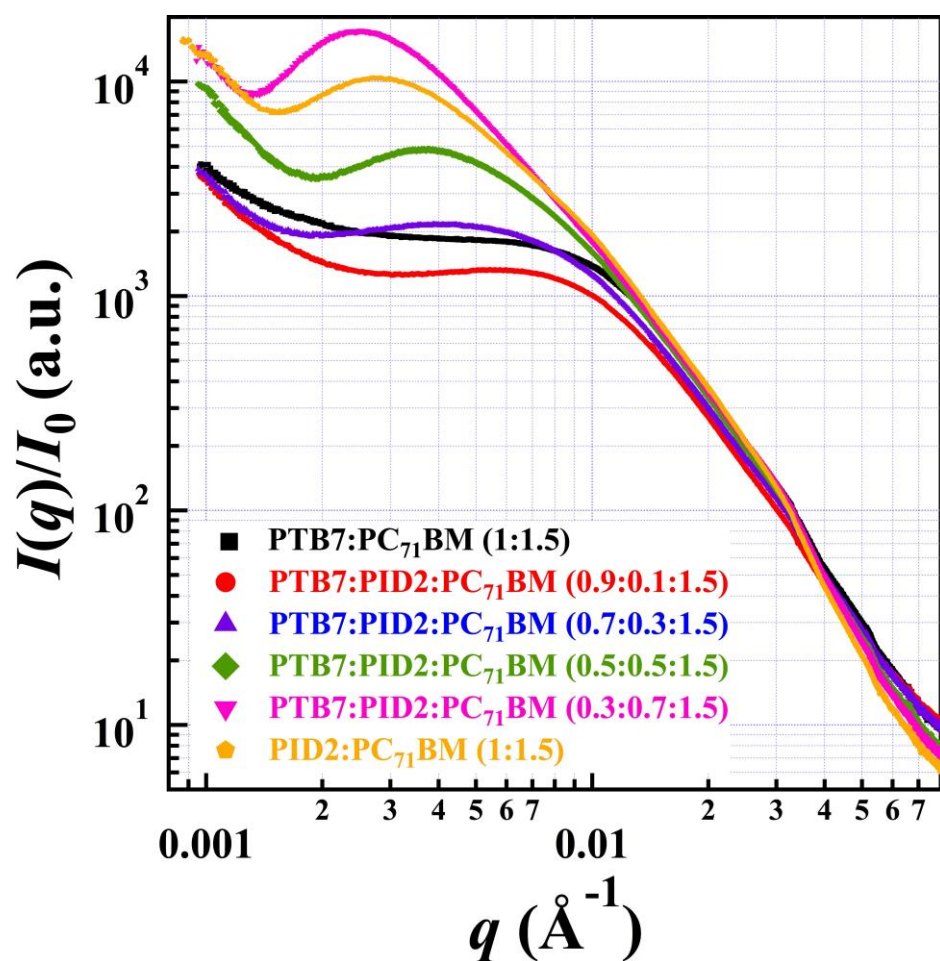


Figure 15 | RSoXS profiles of the ternary films.

Archival publications (published) during reporting period:

1. Son, Hae Jung; Carsten, Bridget; Jung, In Hwan; Yu, Luping, “[Overcoming efficiency challenges in organic solar cells: rational development of conjugated polymers](#) Full Text”, *Energy & Environmental Science* (2012), 5(8), 8158-8170. DOI: [10.1039/C2EE21608F](#)

2. Luyao Lu, Zhiqiang Luo, Tao Xu, Luping Yu **Cooperative Plasmonic Effect of Ag and Au Nanoparticles on Enhancing Performance of Polymer Solar Cells**, *Nano Lett.*, 13, 59-64, 2013. DOI: [10.1021/nl3034398](https://doi.org/10.1021/nl3034398), Published: JAN 2013
3. Hae Jung Son, Luyao Lu, Wei Chen, Tao Xu, Tianyue Zheng, Bridget Carsten, Joseph Strzalka, Seth B. Darling, Lin X. Chen and Luping Yu, **Synthesis and Photovoltaic Effect of Semi-Ladder-Conjugated Polymers with High Solar Cell Efficiencies**, *Adv. Mater.*, (2013), 25(6), 838-843. DOI: [10.1002/adma.201204238](https://doi.org/10.1002/adma.201204238), Published: FEB 13 2013.
4. Luyao Lu, Tao Xu, Ju Min Lee, Zhiqiang Luo, Feng He, Hyung Il Park, In Hwan Jung, Sang Ouk Kim, Luping Yu, **"The Role of N-Doped Multi-wall Carbon Nanotubes in Achieving Highly Efficient Polymer Bulk Heterojunction Solar Cells"**, *Nano Lett.*, 2013, 13 (6), pp 2365–2369, DOI: [10.1021/nl304533j](https://doi.org/10.1021/nl304533j), May 2, 2013.
5. Luyao Lu, Luping Yu, **Polymers for solar cells**, *Encyclopedia for Polymeric Nanomaterials*, 2014, 1-9.
6. Luyao Lu, Tao Xu, Wei Chen, Erik S. Landry, Luping Yu, **[Ternary blend polymer solar cells with enhanced power conversion efficiency](https://doi.org/10.1038/nphoton.2014.172)**, *Nature Photonics*, 8, 716–722, (2014), doi:10.1038/nphoton.2014.172
7. Tao Xu, Luyao Lu, Tianyue Zheng, Jodi M. Szarko, Lin X. Chen, Luping Yu, **Tuning the Polarizability in the Solar Cell Polymers with Artificial Sweetener Thiophenesacchrin**, *Adv Functional Mater.*, 2014, 22, 3432-3437. DOI: [10.1002/adfm.201303688](https://doi.org/10.1002/adfm.201303688)
8. Tao Xu and Luping Yu, **How to design low band gap polymers for highly efficient organic solar cells**, *Materials Today*, 17 (1), 11-15 (2014). <http://dx.doi.org/10.1016/j.mattod.2013.12.00>
9. Luyao Lu, and Luping Yu, **Understanding low bandgap polymer PTB7 and optimizing polymer solar cells based on it**, *Adv. Mater.*, 2014, 26, 4413-4430, doi:10.1002/adma.201400384.
10. In Hwan Jung, Wai-Yip Lo, Jaeyoung Jang, Wei Chen, Donglin Zhao, Erik S. Landry, Luyao Lu, Dmitri V. Talapin, Luping Yu, **Search for Design Principles of Electron Accepting Polymers for All-Polymer Solar Cells**, *Chem. Mater.*, 2014, 26 (11), pp 3450–3459, DOI: 10.1021/cm500832h
11. Rolczynski, Brian; Szarko, Jodi; Son, Hae Jung; Yu, Luping; Chen, Lin X, **Effects of Exciton Polarity in Charge Transfer Polymer/PCBM Bulk Heterojunction Films**, *J Phys. Chem. Lett.*, 2014, 5, 1856–1863. [dx.doi.org/10.1021/jz5005957](https://doi.org/10.1021/jz5005957)
12. Luyao Lu, Tao Xu, In Hwan Jung, Luping Yu, **Match the interfacial energy levels between hole transport layer and donor polymer to achieve high solar cell performance**, *J. Phys. Chem. C.*, 2014, 118 (40), pp 22834–22839. DOI: 10.1021/jp5036663.
13. Tianyue Zheng, Luyao Lu, Nicholas E. Jackson, Sylvia J. Lou, Lin X. Chen and Luping Yu, **The Roles of Quinoidal Character and Regioregularity in Determining the Optoelectronic and Photovoltaic Properties of Conjugated Co-polymers**, *Macromol.*, 2014, 47 (18), pp 6252–6259, DOI: 10.1021/ma501152v
14. JUNG, IN HWAN; Zhao, Donglin; Jang, Jaeyoung; Chen, Wei; Landry, Erik; Lu, Luyao; Talapin, Dmitri; Yu, Luping, **Development and structure/property relationship of new electron accepting polymers based on thieno[2',3':4,5]-pyrido[2,3-g]thieno[3,2-c]quinoline-4,10-dione for all-polymer solar cells**, *Chem Sci*, Submitted.
15. Luyao Lu, Tianyue Zheng, Qinghe Wu, Alexander M Schneider, Donglin Zhao, and Luping Yu **Recent advances in bulk heterojunction polymer solar cells**, (Invited article) *Chem. Rev.* Submitted.
16. Luyao Lu¹, Wei Chen^{2,3}, Tao Xu¹, Luping Yu¹ **High performance ternary blend polymer solar cells involving both energy transfer and hole relay processes**, *Nature Commun.*, In revision.

Changes in research objectives, if any: None

Change in AFOSR program manager, if any: None

Extensions granted or milestones slipped, if any: None

Include any new discoveries, inventions, or patent disclosures during this reporting period (if none, report none): 1

Luping Yu and Haejung Son, "SEMICONDUCTING POLYMERS", PCT Application Pending.

To: technicalreports@afosr.af.mil
Subject: Final Performance Report to Dr. Charles Lee

Contract/Grant Title: "Semiconducting Polymers solar cell"

Contract/Grant #: FA9550-12-1-0061

Reporting Period: April 01, 2012 to March 31, 2015

Prepared by Luping Yu

Department of Chemistry, The University of Chicago, 929 E 57th Street, Chicago, IL 60637.

Abstract:

In the past three years, our research project sponsored partially by AFOSR has been focused on developing low bandgap semiconducting polymers as both the donor and acceptor materials for BHJ solar cells. Research effort were also devoted to establish structure-property relationship and develop approaches to optimize light harvest, charge separation and charge collection, thus the overall power conversion efficiency (PCE). We have made very important contributions to the field and developed a series of new semiconducting polymers for highly efficient ternary polymer solar cells. We also discovered cooperative plasmonic effect of dual precious metal nanoparticles in enhancing PCE of BHJ solar cells. Multiwall carbon nanowire were introduced to significantly enhance the charge collection. These results have had significant impact to the area. Several polymers developed in our lab are now widely investigated around world. Seven of the papers published are highly cited as indicated by SCI.

Accomplishments:

In the past three years, we made significant progress in four research directions in OPV solar cells.

1. Establishing structure property relationship between Low Bandgap Polymers and Their Organic Solar Cells Performance.

A key challenge of the development of organic photovoltaic devices is obtaining a predictive understanding of the relationship between polymeric structure of the donor material and device performance. Among the factors that may influence solar energy conversion, the nature of electron donating and accepting materials and the morphology of the composites play the crucial roles in determining the final performance of the devices. In recent years, fullerene derivatives such as [6,6]-phenyl C₇₁-butyric acid methyl ester (PC₇₁BM) have been widely adopted as electron acceptors due to their low lying energy levels and relatively high electron affinity and mobility. It was also found that addition of a small amount of high boiling point solvent, generally 1,8-diiodooctane (DIO), can reliably improve the morphology of most of the composite systems.^{19,20} Thus, we focus our main effort on understanding the structure/property correlation of electron donor materials in order to develop innovative strategies for achieving high performance solar cells.

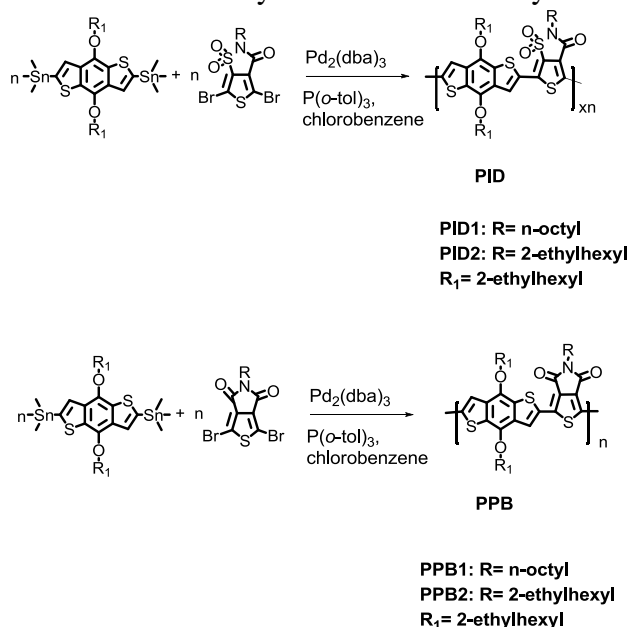
In previous studies, a linear correlation of the calculated dipole moment change between the ground and excited states $\Delta\mu_{ge}$ of single repeating units in charge transfer polymers was established, suggesting a larger local $\Delta\mu_{ge}$ could defray a part of exciton binding energy, leading to a higher power conversion efficiency (PCE). We further synthesized a new low bandgap polymers incorporating an artificial sweetener derivatives, *N*-alkyl, 3-oxothieno[3,4-*d*]isothiazole 1,1-dioxide (TID). Semi-empirical calculations on the local dipole moment change between ground and excited states ($\Delta\mu_{ge}$) in the repeating units of the new polymer indicate that the replacement of the carbonyl by a sulfonyl group leads to larger $\Delta\mu_{ge}$ values. The resulting polymers exhibit diminished power conversion efficiency (PCE) from bulk heterojunction (BHJ) solar cells with PC₇₁BM as acceptor, which extends the correlation between PCE and $\Delta\mu_{ge}$ of

single repeating units in p-type polymers to a new regime. Detailed studies show that the strongly electron withdrawing sulfonyl group is detrimental to charge separation in alternating copolymers containing TID unit.

Semi-empirical calculations on the local dipole moment change between ground and excited states ($\Delta\mu_{ge}$) in the repeating units of the new polymer indicate that the replacement of the carbonyl by a sulfonyl group leads to larger $\Delta\mu_{ge}$ values. The resulting polymers exhibit diminished power conversion efficiency (PCE) from bulk heterojunction (BHJ) solar cells with PC₇₁BM as acceptor, which extends the correlation between PCE and $\Delta\mu_{ge}$ of single repeating units in p-type polymers to a new regime. Detailed studies show that the strongly electron withdrawing sulfonyl group is detrimental to charge separation in alternating copolymers containing TID unit.

1.1. Synthesis of polymers: The TID unit was prepared according to a modified literature procedure.²⁶ In order to anchor alkyl side chains on the original artificial sweetener unit, the phase transfer catalyst 15-crown-5 was used to achieve a relatively high conversion yield. Two different solubilizing alkyl side chains were used, octyl and 2-ethylhexyl (used in PID1 and 2, respectively). The final monomer TID was prepared via a modified bromination procedure in the presence of strong Brønsted acids (See Scheme S1 for synthetic details). The BDT and TPD units were synthesized according to previous published procedures.^{7,27} Polymers were synthesized via Stille polycondensation using Pd₂(dba)₃/P(o-tolyl)₃ catalyst in refluxing chlorobenzene (CB) for 48 hrs.^{6,28} For comparison, another known polymer with a relatively large $\Delta\mu_{ge}$ value (PPB) was also synthesized and characterized in the same conditions as Scheme 1.

Scheme 1 Synthetic routes of Polymers.

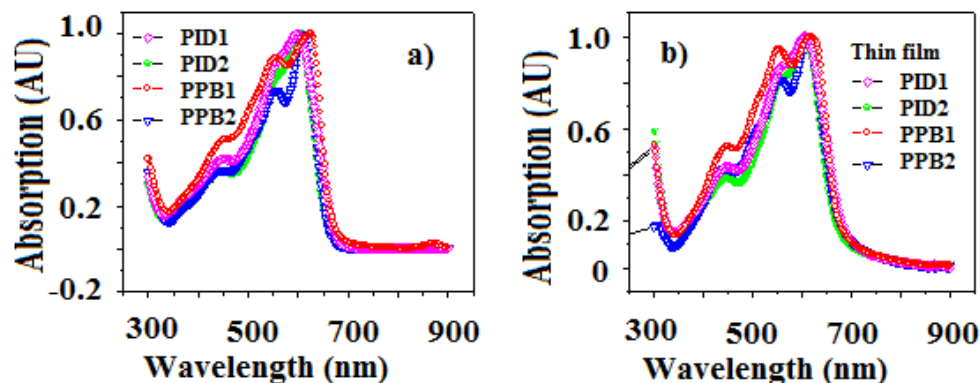


1.2 Optical and electrical properties of polymers

As shown by Gel permeation chromatography (GPC) measurements, these polymers exhibit number-averaged molecular weights between 12.0 and 18.6 kg/mol with a dispersity index (\bar{D}) around 2 (Table S1). The structures of polymers were confirmed by ¹H NMR spectra (Figure S1-S11) and elemental analyses (Table S2). Both the solution and thin-film optical absorption spectra of the polymers are presented in Figure 1. All polymers showed similar absorption range from 320 to 700 nm, and the absorption edge was nearly identical. The absorption maximum of the PID polymers was slightly blue-shifted compared to the PPB polymers. The cyclic voltammetry (CV) (Figure S12) studies indicated that the HOMO energy levels of PID1 and PID2

were at -5.44 and -5.52 eV, approximately 0.1 eV lower than their corresponding PPBs; while the LUMO energy levels were at -3.55 eV and -3.50 eV, respectively.

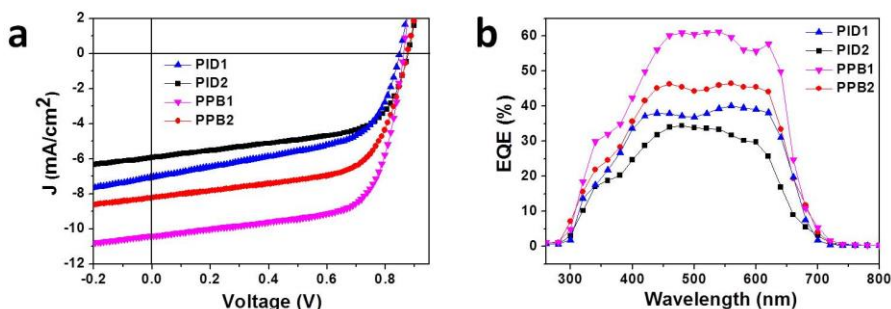
Figure 1. Normalized UV-vis absorption spectra of the polymers (a) in diluted chloroform solution and b) in pristine polymer films.



1.3 Current-Voltage (*J*-*V*) characteristics of the polymer solar cells

The photovoltaic properties were investigated in the device structure ITO/PEDOT:PSS/polymer:[6,6]-phenyl-C71-butyric acid methyl ester (PC₇₁BM)/Ca/Al. All solar cell data used in comparison of physical properties were determined based on this device structure. The active layers of ~100 nm were spin-coated from 10 mg/mL chlorobenzene (CB) and DIO (v/v, 97:3) solutions. The corresponding *J*-*V* curves of the four polymer solar cells under AM 1.5G condition at 100 mW/cm² are presented in Figure 2a. Representative characteristics of solar cells are summarized in Table 1. Devices fabricated from PID1, PID2, PPB1 and PPB2 showed best PCE values at 3.28%, 3.05%, 5.97%, and 4.48%, respectively. Figure 2b depicts the external quantum efficiency (EQE) curves of the four solar cells. The PPB1 showed highest EQE values around 60% within the spectral range from 450 to 650 nm while PID2 showed the lowest EQE values ca 30%. Changes in EQE curves are in good agreement with the observed *J*_{sc} values from the four polymers. Hole mobility of all four polymers, measured using space charge limited current (SCLC)²⁹ method, were $\sim 2.42 \times 10^{-4}$, 2.71×10^{-4} , 3.69×10^{-4} and 3.34×10^{-4} cm² V⁻¹ s⁻¹ for PID1, PID2, PPB1 and PPB2, respectively (Figure S13). Along with the EQE curves, the mobility values match with the *J*_{sc} trend well. Although PIDs exhibits high open circuit voltage due to a low HOMO energy level, small current density and low fill factor limit the overall solar cell performance.

Figure 2. (a) Characteristic J - V curves of the four solar cells and (b) EQE curves of the four solar cells.



To ensure that the comparison of solar cell performance is meaningful, the morphologies of these polymer films were optimized for the device performance by using organic additive in the film fabrication.³⁰ As shown in the transmission electron microscopy (TEM) images of blend films with and without DIO in Figure S14, all four solar cells with DIO exhibit fine phase separations while severe phase segregation was observed in the blend films without DIO, leading to almost zero photovoltaic effect (Figure S15).

Table 1. Comparison of Photovoltaic Parameters of TID and TPD-containing Polymers in the Blend with PC₇₁BM (CB/DIO, Polymer/PCBM = 1:1.5 Weight ratio).

Polymer	HOMO* (eV)	LUMO* (eV)	V_{oc} (V)	J_{sc} (mA/cm^2)	FF (%)	PCE (%)
PID1	5.44	3.55	0.85	7.06	54.7	3.28
PID2	5.52	3.40	0.88	5.94	58.6	3.05
PPB1	5.38	3.55	0.86	10.40	66.6	5.97
PPB2	5.40	3.55	0.88	8.23	62.2	4.48

Note: * From CV data.

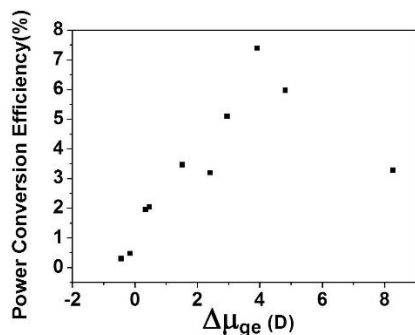
1.4. Correlation of $\Delta\mu_{ge}$ change and solar cell performance

The results shown are those for the optimized solar cells and therefore it is believable to use them to compare with other similarly optimized systems. The dipole moments of single repeating units in PID1 and PPB1 were calculated using the procedure in our previous study.¹⁸ The results are presented together with the optimized PCE values in Table 2 along with data for other polymers previously reported. To simulate the randomized orientation of the asymmetric TID unit, the average dipole moment for each polymer repeating unit was determined and used for the analysis of dependence of PCE values on dipole changes. Both the ground and excited state dipole moments were calculated for each polymer repeating unit in the series. The overall change $\Delta\mu_{ge}$ was calculated by accounting for the changes of the dipole along each coordinate axis. Our previous data indicated that a linear correlation between $\Delta\mu_{ge}$ and PCEs exists, where the PTB7 showed the highest values of both PCE (7.4%) and $\Delta\mu_{ge}$ (3.92 D). Such a trend was explained as an indication of local electron density gradient that defrays a part of the exciton binding energy, which enabled the cation generation in these polymers via intra-chain charge transfer even in solution.³² However, the results shown here indicate that further increasing $\Delta\mu_{ge}$ actually lowers PCE in the corresponding solar cell. PPB1 has a larger $\Delta\mu_{ge}$, but a lower PCE value of 5.97% than PTB7. The most notable dipole moment change $\Delta\mu_{ge}$ comes from the TID-based polymer PID1 which is almost twice as large as PTB7. However, it exhibits a PCE value only slightly above 3%, indicating that the linear relationship of $\Delta\mu_{ge}$ vs PCE did not extend (Figure 3) into the larger $\Delta\mu_{ge}$ regime.

Table 2. Calculated Single Repeating Unit Dipole Moments and the Corresponding Optimized PCE Values.

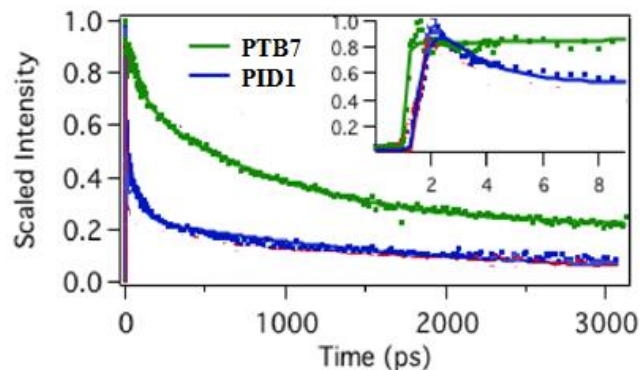
Polymer	μ_g (D)	μ_e (D)	$\Delta\mu_{ge}$ (D)	PCE (%)
PTB2	3.60	6.37	2.96	5.10
PTB7	3.76	7.13	3.92	7.40
PTBF2	3.35	5.45	2.41	3.20
PBB3	0.61	0.82	0.47	2.04
PBIT1	4.46	4.80	0.34	1.96
PBIT3	6.99	6.83	-0.16	0.47
PBTZ1	0.88	2.41	1.52	3.46
PBTZ2	1.92	1.48	-0.44	0.29
PPB1	3.58	7.60	4.82	5.97
PID1	4.69	12.08	8.26	3.28

Figure 3. Correlation of PCE values with calculated dipolar changes of polymer repeating unit.



To explain these trends, we can reason that a higher $\Delta\mu_{ge}$ implies a larger displacement of hole-electron pair in an exciton, lower Coulombic interactions between charges, and hence a reduced exciton binding energy. In addition, the introduction of strong electron withdrawing group simultaneously enhances the polarizability of excitons and lowers the polymer LUMO energy level. Ideally, the polarized exciton facilitates an electron transfer from the polymer blocks with lower electron affinity to the adjacent blocks with higher electron affinity and then to fullerene. However, the sulfonyl group exhibits strong electron accepting ability, leading to a much larger $\Delta\mu_{ge}$ (8.26 D) than PTB7 (3.92 D) and a highly polarized exciton with a larger effective separation of charges within a polymer repeating unit and beyond. When $\Delta\mu_{ge}$ is too large, the polarized polymer repeating units could also acts as trapping or recombination centers for electrons and compete with the electron injection to the fullerene. This happens in the PPB and PID series of polymers, particularly PID1, with LUMO energy nearly 0.24 eV lower than that of PTB7. Ultrafast spectroscopic results, taken at 840 nm at which the cationic state absorption of the PID or PPB polymer in blended films dominates, confirmed this hypothesis. Although the rising time of the PID1 cation signal is still nearly 1 ps, the intramolecular charge separation (CS) dynamics in PID1 are slower than those of PTB7. The charge recombination (CR) of the cationic state, however, is relatively fast for the PID1 polymer. The CR traces of the PID1 polymer were fit to a tri-exponential decay of 2 ps, 60 ps, and > 2 ns. At 3 ns, the cationic signal of only <10% remains, which is much smaller than those in PTB7 (Figure 4). The increased recombination rate is attributed to the increased binding energy of the bound charge transfer state within the polymer, which enhance the recombination probability. These results seem to indicate that the TID unit is too strong in electron-withdrawing ability to be useful in heteropolymers used as donor materials. An optimized polarizability in polymer repeating units is achieved with a $\Delta\mu_{ge}$ around 4 Debye.

Figure 4. The charge separation (rise) and recombination (decay) dynamics monitored at the signals of the cationic state in the PID1 polymer. For comparison, the CS and CR of PTB7 are also shown.



1.5. Further synthetic effort was focused on the roles of quinoidal character and regioregularity in determining the optoelectronic and photovoltaic properties of conjugated copolymers.

An efficient synthetic method for creating ladder-type, oligomeric donor monomers with fused thienobenzothiophene structures. These monomers are copolymerized with fluorinated thieno[3,4-b]thiophene ester to form a series of polymers which were investigated as donor materials in polymer/fullerene solar cells. Photophysical and electrochemical characterizations are used in conjunction with quantum-chemical calculations to identify the interplay of quinoidal and charge transfer character in the optical gaps of conjugated copolymers, providing broadly applicable design rules for tuning the excitation character of conjugated copolymers. X-ray diffraction, mobility measurements, and solar cell device characterization are used to analyze neat films and bulk heterojunctions of these copolymers, demonstrating the importance of the spatial symmetry of the donor and acceptor unit in determining the charge transport characteristics of conjugated copolymers.

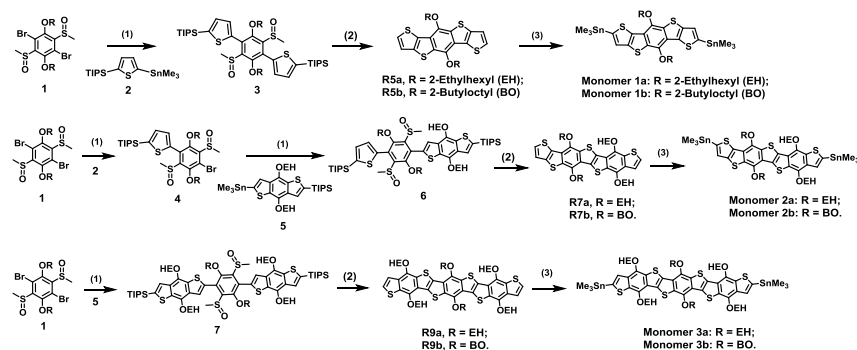
An issue in conjugated copolymers that is not often discussed, but is of vital importance, is the regioregularity of these polymers. While this issue was at the forefront of polymer design in previous generations of materials, notably **P3HT**,^{49,50} this topic has lost interest in recent studies of novel copolymer materials, although some careful studies have examined these effects in donor-acceptor polymers.⁵¹ In recent work, we have computationally examined the effects of conformational and structural dispersion in the optoelectronic properties of conjugated copolymers⁵² and found that copolymers synthesized via non-selective cross coupling reactions such as Stille Coupling, can exhibit dispersion in their optoelectronic properties when the comonomers do not possess the appropriate symmetry operations. The exact role of this energetic dispersion in the charge transport properties of conjugated copolymers is unclear, though it is known that the tail of the density of states primarily determines V_{oc} ,⁵³ and that energetic disorder localizes charge carrier wavefunctions, which should decrease J_{sc} . Consequently, the dispersion of these properties that results from such structural and conformational isomerism is fundamental to interpreting the bulk device properties of these materials, and could benefit from an experimental study of charge transport characteristics in polymers that possess variable amounts of structural dispersion.

Fused thienobenzothiophene polymers have demonstrated much success when employed in conjugated polymer/fullerene based BHJs. The original design idea for the highest performing fused thienobenzothiophene polymer, **PTB7**, was to create a low band gap polymer with enhanced quinoidal structure resulting from the thienothiophene (TT) moiety, which would facilitate charge delocalization and transport by increasing the π -conjugation, as well as improved π - π stacking capability resulting from the introduction of the conjugated fused aromatic ring moiety,

benzodithiophene. Furthermore, these types of conjugated copolymers have demonstrated high versatility for fine-tuning energy levels as well as electronic properties via fluorination⁵⁴ and side-chain substitution effects. Given our experience with these materials, we can use these chemical motifs as models for examining the general properties of conjugated copolymer chemistry and physics. It is well known that materials with extended conjugation in structure were studied extensively as candidates in organic field effect transistor when they showed appreciable charge carrier mobility.⁵⁵⁻⁵⁷ Previous work on small oligomers has examined the effects of the thienothiophene quinoidal character on optoelectronic functionality in these materials.⁵⁸ However, how the thienothiophene quinoidal character propagates in a periodically repeating polymer system as a function of comonomer size and chemical identity represents a fundamental gap in the knowledge base of these systems. Additionally, these chemical motifs present an excellent opportunity for the examination of the previously mentioned dependencies on regioregularity by simply altering the symmetry of the donor comonomer. By perturbing the original **PTB7** chemical structure, we are positioned to answer a variety of important questions in the physics and chemistry of conjugated copolymers.

Previous work has shown that a polymer made from five-ring heteroacene donor units exhibits a similar PCE as **PTB7** in a simple solar cell device.⁵⁹ To investigate the effect of the electron delocalization, a generic method was developed to synthesize oligo-heteroacenes with varied number of fused rings (Scheme 1). The key building block is the compound **1**, 1,4-dibromo-2,5-dialkoxy-3,6-bis(methylsulfinyl)benzene (SI). Pd-mediated coupling reaction between compound **1** and compound **2** in 1:2 ratio yielded precursor **3**, which was cyclized by a ring closing reaction to form **R5**. Lithiation of **R5** followed by stannylation generates monomer **1**, which has five fused rings. Similar coupling reaction between compounds **1** and **2** in 1:1 ratio yielded compound **4** that can be further coupled with compound **5** to yield precursor **6**. Identical cyclization and stannylation reactions lead to monomer **2**. When compounds **1** was coupled with 2 equivalent of compound **5**, the precursor **7** was formed, which can be cyclized to fused nine rings (**R9**) and then be stannylated to form monomer **3**.

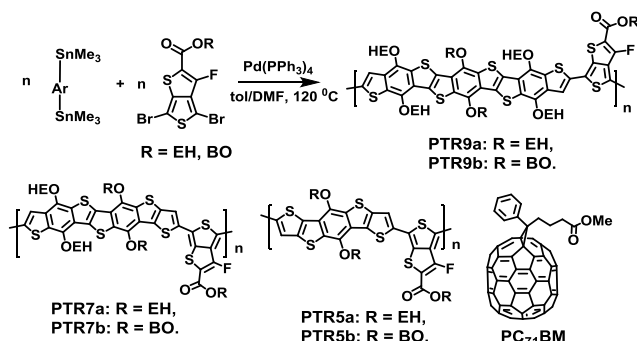
Scheme 2: Synthesis of monomers



(1) Pd(PPh₃)₄, tol or toluene/DMF. (2) TFA/P₂O₅, r.t.; pyridine, reflux; TBAF, r.t. (3) ⁿBuLi, -78 °C to r.t.; Me₃SnCl, -78 °C to r.t.

Among these conversions, the key step is the ring-closing reaction, which is an intramolecular electrophilic substitution by using trifluoroacetic acid (TFA) and P₂O₅ as the reagent, followed by elimination reaction in pyridine. The triisopropylsilyl (TIPS) group played a vital role, since it not only enriched the electron density of the aromatic system, favoring the electrophilic addition, but also prevented the active alpha position of thiophene unit from intermolecular side reactions. Interestingly, the TIPS group attaching to the BDT unit had been mostly removed during ring-closing step, while that on the thiophene unit remained intact, until TBAF was added as observed in the synthesis of **R7**.

Scheme 3 Synthesis of polymers and the structure of PC71BM



The resulting monomers were polymerized with F-substituted dibromo-thienothiophene ester monomer via the Stille polycondensation (Scheme 3). GPC measurements showed sizable molecular weights for these polymers (Table 3). NMR spectra and elemental analysis support the structure as proposed. It was found that **PTR5a** polymer, with 2-ethylhexyloxy (O-EH) side chains was barely soluble in common organic solvents like THF, chloroform and chlorobenzene, and was not further studied. When the side chains were changed to bulkier 2-butyloctyloxy (O-BO) groups, the resulting polymer **PTR5b** exhibited good solubility. Both **PTR7** and **PTR9** show good solubility in organic solvents with both the EH and BO side chains, simply because **R7** (4 side chains/7 rings) and **R9** (6 side chains/9 rings) bear more side chains than the **R5** (2 side chains/5 rings).^{60,61} The TGA studies indicated that the polymers are stable up to around 310 °C at which weight losses of 5% were observed (SI).

Table 3: Molecular weight and UV-vis absorption properties of polymers

Polymers	Mn (kg/mol)	PDI	λ_{peak} (nm)	λ_{onset} (nm)	E_g^{opt} (eV)
PTR5b	35.6	2.15	659	747	1.66
PTR7a	12.6	1.57	595,627	703	1.77
PTR7b	12.3	1.54	586,624	696	1.78
PTR9a	11.0	2.62	580,620	675	1.84
PTR9b	14.7	2.82	580,625	678	1.83

2. Optical and electrochemical properties

The optical absorption spectra of **PTR5**, **PTR7**, and **PTR9** were recorded in both chlorobenzene solution and the neat film, the results of which are similar, as in the case of **PTB7**, which is suggestive of solution-phase aggregation. Those for the neat film are summarized in Table 3. By looking at the red edge of the neat film absorption spectra for **PTR5**, **PTR7**, and **PTR9** (Figure 5a), an apparent blue-shift is observed in the optical absorption as the length of the donor unit is increased from **PTR5** to **PTR9**. The electronic band gaps of these polymers were measured with cyclic voltammetry (CV), using thin films coated on a glass carbon electrode with a scan rate of 50 mV/s and electrolyte Bu₄NPF₆ in CH₃CN solution (0.10 M). The measured electronic band gaps (Figure 5b) demonstrated a similar overall blue shift in going from **PTR5** to **PTR9**. However, this trend is in contrast with the absorption spectra of donor monomers, which showed a red-shift from **R5** to **R9** (Figure 5c).

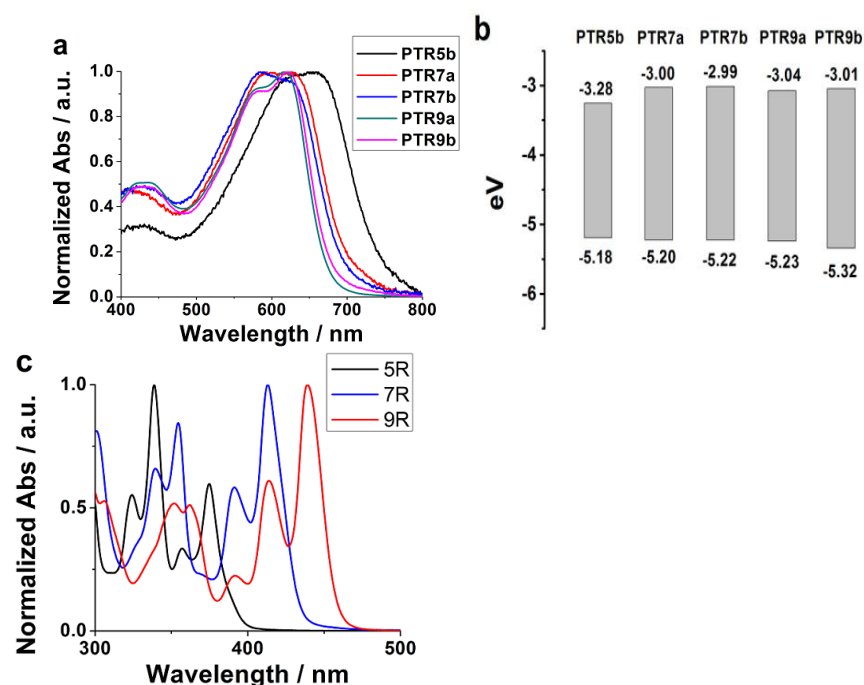


Figure 5 (a) UV-vis absorption spectra of polymers in films gained from spin-coating of their chlorobenzene solution to clean glass. (b) Energy level diagram of polymers. (c) UV-vis absorption spectra of donor monomers in dilute chloroform solution.

The observed shift in the optical gap of polymers and donor monomers seems to be counterintuitive that increasing the size and rigidity of the pi-electron system does not reduce the optical gap of conjugated polymers. However, it is important to pay close attention to the nature of the molecular units along the backbone, as many potential mechanisms for lowering the optical gap of conjugated polymers exist.⁶² All polymers studied here consist of copolymers of the highly quinoidal thienothiophene unit^{63,64} and the highly aromatic fused benzodithiophene donor units. As the number of fused benzodithiophene units of the donor grows, the energy penalty becomes too large to be overcome by the quinoidal character of the thienothiophene unit. As a result, the longer donor moieties prefer fused aromatic rings to the quinoidal form, thus preventing the band gap from further narrowing. In the extreme limit of infinite donor length, the optical absorption should reach the limit of the donor monomer unit. Consequently, by increasing the size of the fused benzodithiophene donor units in an attempt to enhance pi-stacking and decrease the optical gap, it appears that we have fundamentally altered the nature of the optical excitation by changing the quinoidal/aromatic character of the backbone.

3. Computational work

Ground and excited-state density functional theory (DFT) calculations were performed to support the above hypothesis. An oligomer of each repeat unit was chosen (SI), and a ground-state geometry optimization was performed at the EDF1/6-31G* level of theory. In these calculations, all alkoxy groups were simplified to methoxy groups. These ground-state oligomer structures were then used as input to ground-state DFT and excited-state time-dependent DFT (TDDFT) calculations at the OT-BNL/6-31G* level of theory.⁶⁵ These results are summarized in Table 4. Excitations on ground-state vacuum structures should not match up quantitatively with the absorption edge, due to polarization and flattening effects in the film.⁶⁶ However, the OT-BNL method has been used to accurately determine the excitation energies in studies on similar materials.⁶⁷ While the absolute values of our computed optical gaps are shifted from experimental results, the relative blue-shift of each structure was accurately predicted, and compares favorably with the experimental spectrum, confirming that the blue-shift is indeed due to the changes in chemical structure, and not solely the result of differential polymer aggregation in the film.

Table 4 Calculated energy levels and gaps for polymers

Polymers	HOMO (eV)	LUMO (eV)	E _g ^{opt} (eV)
PTB7	-5.09	-1.06	2.14
PTR5	-5.03	-1.01	2.12
PTR7	-5.14	-0.94	2.25
PTR9	-5.12	-0.82	2.32

In order to quantify this further, DFT calculations (OT-BNL/6-311G**) were performed to determine the energy level alignment of the donor and acceptor units used in these copolymers. It was determined that indeed the band gaps of the donor monomers become narrow as they become longer, which is consistent with the optical absorption spectra of monomers as present in Figure 1c. However, when comparing with the acceptor monomer thienothiophene, it is clear that as the conjugation of the donor unit increases above the 5-ring (**PTR5**), the lowest unoccupied molecular orbital (LUMO) level of the donor drops below the LUMO of thienothiophene (Figure 6). Consequently, the conjugation in the resulting polymers (**PTR7** and **PTR9**) between the donor monomer and acceptor monomer becomes less efficient, decreasing the charge transfer nature of the excitation, resulting in a less quinoidal structure, and the blue shift of the polymers relative to **PTB7**.

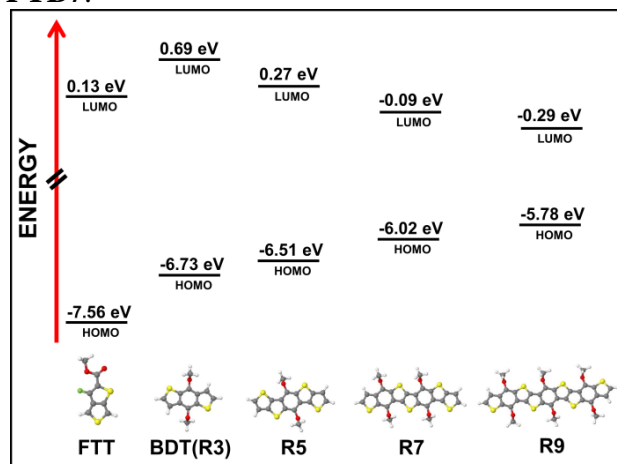


Figure 6. Calculated energy levels of monomers. Geometry was optimized at EDF1/6-31G* and energy levels were calculated at OT-BNL/6-31G*.

4. X-Ray Diffraction

The blend films of polymers show uniform and fine features according to TEM studies (SI). The GIWAXS studies (Figure 7) indicate that neat and blend **PTR5**, **PTR7**, and **PTR9** films all exhibit scattering between $q = 0.32\text{--}0.38 \text{ \AA}^{-1}$ which relates to d-spacings of $20 \text{ \AA} - 17 \text{ \AA}$ corresponding to **PTR** lamellar stacked regions and is determined by the type and orientation of the alkyl side chains. This scattering can be divided into two distinct regions: an arc growing from $q_{xy} = 0.32\text{--}0.36 \text{ \AA}^{-1}$ and a more localized peak at $q_z = 0.33\text{--}0.38 \text{ \AA}^{-1}$. In general, features along the horizontal, q_{xy} , axis describe the in-plane structure while features along the vertical, q_z , axis roughly describe the out-of-plane structure,⁶⁸ so the presence of lamellar stacking in both the horizontal and vertical suggest that two different orientations and crystal packing are present in the **PTR** thin films. The out-of-plane lamellar stacking indicates an edge-on orientation of the polymer and a smaller d-spacing, while the in-plane lamellar stacking indicates a face-on orientation of the polymer and a larger d-spacing. For neat films of **PTR9a** and **PTR9b**, in addition to the lamella scattering peaks, an out-of-plane scattering peak appears at $q = 0.54 \text{ \AA}^{-1}$ (1.1 nm) and $q = 0.49 \text{ \AA}^{-1}$ (1.2 nm),

respectively, consistent with the change to larger side chains in **PTR9b**. We attribute this peak to different polymorphs of the edge-on lamellar stacking in **PTR9** which can be attributed to different side chain orientations. While it is possible these polymorphs exist in the **PTR5** and **PTR7** polymers, we suggest that they are more highly ordered in the **PTR9** polymers due to the increased backbone rigidity. These polymers also exhibited $q = 1.61\sim 1.65 \text{ \AA}^{-1}$ corresponding to a π - π d-spacing around 3.8-3.9 \AA . Note that the π - π stacking is only present in the vertical direction, so while edge-on lamellar stacked domains are present, the edge-on domains do not create 3-dimensional π - π stacked crystals. In the neat films, a broad isotropic scattering peak at $q = 1.0\text{-}1.3 \text{ \AA}^{-1}$ is attributed to amorphous scattering, while in blend films, the isotropic ring at $q = 1.4 \text{ \AA}^{-1}$ is due to the PCBM structure

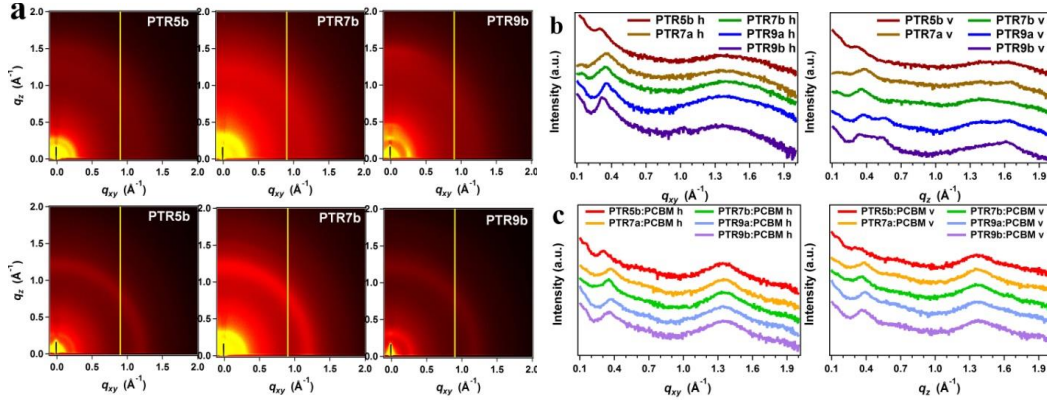


Figure 7: (a) 2D GIWAX images for neat polymer films (upper) and polymer/PCBM blend films (lower). (b) Linecut of GIWAX images of neat polymer films on horizontal (left) and vertical (right) direction. (c) Linecut of GIWAX images of polymer/PCBM blend films on horizontal (left) and vertical (right) direction.

Scherrer analysis is used to measure trends in the crystalline domain size of the lamellar stacked domains and the π - π stacked domains. Neat **PTR5** and **PTR7** films exhibit small face-on lamellar crystalline domains of 4-6 nm while both **PTR9** films contain domains of 8-10 nm. The π - π stacked domain size follows a similar trend (Table 5) and we attribute the increased domain sizes in **PTR9** to its increased backbone rigidity, leading to more ordered polymer domains. In blend films, the reverse trend is observed and the face-on lamellar domain size is smaller for **PTR9** (~4 nm) than for **PTR7** (5.6-7 nm) and **PTR5** (~8 nm). The π - π stacked domain size cannot be confidently calculated due to its low intensity and overlap with the PCBM peak. After forming blend film with PCBM, all of polymer domains are homogenized to 2-5 nm, indicating that the polymer phase separation is ideal for exciton migration.

Table 5: Lamellar and π - π d-spacing and domain size for both neat and blend films of polymers

Polymers	Lamellar (\AA)	Domain size (\AA)		π - π (\AA)	Domain size (\AA)	
	neat	neat	blend	neat	neat	blend
PTR5b	19.91	65	84	3.83	18	23
PTR7a	17.60	42	56	3.80	41	33
PTR7b	18.14	49	72	3.83	12	32
PTR9a	17.78	102	40	3.84	49	50
PTR9b	19.13	83	45	3.88	46	31

5. Hole mobility

The hole mobilities of polymers were measured according to the Space Charge Limited Current (SCLC) model, and the results were plotted in Figure 4, from which hole mobilities of 5.02×10^{-4} , 2.50×10^{-6} , 5.56×10^{-6} , 1.32×10^{-4} , 1.11×10^{-4} $\text{cm}^2/\text{V}\cdot\text{s}$ were observed for **PTR5b**, **PTR7a**, **PTR7b**, **PTR9a** and **PTR9b**, respectively (Figure 8). **PTR5b** exhibits similar mobility with **PTB7**. A significant decrease occurred when the polymer's donor moiety changed to larger conjugated system. The hole mobility of **PTR9** dropped to about 1/5~1/4 of that of **PTR5**, and that of **PTR7** was even 2 orders of magnitude smaller than that of **PTR5**. While one would expect increased conjugation and rigidity of the donor moiety to favor for charge carrier transport, the decrease in mobilities appears to correlate with the side-chain to fused ring ratio of **PTR5** through **PTR9**. As the fused ring system is made longer, the ratio of side-chains to fused rings grows. More alkyl side-chains would disrupt π - π stacking, and decrease charge transport by lowering intermolecular charge transfer couplings. While this explanation is capable of explaining the general trend of decreasing polymer mobility as the length of the donor unit grows, it is not capable of explaining the drastic decrease in the mobility observed for **PTR7**. Upon examination, it becomes clear that **PTR7** differs from **PTR5** and **PTR9** in that it exhibits only C1 symmetry. As shown in recent work,⁵² whether or not the donor and acceptor units possess appropriate symmetry in a Stille condensation process determines the width of the distribution of structural and conformational isomers. While most copolymers in the literature consist of symmetric donor and a symmetric or asymmetric acceptor, **PTR7** consists of asymmetric donor and an asymmetric acceptor. The backbone of the copolymer then will exhibit 2^n (where n is the length of the copolymer) more potential regioisomers than the corresponding **PTR5** and **PTR9**. Given the similarity of the XRD data regarding these materials, it is likely that the increase in disorder of the backbone's electronic system resulting from this regioirregularity is leading to localization of the wave function, and decreasing the mobility of charge carriers, in agreement with the observed mobilities. With the same backbone, a slight decrease of hole mobility was observed after introducing bulky side chains if we compare that of **PTR9a** and **PTR9b** due to the increase in the steric hindrance for intermolecular packing. GIWAXS studies (Figure 7) indeed showed that the lamellar d-spacing for **PTR9b** was larger than that of **PTR9a**.

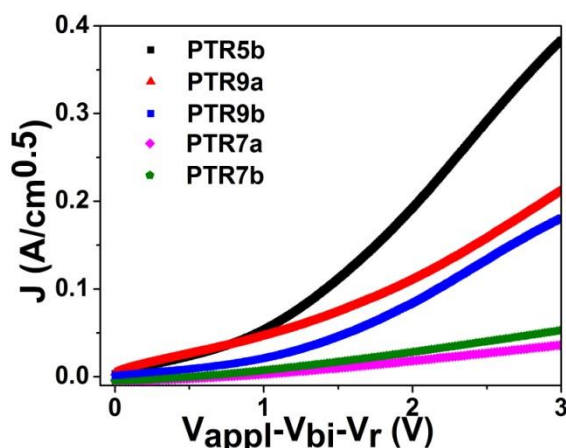


Figure 8: $J^{0.5}$ vs V plots for the polymer films.

6. Photovoltaic properties

Photovoltaic properties of polymers were investigated in a device structure of ITO/PEDOTS:PSS/polymer:PC₇₁BM (1:1.5, wt ratio)/Ca/Al. The active layer was prepared by spin-coating polymer solution in mixed solvent of CB/DIO (97/3, v/v). Figure 9a showed the J-V response of polymer solar cells under AM 1.5 condition at 100 mW/cm^2 . Representative characteristics were summarized in Table 4. The cell made from **PTR5b** gave a PCE of about 5% with moderate J_{sc} ($12.2 \text{ mA}/\text{cm}^2$) and V_{oc} (0.65 V). The **PTR9** polymers exhibited slightly higher V_{oc} (0.71 V), which might be due to their deeper HOMO, but showed inferior efficiency because

of the lower J_{sc} and fill factor. The corresponding EQE spectrum in Figure 9b indicate that **PTR5b** had a higher EQE value with over 40% in the 400 nm to 700 nm range than that of **PTR9**, which was consistent with their J-V performance. However, the performance of polymer solar cells can be improved by modifying the side chain attached to the backbone. For example, replacement of the dialkoxy benzodithiophene (2-ethylhexyloxy, O-EH) in the **PTB7** with alkyl analogue (CH_2EH), generated a new polymer **PTB10** (Scheme 3), which showed slightly higher V_{oc} , but slightly lower J_{sc} , and overall, almost the same PCE (7.3%) as **PTB7** (7.4%). But for **PTDBD**, it triumphed over **PTR5b** in all aspects and the PCE increased from about 5% to 7.6%. The same trend is observed for **PTR9c**, which had an efficiency of 5.5%, doubled that of the other two **PTR9** polymers. It is not surprising that even though the structure of **PTR7** polymers is very similar to those of **PTR5** or **PTR9**, their solar cell performances are extremely low with nearly 0% efficiency. As discussed above, the asymmetric nature of donor monomer leads to the regioirregularity of **PTR7** polymer, which should account for their low charge carrier mobilities, and thus poor performance in OPV cells is predicted

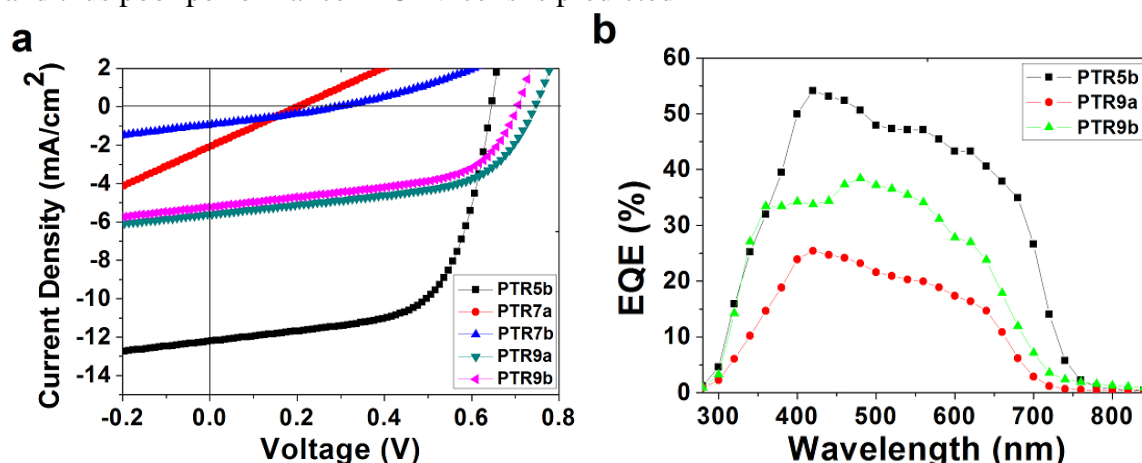


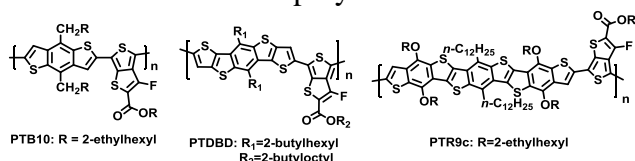
Figure 9: (a) J-V characteristics of polymer solar cells under AM 1.5 condition (100 mW/cm^2), (b) EQE of polymer/PC₇₁BM device. No result was obtained for **PTR7** polymers because of the low current of devices.

Table 6. J-V characteristics of polymer solar cells

Polymers	J_{sc} (mA/cm^2)	V_{oc} (V)	FF (%)	PCE (%)
PTB7^a	14.5	0.74	69.0	7.4
PTR5b	12.2	0.65	63.0	5.0
PTR7a	0.28	0.20	25.0	0.014
PTR7b	0.96	0.30	28.8	0.083
PTR9a	7.23	0.71	54.6	2.8
PTR9b	5.22	0.71	54.0	2.0
PTB10	13.6	0.77	69.1	7.3
PTDBD^b	13.0	0.89	65.3	7.6
PTR9c	11.2	0.72	67.9	5.5

a: ref [⁴⁵]; b: ref [⁵⁹]

Scheme 5. Structures of polymers after modification



2. Enhance light harvest via cooperative plasmonic effect of dual precious metal nanoparticles:

The major achievement in the past year in Yu's lab is the demonstration of a cooperative plasmonic effect on improving the performance of polymer bulk heterojunction (BHJ) solar cells. When mixed Ag and Au nanoparticles are incorporated into the anode buffer layer, dual nanoparticles show superior behavior on enhancing light absorption in comparison with single nanoparticles, which led to the realization of a polymer solar cell with a power conversion efficiency of 8.67%, accounting for a 20% enhancement from that without nanoparticles. The cooperative plasmonic effect aroused from dual resonance enhancement of two different NPs. The idea was further unraveled by comparing Au nanorods with mixed nanoparticles for solar cell application. A similar enhancement of nanorods mixture with that of mixed Au and Ag nanoparticles was observed because the plasmonic absorption spectra of gold nanorods also exhibit dual peaks in the visible region. Detailed studies shed light into the influence of plasmonic nanostructures on exciton generation, dissociation and charge recombination and transport inside thin film devices. We believe that the results of our study offer an effective approach to enhance the efficiency of organic BHJ solar cells.

3. Facilitate charge separation via Ternary Blend Polymer Solar Cells

Ternary blend PSCs with two donor materials and one fullerene acceptor are emerging as an attractive strategy to overcome the PCE bottleneck for binary devices while maintaining the simplicity of processing condition as for single active layer compared to tandem cells. Recently, dye sensitizers²⁰⁻²², polymer sensitizers²³⁻²⁶, small molecular sensitizers²⁷ and quantum dot sensitizers^{28,29} have been utilized as the additional donor material in ternary blend solar cells to extend the absorption of solar spectrum. However, most of these systems are based on P3HT as the dominating donor polymer and still exhibit poor performance compared with the state of the art binary counterparts. Not to mention the even reduced device performance in some cases with the third component acting as recombination centers or defects within the active layer^{30,31}. In addition, although it has been reported that adding PCPDTBT into P3HT:PCBM blend would lead to decreased crystallinity of PCBM³² or smooth surface morphology³³, no experimental evidence of positive changes in bulk morphology inside the ternary blend system after the incorporation of the third component has been reported.

In this work, we demonstrate for the first time, efficient ternary blend BHJ solar cells with PCEs larger than 8% by incorporating poly-3-oxothieno[3,4-*d*]isothiazole 1,1-dioxide/benzodithiophene (PID2) as the additional donor material into polythieno[3,4-*b*]thiophene/benzodithiophene (PTB7) : [6,6]-Phenyl C71 butyric acid methyl ester (PC₇₁BM) host binary blend. Unlike common ternary blend systems, where the enhancement in PCE mainly comes from extended light harvesting in solar spectrum by the third component^{24,25,28,34}, we show for the first time that a high efficient ternary blend solar cell could also be developed with the third component not only improving photon absorption range but more importantly, facilitating charge separation and transport while suppressing charge recombination through a combination of cascade energy levels and optimized device morphology.

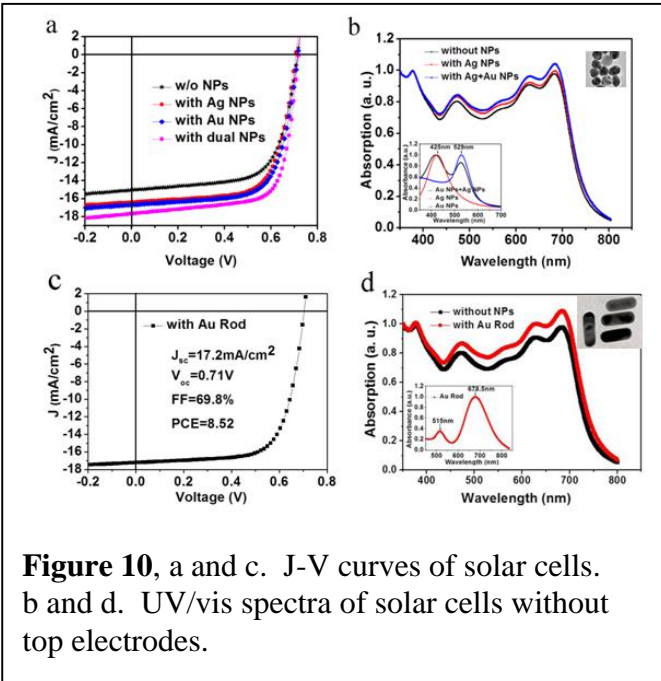


Figure 10, a and c. J-V curves of solar cells. b and d. UV/vis spectra of solar cells without top electrodes.

Chemical structures of PTB7, PID2 and PC₇₁BM are shown in Figure 11a. The synthesis and characterization of PID2 will be published elsewhere. The highest occupied molecular orbital (HOMO) energy level and lowest unoccupied molecular orbital (LUMO) of PID2 are -5.52 eV and -3.50 eV, determined from cyclic voltammetry curve. PID2 used in this work has a molecular weight at 32 kg/mol. The cascade energy levels of the three components are shown in Figure 1b. Solar cells used in this work have a simple structure that we always used to evaluate the material's properties: ITO/poly(3,4-ethylenedioxythiophene):poly(styrenesulfonate) (PEDOT:PSS)/PTB7:PID2:PC₇₁BM /Ca/Al (Figure 11c).

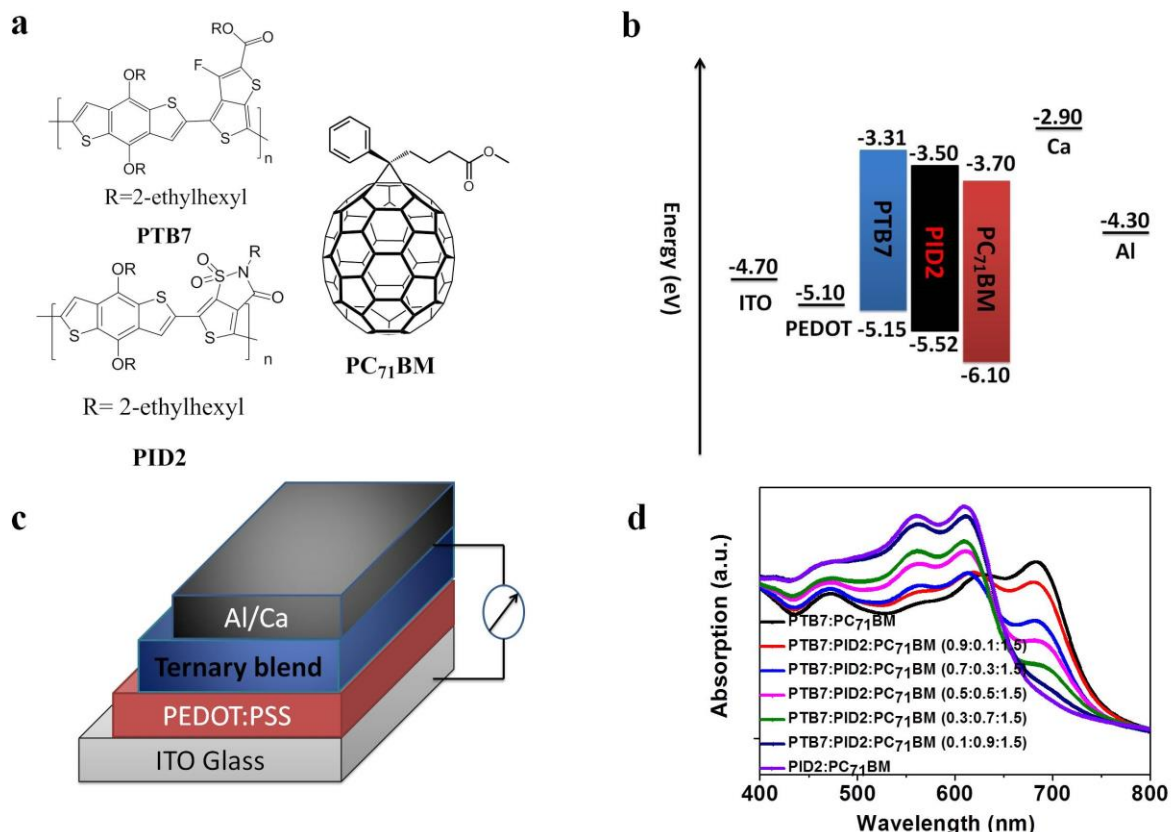


Figure 11: | Material properties and device structure. a, Chemical structures of PTB7, PID2, PC₇₁BM. **b**, energy levels of electrodes and active layer materials used in ternary blend solar cells. **c**, device structure of solar cells used in this work. **d**, UV-vis absorption spectra of ternary PTB7:PID2:PC₇₁BM blend with different ratios of PTB7:PID2.

We first measured the UV-vis absorption of the ternary blends with different PID2 contents to study the changes in absorption upon incorporation of the third component. Figure 11d indicates that increasing the content of PID2 in PTB7:PC₇₁BM host blend gradually enhanced the absorption from 450 nm to 650 nm while simultaneously decreased the absorption from 650 nm to 750 nm, consistent with the fact that the PID2 showed maximum absorption at 610 nm and the absorption maximum of PTB7 was at 683 nm.

The overall polymer to PC₇₁BM ratio was kept at 1:1.5 in this work. Figure 12a shows the corresponding current density versus voltage (*J-V*) characteristics of ternary blend solar cells with different PID2 contents under AM 1.5 G illumination at 100 mW/cm². Table 7 summarizes the photovoltaic parameters for those devices. The PTB7:PC₇₁BM used as a reference device gave a PCE of 7.25% with an open circuit voltage (*V_{oc}*) at 0.72 V, a short circuit current density (*J_{sc}*) at 15.0 mA/cm² and a fill factor (*FF*) at 67.1%. It is clear from Figure 12a that *J_{sc}* was enhanced significantly after the incorporation of a small amount of PID2 (10% or 30%) into the host blend

and decreased later when PID2 became the dominating donor polymer in the system. The decreased performance at high PID2 content should be ascribed to the poor performance of PID2, which only gave a PCE of 2.01% when mixed with PC₇₁BM. Meanwhile, V_{oc} of the ternary blend solar cells was pinned to the smaller V_{oc} of PTB7:PC₇₁BM host blend at all PID2 contents. This is attributed to the fact that V_{oc} is mainly determined by the smallest difference between HOMO energy levels of donor materials and LUMO energy level of PC₇₁BM²⁴. The HOMO energy levels of PTB7 and PID2 are -5.15 eV and -5.52 eV, respectively (Figure 11b). In particular, with a 9:1 ratio between PTB7 and PID2, we achieved a V_{oc} at 0.72 V, a J_{sc} at 16.8 mA/cm² and a FF at 68.7%, resulted in a very promising PCE of 8.22%. An average PCE of 8.01% was attained over 10 identical devices under this condition with a mean V_{oc} at 0.71 ± 0.01 V, a J_{sc} at 16.7 ± 0.36 mA/cm² and a FF at $67.9 \pm 0.70\%$. To the best of our knowledge, this is the highest PCE reported for ternary blend PSCs so far. When the content of PID2 was increased to 30%, J_{sc} of the device was improved to 16.3 mA/cm², yielding a PCE of 7.88%. Solar cell with 50% of PID2 showed comparable PCE compared to the reference device. Further increasing the content of PID2 beyond 50% resulted in decreased solar cell performance due to inferior J_{sc} and FF compared to PTB7:PC₇₁BM reference device. Since incorporation of 10% and 30% PID2 showed better solar cell performance than the reference device, the two conditions are used in the following measurements to unravel the mechanism for the increase in J_{sc} and FF in our ternary blend system.

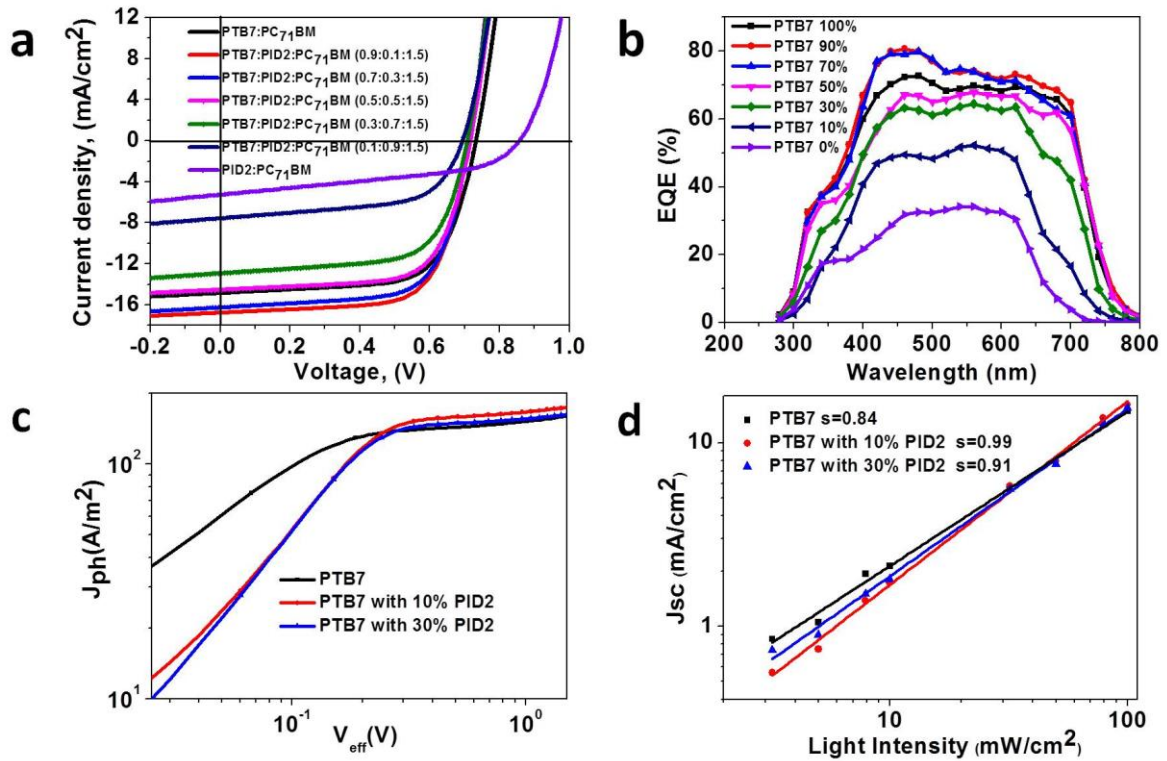


Figure 12 | Photovoltaic performance. **a**, Current-voltage characteristics of ternary solar cells with different polymer mixture ratios. **b**, EQE curves of ternary PTB7:PID2:PC₇₁BM blend different PID2 contents. **c**, Photocurrent density (J_{ph}) versus effective voltage (V_{eff}) characteristics. **d**, Dependence of J_{sc} on light intensity of ternary system with different polymer ratios.

Table 7 | Summary of solar cell parameters of ternary PTB7:PID2:PC₇₁BM blend with different ratios of PTB7:PID2.

<i>PTB7:PID2:PC₇₁BM</i>	<i>J_{sc} (mA/cm²)</i>	<i>V_{oc} (V)</i>	<i>FF (%)</i>	<i>PCE (%)</i>
1:0:1.5	15.0	0.72	67.1	7.25
0.9:0.1:1.5	16.8	0.72	68.7	8.22
0.7:0.3:1.5	16.3	0.71	68.0	7.88
0.5:0.5:1.5	14.5	0.72	68.3	7.10
0.3:0.7:1.5	12.9	0.71	66.1	6.04
0.1:0.9:1.5	7.56	0.70	59.5	3.12
0:1:1.5	5.27	0.86	44.4	2.01

To study changes in J_{sc} , external quantum efficiency (EQE) of the ternary blend devices was measured and the results are illustrated in Figure 12b. Ternary systems with up to 30% PID2 incorporation showed similar thicknesses (around 130 nm) to PTB7:PC₇₁BM binary device. Thus direct comparison between the EQE results is meaningful. Unlike the trend we observed in the UV-vis absorption spectra, incorporation of 10% PID2 into PTB7:PC₇₁BM blend led to increased EQE values over the whole wavelength region. The EQE values were enhanced most in the region between 400 nm to 550 nm where PC₇₁BM exhibits high absorption. Since incorporation of 10% PID2 only led to better absorption from 500 nm to 620 nm in Figure 1d, the increase in EQE between 400 nm to 550 nm at low PID2 content should not result from additional absorption enhancement of PID2. Instead, this result indicated that the small amount of PID2 played the role of hole relay between PC₇₁BM and PTB7 via its HOMO orbital. The energy diagram clearly showed that the HOMO energy level difference between PC₇₁BM and PTB7 is about 0.95 eV, too large for an effective hole transfer. The HOMO energy level of PID2 is almost positioned in the middle of the PTB7 and PC₇₁BM, forming the cascade HOMO energy levels for more effective extraction of holes from PC₇₁BM (Figure 11b)³⁵. To prove this, we measured film photoluminescence (PL) of PID2, PTB7 and PTB7:PID2 (both 0.9:0.1 and 0.7:0.3 ratios) excited at 610 nm (maximum absorption for PID2). The results are shown in Figure S7a. Generally, if energy transfer between PID2 and PTB7 exists, one would expect increased PL emission for PTB7 with decreased PL emission for PID2 assuming that the quantum yields of the two polymers are similar. On the other hand, if photoinduced electron transfer from HOMO energy level of PTB7 to HOMO energy level of excited PID2 exists (hole transfer from PID2 to PTB7) (Figure S7b), emission of PID2 would be quenched without increase of PTB7 PL signal. PID2 showed a strong emission with a maximum at 680nm while PTB7 exhibited a weak PL emission signal with a peak at 760 nm. PL of PID2 was completely quenched while PL of PTB7 remained almost the same in PTB7:PID2 blends (both 0.9:0.1 and 0.7:0.3). The results confirmed that photoinduced electron transfer from PTB7 to PID2 (hole transfer from PID2 to PTB7) existed other than energy transfer between PID2 and PTB7. Since hole transfer from PC₇₁BM to PID2 was already demonstrated by 2.01% device performance for PID2:PC₇₁BM, we could conclude that holes could transfer from PC₇₁BM to PID2 and finally to PTB7. In addition, we fabricated a solar cell using PTB7 and PID2 at 1 to 1 ratio only and achieved a PCE at 0.051%, with a V_{oc} at 0.65 V, a J_{sc} at

0.192 mA/cm² and a *FF* at 40.8%. Although the PCE was poor due to the fact that PID2 was designed as a donor material instead of an acceptor, it again proved that charge separation and transport between PTB7 and PID2 happened at their interfaces. This point is further reinforced by an improved EQE values from 400 nm to 650 nm while remained similar values from 650 nm to 750 nm when PIB2 content was increased to 30%. The integrated J_{sc} values from EQE spectrum for PTB7:PC₇₁BM (1.0:1.5), PTB7:PID2:PC₇₁BM (0.9:0.1:1.5), PTB7:PID2:PC₇₁BM (0.7:0.3:1.5) devices were 15.1 mA/cm², 16.3 mA/cm², 15.8 mA/cm², respectively. This is within 3% difference from measured J_{sc} values, indicating that *J-V* measurements in this work are reliable. In addition, since devices with low PID2 content (10% and 30%) showed higher or comparable EQE values from 650 nm to 750 nm compared to PTB7:PC₇₁BM while higher PID2 content (>30%) led to lower EQE values from 400 nm to 650 nm, we can again conclude that changes in light absorption is not the only cause for J_{sc} changes in our ternary blend system, the cascade energy levels is also important to PCE changes.

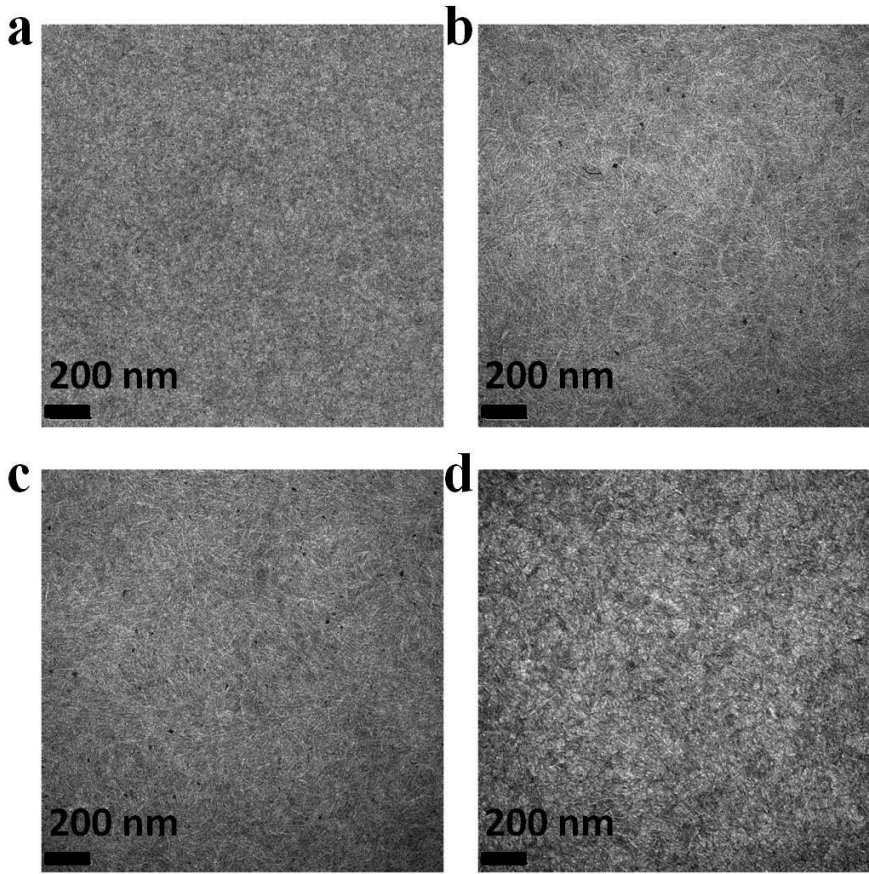


Figure 13 | TEM characterization. TEM images of **a**, PTB7:PC₇₁BM (1:1.5). **b**, PTB7:PID2:PC₇₁BM (0.9:0.1:1.5). **c**, PTB7:PID2:PC₇₁BM (0.7:0.3:1.5). **d**, PID2:PC₇₁BM (1:1.5).

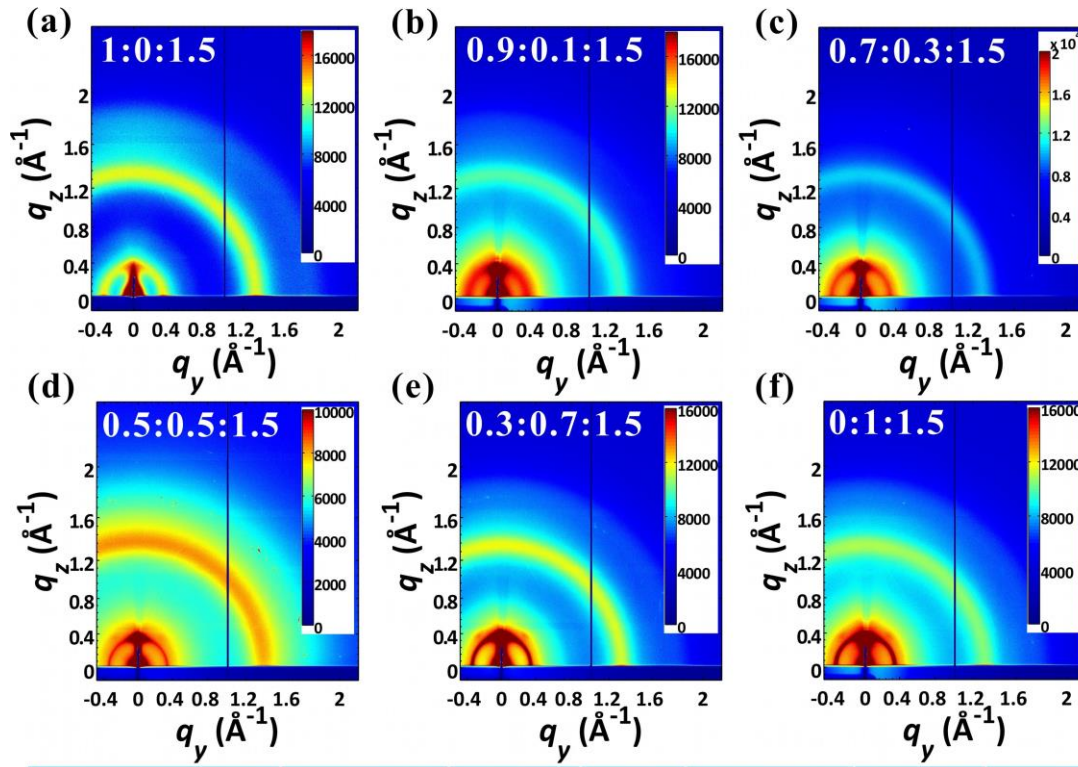
To gain more insight into light absorption and exciton dissociation process, we determined the saturation current density (J_{sat}) and charge dissociation probabilities $P(E,T)$ of PTB7:PC₇₁BM (1:1.5), PTB7:PID2:PC₇₁BM (0.9:0.1:1.5), PTB7:PID2:PC₇₁BM (0.7:0.3:1.5) devices. Figure 12c reveals photocurrent density (J_{ph}) versus effective voltage (V_{eff}) curves for solar cells used in this work. Here J_{ph} is defined as $J_{ph} = J_L - J_D$, where J_L and J_D are the photocurrent densities under illumination and in the dark, respectively. V_{eff} is defined as $V_{eff} = V_0 - V_a$, where V_0 is the voltage where J_{ph} equals zero and V_a is the applied bias voltage³⁶. If we assume that all the photogenerated

excitons are dissociated into free charge carriers and collected by electrodes at a high V_{eff} (i.e. $V_{eff} = 2$ V), saturation current density (J_{sat}) will only be limited by total amount of absorbed incident photons. The J_{sat} values for the three devices were 169 A m^{-2} (0% PID2 content), 180 A m^{-2} (10% PID2 content) and 169 A m^{-2} (30% PID2 content), respectively. Further increasing the content of PID2 showed dramatic decrease in J_{sat} values (Figure S8). The larger J_{sat} value of device with 10% PID2 content would suggest enlarged overall exciton generation while the unchanged J_{sat} value of device with 30% PID2 content suggested the same overall exciton generation compared to the control device^{13,35}. It should be pointed out that even though J_{sat} increased at 10% PID2 content by 6.5%, the increased J_{sat} was still not enough to account for the overall enhancement in J_{sc} (12%). Since both 10% and 30% contents of PID2 showed much larger J_{sc} values than the control device, the J_{ph} results further confirmed the assertion that both absorption change and energy cascade contributed to the change in current density in this work. The $P(E, T)$ is determined by normalizing J_{ph} with J_{sat} (J_{ph} / J_{sat})³⁷. The $P(E, T)$ values under J_{sc} condition for the three devices were 88.0%, 90.2%, 91.2%, respectively, while the $P(E, T)$ value for PID2:PC₇₁BM device was only 65.6%. The results showed that incorporation of PIB2 at low contents facilitated charge dissociation in ternary devices.

In addition to light absorption and exciton dissociation, we also measured J_{sc} as a function of illumination intensities for the three devices to monitor the changes in recombination kinetics. Quantitatively, J_{sc} follows a power-law dependence on light intensity ($J_{sc} \propto P_{light}^S$)^{38,39}. In general, linear scaling of photocurrent with P_{light} would suggest weak bimolecular recombination while sublinear scaling of photocurrent with P_{light} indicates partial loss of charge carriers during charge transport process due to bimolecular recombination. As shown in Figure 12d, the exponential factors of PTB7:PC₇₁BM (1:1.5), PTB7:PID2:PC₇₁BM (0.9:0.1:1.5), PTB7:PID2:PC₇₁BM (0.7:0.3:1.5) devices were 0.84, 0.99, 0.91, respectively. Thus, bimolecular recombination was weakest in devices with 10% of PID2. Compared to PTB7:PC₇₁BM, device with 30% of PID2 also showed decreased bimolecular recombination. Changes in bimolecular recombination help to explain the increased J_{sc} and FF in the ternary blend system. This is in good agreement with hole mobility data of these devices, measured with the structure ITO/ PEDOT:PSS/ PTB7:PID2/ Al using space-charge-limited current (SCLC) model⁴⁰. As shown in Figure S9, hole mobility increased from $5.42 \times 10^{-4} \text{ cm}^2 \text{ V}^{-1} \text{ s}^{-1}$ (PTB7) to $7.75 \times 10^{-4} \text{ cm}^2 \text{ V}^{-1} \text{ s}^{-1}$ (PTB7:PID2 /0.9:0.1) and $8.72 \times 10^{-4} \text{ cm}^2 \text{ V}^{-1} \text{ s}^{-1}$ (PTB7:PID2 /0.7:0.3), while hole mobility of PID2 was only $2.71 \times 10^{-4} \text{ cm}^2 \text{ V}^{-1} \text{ s}^{-1}$. The improved charge transport property is the result of the cascade energy levels in the ternary system and improved morphology as discussed below³⁵.

Transmission electron microscopy (TEM) was first used to probe morphology of the ternary blend (Figure 13). Both PTB7:PID2:PC₇₁BM (0.9:0.1:1.5) and PTB7:PID2:PC₇₁BM (0.7:0.3:1.5) films showed fibrous features while no such structure was observed in PTB7:PC₇₁BM or PID2:PC₇₁BM devices. This seems to indicate that the PID2 plays the role of template for the formation of fibrous structure in PTB7. The fine dispersed fibrils were previously found beneficial to exciton separation and charge transport^{41,42}. Tapping mode atomic force microscopy (AFM) height and phase images of the ternary system showed that the root-mean-squared (RMS) roughness of the four devices based on PTB7:PC₇₁BM (1:1.5), PTB7:PID2:PC₇₁BM (0.9:0.1:1.5), PTB7:PID2:PC₇₁BM (0.7:0.3:1.5) and PID2:PC₇₁BM (1:1.5) was 0.87 nm, 1.06 nm, 1.02 nm and 2.31 nm, respectively. Although PID2 showed higher roughness than PTB7 when mixed with PC₇₁BM, blending PID2 into PTB7:PC₇₁BM up to 30% did not cause any significant change of surface roughness of the host blend. X-ray scattering techniques helped to understand changes in molecular packing, structure ordering and domain sizes in our devices. Shown in Figure 4 and 5 are the 2D grazing incidence wide-angle X-ray scattering (GIWAXS) patterns and resonant soft X-ray scattering (RSoXS) profiles of the ternary PTB7:PID2:PC₇₁BM blend films with different PID2 content. In the 2D GIWAXS pattern of PTB7:PC₇₁BM (1:1.5) blend film (Figure 14a), a

broad arc-like scattering arising from the Bragg diffraction of periodic PTB7 layers was observed at $q_y \sim 0.36 \text{ \AA}^{-1}$, suggesting the preferential face-on conformation, whereas the 2D GIWAXS pattern of PID2:PC₇₁BM (1:1.5) blend film (Figure 14f) exhibited a ring-like layering peak at $q_z \sim 0.34 \text{ \AA}^{-1}$ and two off-axis scattering spots located at $(\pm 0.27, 0.38) \text{ \AA}^{-1}$, indicating the formation of PID2 bilayer ordering with a preferential edge-on orientation similar to that observed in PCDTBT⁴³. Since the full width at half maximum (FWHMs) of scattering peak, Δq , correlates to the nanocrystallite size *via* Scherrer equation⁴⁴⁻⁴⁶, the narrower Δq of PID2 layering peak indicated that PID2 could form larger nanocrystallite sizes in the blend film than PTB7. Further RSoXS studies provided access to the spatial dimensions of phase-separated domains^{45,46}. The RSoXS profile of the PTB7:PC₇₁BM blend film showed a diffuse scattering at $q \sim 0.006 \text{ \AA}^{-1}$, while that of the PID2:PC₇₁BM blend film exhibited a well-defined peak centered at a larger q value of $\sim 0.003 \text{ \AA}^{-1}$ (Figure 5). This illustrates that the phase-separated domains in PID2:PC₇₁BM blend film were larger than those in PTB7:PC₇₁BM blend film. However, upon incorporating a small amount of PID2 copolymers into PTB7:PC₇₁BM blend film (PTB7:PID2:PC₇₁BM (0.9:0.1:1.5)), PID2 copolymers showed little influence on the crystalline structures of both conjugated polymers and PC₇₁BM while induced the formation of smaller phase separated domains. These smaller domains would increase the area of interfaces between polymer donors and fullerene acceptors, thus facilitating exciton dissociation and lead to an improved performance. This is in accordance with our exciton dissociation results. Further increasing the amount of PID2 copolymers, PID2:PC₇₁BM blends gradually phase separated out of the PTB7:PC₇₁BM blends and formed individual blend region in the films. Both larger conjugated polymer nanocrystallites and phase-separated domains formed in the ternary blend films and low PID2 mobility resulted in decreased device efficiency at high PID2 content. Taken together, these observations of morphological changes in the ternary blend films support our hypothesis that the incorporation of PID2 at low contents could facilitate charge dissociation and transport. This also helps to explain the tendency of performance change as a function of the PID2 contents in our device.



PTB7:PID2:PC ₇₁ BM	q_r (Å ⁻¹)	Δq_r (Å ⁻¹)	D_L (Å)	q_z (Å ⁻¹)	Δq_z (Å ⁻¹)	D_L (Å)
1:0:1.5	0.363±0.009	0.172	34.4	—	—	—
0.9:0.1:1.5	0.350±0.009	0.175	33.8	—	—	—
0.7:0.3:1.5	0.332±0.009	0.216	27.4	0.329±0.009	0.076	77.7
0.5:0.5:1.5	0.349±0.009	0.140	42.3	0.333±0.009	0.046	128.4
0.3:0.7:1.5	0.344±0.009	0.073	81.2	0.348±0.009	0.043	138.8
0:1:1.5	0.344±0.009	0.033	180.8	0.336±0.009	0.041	145.5

Figure 14 | 2D GIWAX patterns of ternary films on PEDOT:PSS-modified Si substrates. a, PTB7:PC₇₁BM (1:1.5). **b,** PTB7:PID2:PC₇₁BM (0.9:0.1:1.5). **c,** PTB7:PID2:PC₇₁BM (0.7:0.3:1.5). **d,** PTB7:PID2:PC₇₁BM (0.5:0.5:1.5). **e,** PTB7:PID2:PC₇₁BM (0.3:0.7:1.5). **f,** PID2:PC₇₁BM (1:1.5).

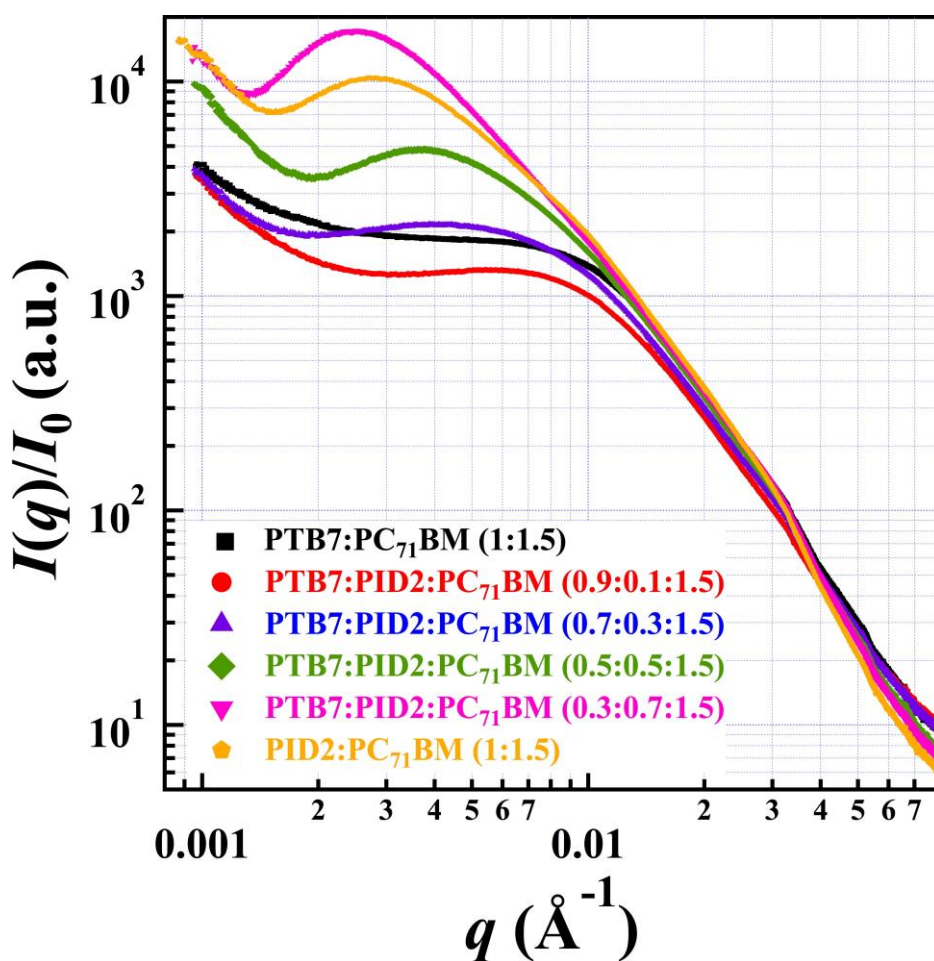


Figure 15 | RSoXS profiles of the ternary films.

Archival publications (published) during reporting period:

17. Son, Hae Jung; Carsten, Bridget; Jung, In Hwan; Yu, Luping, “[Overcoming efficiency challenges in organic solar cells: rational development of conjugated polymers](#) Full Text”, *Energy & Environmental Science* (2012), 5(8), 8158-8170. DOI: [10.1039/C2EE21608F](#)
18. Shengwen Yuan, Desiree White, Alex Mason, Briana Repogle, Magali S. Ferrandon, Luping Yu, Di-Jia Liu, **Improving Hydrogen Adsorption Enthalpy Through Coordinatively**

- Unsaturated Cobalt in Porous Polymers**, *Macromolecular Rapid Communication*, **2012**, 33(5), 407-413, DOI: [10.1002/marc.201100797](https://doi.org/10.1002/marc.201100797).
19. Zhuo Wang, Shengwen Yuan, Alex Mason, Briana Repogle, Di-Jia Liu, and Luping Yu, “**Nanoporous Porphyrin Polymers for Gas Storage and Separation**”, *Macromol.*, (2012), 45(18), 7413-7419. DOI: 10.1021/ma301426e
 20. Luyao Lu, Zhiqiang Luo, Tao Xu, Luping Yu **Cooperative Plasmonic Effect of Ag and Au Nanoparticles on Enhancing Performance of Polymer Solar Cells**”, *Nano Lett.*, 13, 59-64, 2013. DOI: [10.1021/nl3034398](https://doi.org/10.1021/nl3034398), Published: JAN 2013
 21. Hae Jung Son, Luyao Lu, Wei Chen, Tao Xu, Tianyue Zheng, Bridget Carsten, Joseph Strzalka, Seth B. Darling, Lin X. Chen and Luping Yu, **Synthesis and Photovoltaic Effect of Semi-Ladder-Conjugated Polymers with High Solar Cell Efficiencies**, *Adv. Mater.*, (2013), 25(6), 838-843. DOI: [10.1002/adma.201204238](https://doi.org/10.1002/adma.201204238), Published: FEB 13 2013.
 22. Jens Niklas, Kristy L. Mardis, Brian P. Banks, Gregory M. Grooms, Andreas Sperlich, Vladimir Dyakonov, Mario Leclerc, Tao Xu, Luping Yu, Oleg G. Poluektov, “**Highly-Efficient Charge Separation and Polaron Delocalization in Polymer-Fullerene Bulk-Heterojunctions: A Comparative Multi-Frequency EPR & DFT Study**”, *Physical Chemistry Chemical Physics*, (2013), 15 (24), 9562 – 9574, DOI: [10.1039/C3CP51477C](https://doi.org/10.1039/C3CP51477C).
 23. Luyao Lu, Tao Xu, Ju Min Lee, Zhiqiang Luo, Feng He, Hyung Il Park, In Hwan Jung, Sang Ouk Kim, Luping Yu, “**The Role of N-Doped Multi-wall Carbon Nanotubes in Achieving Highly Efficient Polymer Bulk Heterojunction Solar Cells** ”, *Nano Lett.*, 2013, 13 (6), pp 2365–2369, DOI: [10.1021/nl304533j](https://doi.org/10.1021/nl304533j), May 2, 2013.
 24. Shengwen Yuan, Jiang-Lan Shui, Lauren Grabstanowicz, Chen Chen, Sean Comment, Briana Repogle, Tao Xu, Luping Yu and Di-Jia Liu **Highly-Active and “Support-free” Oxygen Reduction Catalyst Prepared from Porous Polyporphyrin**, *Angewandte Chemie Engl. Ed.* 125 (32), 8507-8511, (2013), DOI: [10.1002/ange.201302924](https://doi.org/10.1002/ange.201302924).
 25. Jodi M. Szarko, Brian S. Rolczynski, Sylvia J. Lou, Tao Xu, Joseph Strzalka, Tobin J. Marks, Luping Yu, and Lin X. Chen, **Photovoltaic Function and Exciton/Charge Transfer Dynamics in a Highly Efficient Semiconducting Copolymer**, *Adv. Functional Mater.* 24 (1), 10-26, (2014). DOI: [10.1002/adfm.201301820](https://doi.org/10.1002/adfm.201301820)
 26. Luyao Lu, Luping Yu, **Polymers for solar cells**, *Encyclopedia for Polymeric Nanomaterials*, 2014, 1-9.
 27. Luyao Lu, Tao Xu, Wei Chen, Erik S. Landry, Luping Yu, **Ternary blend polymer solar cells with enhanced power conversion efficiency**, *Nature Photonics*, 8, 716–722, (2014), doi:10.1038/nphoton.2014.172
 28. Tao Xu, Luyao Lu, Tianyue Zheng, Jodi M. Szarko, Lin X. Chen, Luping Yu, **Tuning the Polarizability in the Solar Cell Polymers with Artificial Sweetener Thiophenesacchrin**, *Adv Functional Mater.*, **2014**, 22, 3432-3437. DOI: [10.1002/adfm.201303688](https://doi.org/10.1002/adfm.201303688)
 29. Tao Xu and Luping Yu, **How to design low band gap polymers for highly efficient organic solar cells**, *Materials Today*, 17 (1), 11-15 (2014). <http://dx.doi.org/10.1016/j.mattod.2013.12.00>
 30. Yu-Che Hsiao, Huidong Zang, Ilia Ivanov, Tao Xu, Luyao Lu, Luping Yu, and Bin Hu, **Dielectric Interface Effects on Surface Charge Accumulation and Collection towards High-Efficiency Organic Solar Cells**, *J. of Applied Phys.* 115, 154506 (2014). [<http://dx.doi.org/10.1063/1.4871466>]
 169. In Hwan Jung, Wai-Yip Lo, Jaeyoung Jang, Wei Chen, Donglin Zhao, Erik S. Landry, Luyao Lu, Dmitri V. Talapin, Luping Yu, **Search for Design Principles of Electron Accepting Polymers for All-Polymer Solar Cells**, *Chem. Mater.*, 2014, 26 (11), pp 3450–3459, DOI: 10.1021/cm500832h

31. Luyao Lu, and Luping Yu, **Understanding low bandgap polymer PTB7 and optimizing polymer solar cells based on it**, *Adv. Mater.*, 2014, 26, 4413-4430, doi:10.1002/adma.201400384.
32. Rolczynski, Brian; Szarko, Jodi; Son, Hae Jung; Yu, Luping; Chen, Lin X, **Effects of Exciton Polarity in Charge Transfer Polymer/PCBM Bulk Heterojunction Films**, *J Phys. Chem. Lett.*, 2014, 5, 1856–1863. dx.doi.org/10.1021/jz5005957
33. Luyao Lu, Tao Xu, In Hwan Jung, Luping Yu, **Match the interfacial energy levels between hole transport layer and donor polymer to achieve high solar cell performance**, *J. Phys. Chem. C.*, 2014, 118 (40), pp 22834–22839. DOI: 10.1021/jp5036663.
34. Tianyue Zheng, Luyao Lu, Nicholas E. Jackson, Sylvia J. Lou, Lin X. Chen and Luping Yu, **The Roles of Quinoidal Character and Regioregularity in Determining the Optoelectronic and Photovoltaic Properties of Conjugated Co-polymers**, *Macromol.*, 2014, 47 (18), pp 6252–6259, DOI: 10.1021/ma501152v
35. Wai-Yip Lo, Wuguo Bi, In Hwan Jung, and Luping Yu, **Edge-on Gating Effect in Molecular Transistor**, *Nano. Lett.*, *Submitted*.

Changes in research objectives, if any: None

Change in AFOSR program manager, if any: None

Extensions granted or milestones slipped, if any: None

Include any new discoveries, inventions, or patent disclosures during this reporting period (if none, report none): 1

Luping Yu and Haejung Son, “SEMICONDUCTING POLYMERS”, PCT Application Pending.

Final Report for
Dr. Charles Lee
AFOSR 2015.
Grant number: FA9550-12-1-0061

Yue Wu, School of Chemical Engineering, Purdue University, 480 Stadium Mall Drive, West Lafayette,
IN 47907-2100

Under the support of AFOSR, we have made a revolutionary experimental and theoretical breakthrough in developing nanocomposite-based thermoelectric materials. We have successfully achieved the large-scale production of ultrathin thermoelectric nanowires at up to tens of grams level with superior properties compared to conventional bulk materials, mainly due to enhanced phonon scattering to lower the thermal conductivity and the improvement of power factor by blocking the minority carriers or low energy charge carriers. We also invented the direct coating of advanced thermoelectric nanomaterials onto flexible fibers for integrated flexible thermoelectric. Even without complicated process and high temperature annealing, our flexible thermoelectric systems have demonstrated a great potential for device application with performance comparable or better than the complicated, expensive, and rigid conventional devices. In the three-year period, 14 research papers have been published or accepted for publication on high-impact journals including 3 invited reviews/opinions, 20 conference/symposium presentations including 5 invited presentations, and 12 invited colloquium/seminar series presentations at top tier universities. Prof. Wu was also selected as “2014 Emerging Investigators” by Journal of Materials Chemistry A (Royal Society of Chemistry) to recognize the very best work from materials chemists in the early stages of their independent career.

Summary of Research Progress:

- (1) Developing the mass production capability of producing ultrathin nanowires - in this research, we have developed a low-temperature low-cost atmosphere-pressure solution-phase production of ultrathin thermoelectric nanowires with diameter around or below 10nm with narrow size distribution. Unlike all the previous research in the field of nanowires where only milligrams of nanowires can be produced in one batch of synthesis, now we can continuously produce tens of grams of these nanowires within two hours and these nanowires show better performance compared to the bulk material (Publications #10 and #11).
- (2) Developing experimental approach and theoretical modeling to understand electrical and thermal conductivity in one-dimensional material – by design and incorporating secondary-phase nano-inclusions through the nanowire heterostructure approach, we have achieved a rational control to fabricate nanocomposite with predictable electrical and thermal properties. Especially by using the secondary-phase to scatter the phonons to lower thermal conductivity and using energy filtering and minority carrier blocking to improve power factor and block the unwanted bipolar transport, we have demonstrated a key step forward towards low-cost solution-processable nanomaterials without heavy doping level for high-performance thermoelectric energy harvesting (Publications #1, #3, #9, 312, #14).

- (3) Fiber-based flexible thermoelectric materials and devices – fibers can be produced in a continuous, fully automatic, cheap, and scalable way. They can also conform to curved surfaces to form energy harvesting devices for waste heat recovery. We have developed the method, through the collaboration with Wright-Patterson Air Force Research Lab to investigate the thermal conductivity in the axial direction of glass fibers coated with lead telluride (PbTe) nanocrystals using the self-heated 3ω method particularly at low frequency. We also developed the effective doping method to achieve n-type PbTe nanocrystal and proof-of-concept thin-film thermoelectric modules have also been fabricated using both p-type and n-type PbTe nanocrystals for the conversion of thermal energy into electrical energy. More importantly, through the careful investigation of the surface-bound molecules, we have come up with the theory that we can use these molecules to enhance the power factor and lower the thermal conductivity to achieve significant improvement in performance to surpass the existing bulk materials for thermoelectric devices operating at low temperature (Publications #5 and #7).

Appendix

Publications:

1. Zhang, Genqiang; Fang, Haiyu; Yang, Haoran; Jauregui, Luis A.; Chen, Yong P.; **Wu, Yue*** Design Principle of Telluride-based Nanowire Heterostructures for Potential Thermoelectric Applications. *Nano Letters* (Impact factor 13.025), **2012**, 12, 3627-3633.
2. **Wu, Yue***; Finefrock, Scott W.; Yang, Haoran Nanostructured Thermoelectric: Opportunities and Challenges. Invited Opinion, *Nano Energy* (Impact factor 10.211), **2012**, 1, 651-653.
3. Fang, Haiyu; Feng, Tianli; Yang, Haoran; Ruan, Xiulin; **Wu, Yue*** Synthesis and Thermoelectric Properties of Compositional-Modulated Telluride Nanowire Heterostructures. *Nano Letters* (Impact factor 13.025), **2013**, 13, 2058-2063.
4. Yadav, Gautam G.; David, Anand; Favaloro, Tela; Yang, Haoran; Shakouri, Ali; Caruthers, James; **Wu, Yue*** Synthesis and the Investigation of Thermoelectric and Electrochemical Properties of Porous $\text{Ca}_9\text{Co}_{12}\text{O}_{28}$ Nanowires. *Journal of Materials Chemistry* (Impact factor 6.101), **2013**, 1, 11901-11908.
5. Finefrock, Scott W.; Wang, Yan; Ferguson, John B.; Ward, James V.; Fang, Haiyu; Pfluger, Jonathan E.; Dudis, Douglas S.; Ruan, Xiulin*; **Wu, Yue*** Measurement of thermal conductivity of PbTe nanocrystal coated glass fibers by the 3ω method. *Nano Letters* (Impact factor 13.025), **2013**, 13, 5006-5012.
6. Fang, Haiyu; **Wu, Yue*** "Telluride Nanowire and Nanowire Heterostructure-based Thermoelectric Energy Harvesting", Invited Feature Article for 2014 Emerging Investigators Themed Issue, *Journal of Materials Chemistry A* (Impact Factor 6.101), **2014**, 2, 6004-6014.
7. Fang, Haiyu; Finefrock, Scott W.; **Wu, Yue*** "Effects of Size and Doping on the Power Factor of N-type Lead Telluride Nanocrystals", *Nano Letters* (Impact factor 13.025), **2014**, 14, 1153-1157.
8. Finefrock, Scott W.; Zhang, Genqiang; Bahk, Je-Hyeong; Fang, Haiyu; Yang, Haoran; Shakouri, Ali; **Wu, Yue*** "Structure and thermoelectric properties of spark plasma sintered ultrathin PbTe nanowires", *Nano Letters* (Impact Factor 13.025), **2014**, 14, 3466-3473.
9. Fang, Haiyu; Yang, Haoran; **Wu, Yue*** "Thermoelectric Properties of Silver Telluride-Bismuth Telluride Nanowire Heterostructure Synthesized by Site-

- Selective Conversion”, *Chemistry of Materials* (Impact Factor 8.238), **2014**, 26, 3322-3327.
10. Finefrock, Scott W.; Fang, Haiyu; Yang, Haoran; Darsono, Henka; **Wu, Yue*** “Large-scale solution-phase production of Bi₂Te₃ and PbTe nanowires using Te nanowire templates”, *Nanoscale* (Impact factor 6.233), **2014**, 6, 7872-7876. Cited 1 time.
 11. Yang, Haoran; Finefrock, Scott W.; Caballero, Jonatan D. Albarracin; **Wu, Yue*** “Environmentally benign synthesis of ultra-thin metal telluride nanowires”, *Journal of American Chemical Society*, **2014**, 136, 10242-10245.
 12. Yang, Haoran; Bahk, Je-Hyeong; Day, Tristan; Mohammed, Amr M. S.; Min, Bokki; Snyder, G. Jeffrey; Shakouri, Ali; Wu, Yue* “Solution Phase Synthesis of Ag₂Te Nanowires with Tunable Electrical and Thermal Properties”, *Nano Letters*, **2014**, 14, 5398-5404.
 13. Finefrock, Scott W.; Wu, Yue* “Inorganic Nanostructured Composite-based Thermoelectrics”, invited review for Volume 6 of the Annual Review of Chemical and Biomolecular Engineering, accepted.
 14. Yang, Haoran; Bahk, Je-Hyeong; Day, Tristan; Mohammed, Amr M. S.; Snyder, G. Jeffrey; Shakouri, Ali; Wu, Yue* “Enhanced Thermoelectric Properties in Bulk Nanowire Heterostructure-based Nanocomposites through Minority Carrier Blocking”, *Nano Letters*, accepted.

Conference Presentations:

1. (**Oral Presentation**) “Nanowire Heterostructures for Thermoelectric Energy Harvesting”, 2012 AIChE Meeting, Pittsburgh, PA, October **2012**.
2. (**Oral Presentation**) “Nanowire Heterostructures for Thermoelectric Energy Harvesting”, 2013 MRS Meeting, 2013 MRS Meeting, San Francisco, CA, April **2013**.
3. (**Poster**) “Enhanced ZT due to Energy Filtering Effect in Thermoelectric Nano-composites Based on Facile Solution Phase Synthesis of Dumbbell-like PbTe-Ag₂Te-PbTe Heterostructures”, 2013 MRS Meeting, 2013 MRS Meeting, San Francisco, CA, April **2013**.
4. (**Oral Presentation**) “Complex Metal Oxide Nanowires for Thermoelectric and Battery Applications”, 2013 MRS Meeting, San Francisco, CA, April **2013**.
5. (**Oral Presentation**) “Synthesis and thermoelectric properties of compositional-modulated lead telluride-bismuth telluride nanowire heterostructures”, 2013 ACS Meeting, Indianapolis, IN, September **2013**.
6. (**Oral Presentation**) “Solution phase synthesized dumbbell-like PbTe-Ag₂Te heterostructures with enhanced Seebeck coefficient for thermoelectric applications”, 2013 ACS Meeting, Indianapolis, IN, September **2013**.
7. (**Oral Presentation**) “Complex metal oxide nanowires for thermoelectric and battery applications”, 2013 ACS Meeting, Indianapolis, IN, September **2013**.
8. (**Oral Presentation**) “PbTe nanocrystal coated glass fiber for thermoelectric energy harvesting”, 2013 ACS Meeting, Indianapolis, IN, September **2013**.
9. (**Oral Presentation**) “Nanowire Heterostructure-Based Thermoelectric”, AIChE Meeting, San Francisco, CA, November 2013.
10. (**Oral Presentation**) “Complex Metal Oxide Nanowires for Thermoelectric and Battery Applications”, 2013 AIChE Meeting, San Francisco, CA, November 2013.
11. (**Oral Presentation**) “Flexible Fiber-Based Thermoelectric Energy Harvesting and Motion Sensing”, 2014 MRS Meeting, San Francisco, CA, April 2014.

12. (**Oral Presentation**) “Mass Production of Telluride-Based Nanowires and Nanowire Heterostructures and Investigation of Their Thermoelectric Properties”, 2014 MRS Meeting, San Francisco, CA, April 2014.
13. (**Oral Presentation**) “Environmentally Benign Synthesis of Ultra-Thin Metal Telluride Thermoelectric Nanowires”, 2014 AIChE Meeting, Atlanta, GA, November 2014.
14. (**Oral Presentation**) “Mass Production of Ultrathin Nanowires and Nanowire Heterostructures for Thermoelectric Applications”, 2014 MRS Meeting, Boston, MA, December 2014.
15. (**Oral Presentation**) “Nanocomposite-Based Flexible Thermoelectric Devices”, 2014 MRS Meeting, Boston, MA, December 2014.
16. (**Invited Presentation**) “Advanced Nanostructures for Thermoelectric Energy Harvesting”, American Vacuum Society Annual Meeting, Tampa, FL, November **2012**.
17. (**Invited Presentation**) “Nanowire and Nanowire Heterostructures for Thermoelectric Energy Harvesting”, Japan Nano 2013, Tokyo, Japan, February **2013**.
18. (**Invited Presentation**) “Advanced Nanostructured Thermoelectric Materials for Waste Heat Recovery”, ACS Meeting, Indianapolis, IN, September **2013**.
19. (**Invited Presentation**) “Advanced Nanocomposite Fibers for Thermoelectric Energy Harvesting and Motion Sensing”, 2013 AIChE Meeting, San Francisco, CA, November **2013**.
20. (**Invitation Accepted**) “Chalcogenide Nanowire and Nanowire Heterostructure Based Bulk Nanocomposite Thermoelectrics”, 2015 MRS Meeting, San Francisco, CA

Invited Colloquium/Seminar Series Presentations:

1. “Advanced Nanostructured Thermoelectric Materials for Waste Heat Recovery”, Northwestern University, July **2013**.
2. “Advanced Nanostructured Thermoelectric Materials for Waste Heat Recovery”, Carnegie Mellon University, August **2013**.
3. “Advanced Nanostructured Thermoelectric Materials for Waste Heat Recovery”, University of Pittsburgh, September **2013**.
4. “Advanced Nanostructured Thermoelectric Materials for Waste Heat Recovery”, University of Illinois at Urbana Champaign, October **2013**.
5. “Advanced Nanostructured Thermoelectric Materials for Waste Heat Recovery”, Stanford University, October **2013**.
6. “Advanced Nanostructured Thermoelectric Materials for Waste Heat Recovery”, University of Washington, December **2013**.
7. “Advanced Nanostructured Thermoelectric Materials for Waste Heat Recovery”, University of California at Berkeley, January **2014**.
8. “Advanced Nanostructured Materials for Energy Conversion and Storage”, University of Florida, January **2014**.
9. “Advanced Nanostructured Materials for Energy Conversion and Storage”, Iowa State University, February **2014**.
10. “Advanced Nanostructured Materials for Energy Conversion and Storage”, University of Colorado, April 2014.
11. (**Invitation Accepted**) “Advanced Nanostructured Materials for Energy Conversion and Storage”, University of Chicago.
12. (**Invitation Accepted**) “Advanced Nanostructured Materials for Thermoelectric Energy Conversion”, University of California at Riverside.

REPORT DOCUMENTATION PAGE				Form Approved OMB No. 0704-0188	
Public reporting burden for this collection of information is estimated to average 1 hour per response, including the time for reviewing instructions, searching existing data sources, gathering and maintaining the data needed, and completing and reviewing this collection of information. Send comments regarding this burden estimate or any other aspect of this collection of information, including suggestions for reducing this burden to Department of Defense, Washington Headquarters Services, Directorate for Information Operations and Reports (0704-0188), 1215 Jefferson Davis Highway, Suite 1204, Arlington, VA 22202-4302. Respondents should be aware that notwithstanding any other provision of law, no person shall be subject to any penalty for failing to comply with a collection of information if it does not display a currently valid OMB control number. PLEASE DO NOT RETURN YOUR FORM TO THE ABOVE ADDRESS.					
1. REPORT DATE (DD-MM-YYYY) 01-03-2015		2. REPORT TYPE Final Report		3. DATES COVERED (From - To) 01-04-2012 - 31-03-2015	
4. TITLE AND SUBTITLE Photochemical control of electronic, optic, catalytic, mechanic, biological and electrochemical properties of organic materials based on photo-induced proton transfer				5a. CONTRACT NUMBER	
				5b. GRANT NUMBER FP048956	
				5c. PROGRAM ELEMENT NUMBER	
6. AUTHOR(S) Yi Liao				5d. PROJECT NUMBER	
				5e. TASK NUMBER	
				5f. WORK UNIT NUMBER	
7. PERFORMING ORGANIZATION NAME(S) AND ADDRESS(ES) Florida Institute of Technology 150 W University Blvd Melbourne FL 32901				8. PERFORMING ORGANIZATION REPORT	
9. SPONSORING / MONITORING AGENCY NAME(S) AND ADDRESS(ES) AF OFFICE OF SCIENTIFIC RESEARCH 875 N. RANDOLPH ST. ROOM 3112 ARLINGTON VA 22203				10. SPONSOR/MONITOR'S ACRONYM(S) AFOSR	
				11. SPONSOR/MONITOR'S REPORT NUMBER(S)	
12. DISTRIBUTION / AVAILABILITY STATEMENT Approved for Public Release, Distribution is Unlimited					
13. SUPPLEMENTARY NOTES					
14. ABSTRACT Photo-controlled reversible proton transfer has been studied as a general method for developing various smart materials. A novel type of photoacid, i.e. metastable-state photoacid, was developed as a bridge between photon and proton. Unprecedented change of proton concentration under visible light has been achieved using this type of photoacid. Photo-controlled acid-catalyzed reactions, volume-change hydrogels, polymer conductivity, bacterial killing, fragrance release, color, and phase change have been demonstrated. These results show that metastable-state photoacids are useful tools for controlling proton transfer processes with light and developing various photoresponsive materials.					
15. SUBJECT TERMS Photoresponsive materials, photoacid, proton transfer					
16. SECURITY CLASSIFICATION OF:			17. LIMITATION OF ABSTRACT SAR	18. NUMBER OF PAGES	19a. NAME OF RESPONSIBLE PERSON Dr. Charles Lee
a. REPORT Unclassified	b. ABSTRACT Unclassified	c. THIS PAGE Unclassified			19b. TELEPHONE NUMBER (include area code) (703) 696-7779

1.0 Summary

The objective of this project is to utilize photo-induced proton transfer as a general method to develop different smart materials that alter their properties under irradiation. The photo-induced proton transfer is controlled by a novel type of photoacid, i.e. metastable-state photoacid, which was discovered by our group.

Metastable-state photoacid can reversibly produce large proton concentration under moderate irradiation (sunshine, LED light etc.) and so far no other type of molecule can achieve this. In this project, we showed that metastable-state photoacids can be generally designed by linking an electron-accepting moiety and a nucleophilic moiety with a double bond, and the nucleophilic moiety needs to have an active proton. Irradiation induces a trans-cis isomerization of the double bond, which allows a nucleophilic cyclization reaction to occur between the two moieties and releases the active proton. Over 40 metastable-state photoacids with different photo- and thermo-activities have been synthesized during the project. Unprecedented change of proton concentration ($\Delta\text{pH} \sim 5$) under visible light has been achieved.

Visible light controlled proton transfer processes have been demonstrated by our group using metastable-state photoacid as a bridge between photon and proton. In general, metastable-state photoacids were added to acid or pH sensitive systems, and the properties, including chemical, biological, catalytic, electronic, optic, geometric and mechanic properties, of the resulting systems can be altered by turning on and off irradiation. In this project, photo-controlled acid-catalyzed reactions, volume-change hydrogels, polymer conductivity, bacterial killing, fragrance release, color, and phase change have been achieved.

In addition, several other groups have utilized the photoacids we reported in the development of novel polymer sensor, molecular switch, microbial fuel cell and supramolecular gel, which shows that photo-controlled proton transfer using metastable-state photoacids is indeed a useful approach towards various photoresponsive systems.

2.0 Introduction

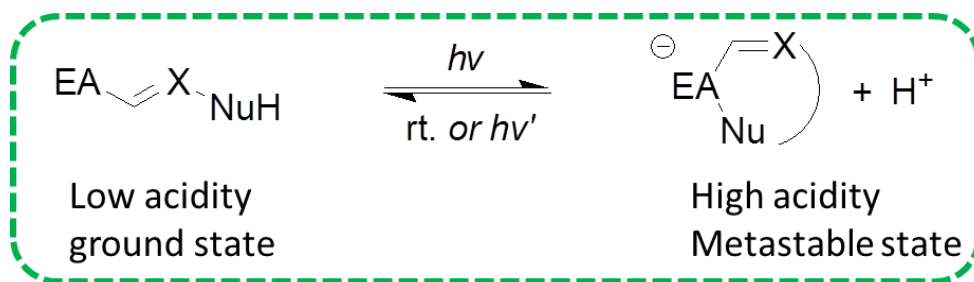
Proton transfer is one of the most fundamental processes in nature and numerous chemical, material, and biological processes are driven by proton transfer. For example, biological systems use proton gradient as an energy form to synthesize energetic chemicals for their biological functions; many organic reactions are catalyzed by Brønsted acids; and many materials have pH-sensitive properties. In fact, searching Scifinder Scholar data base with the key words “proton transfer” resulted in more than 47000 references, and “pH sensitive” resulted in more than 15000 references. This project is regarding a general method for controlling proton transfer processes with light, and utilizing this method to develop smart materials that alter their properties under irradiation.

A photoacid that undergoes proton dissociation upon photo-irradiation can work as a bridge between a photon and a proton, and thus allows photo-control of proton-transfer process. So far, three types of photoacids have been reported, which are photoacid generator (PAG), excited-state photoacid, and metastable-state photoacid discovered by our group. PAGs are irreversible and thus can only initiate a proton transfer process but not stop or reverse it. Excited state photoacids, although are reversible, cannot produce a large proton concentration, while most proton transfer processes are driven by a high proton concentration. Only metastable-state photoacids can reversibly produce a large proton concentration, and moderate visible light from e.g. sunshine or LED is enough to induce the change. Incorporating metastable-state photoacids into pH or acid sensitive systems will allow remote, temporal and spatial control of their properties with visible light

In this project, a general scheme for designing metastable-state photoacids was studied; metastable-state photoacids with different structures were synthesized and their physicochemical properties were studied; photoresponsive materials based on proton transfer were developed.

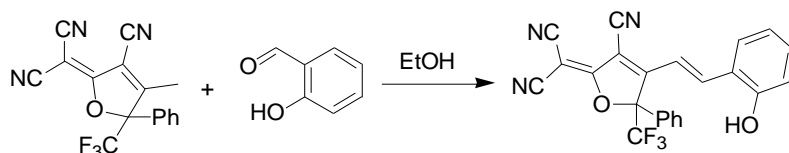
2.0 Methods, Assumptions and Procedures

Metastable-state photoacids can be generally designed by linking an electron-accepting moiety and a nucleophilic moiety with a double bond, and the nucleophilic moiety needs to have an active proton. (Scheme 1) Irradiation induces a trans-cis isomerization of the double bond, which allows a nucleophilic cyclization reaction to occur between the two moieties and releases the active proton. The high-acidity state resulted from irradiation is a metastable-state, which relaxes to the ground state in the dark and takes back the proton. Specific structures of the photoacids developed based on this scheme are given in the next section.



Scheme 1. Design of metastable-state photoacids.

The photoacids are synthesized by Knoevenagel reactions between the corresponding electron accepting moiety with a methyl group and the nucleophilic moiety with an aldehyde in ethanol. Ammonium acetate was sometimes added as the catalyst. An example is shown in Scheme 2.



Scheme 2. An example of the synthesis of a metastable-state photoacid.

Photoactivity was studied by monitoring the UV-Vis absorption change of a photoacid in water, ethanol and DMSO under irradiation. Narrow bandwidth visible light LEDs with a photon flux density of $\sim 1000 \mu\text{mol m}^{-2}\text{s}^{-1}$ were used as the light sources in most cases. For those photoacids with very fast reverse reaction, an OmniCure S1500 system was used. Quantum yields were calculated from the results. The reverse reaction was studied by monitoring the UV-Vis absorption after the irradiation was turned off, and the data were fit to a second order kinetic equation to obtain the rate constants. Change of proton concentration (pH) was evaluated by measuring pH of a solution of a photoacids before and upon/after irradiation. Water is a preferred solvent when the solubility of a photoacid in water is close to or higher than 1 mM. Small amount of DMSO or ethanol was often mixed with water to improve the solubility. Cycles of UV-Vis absorption and pH change were obtained by turning on and off the irradiation for several times and recording the absorbance or pH values.

Photoresponsive systems were prepared by mixing or covalently linking metastable-state photoacids with the targeting systems. The concentration of the photoacid was optimized so that the proton concentration generated by irradiation is large enough to induce significant property change.

A photoacid with a suitable reverse rate was selected for a certain system so that a desirable switching rate can be achieved. For organic materials, a proton transfer moiety or additive was often required to achieve a good performance. The photoresponsive systems developed in this project and the corresponding property changes are described in the next section.

3.0 Results and Discussion

3.1 Metastable-state photoacids developed during the project

As described in the last section, metastable-state photoacids can be designed based on Scheme 1. Different types of electron acceptor moieties and nucleophilic moieties have been identified as suitable components for constructing metastable-state photoacids, which are listed in Figure 1. Over 40 photoacids have been synthesized during this project. Although a systematic work for fully understanding the structure-property relationship is still undergoing, useful information have been obtained and photoacids with desirable properties have been identified.

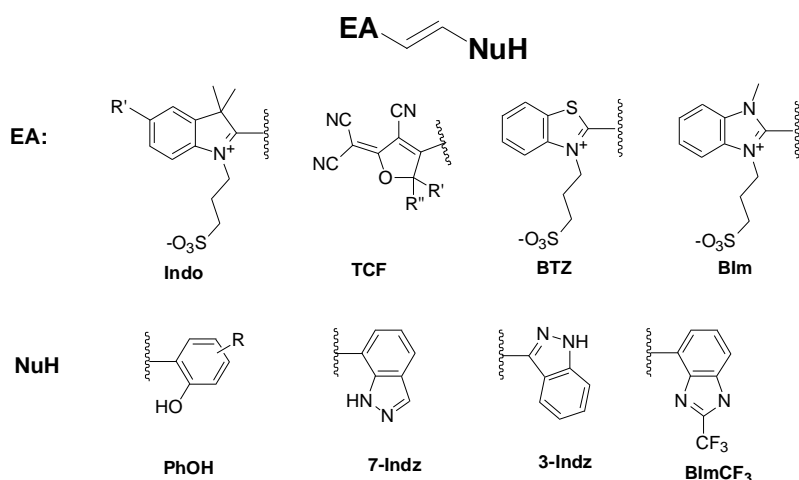


Figure 1. Electron acceptor moieties and nucleophilic moieties that have been used for constructing metastable-state photoacids.

Among the different types of metastable-state photoacids, the Indo-PhOH type has been extensively studied. In fact, the first metastable-state photoacid was a Indo-PhOH (**1** in Table 1), and all the photoresponsive systems based on metastable-state photoacids by far (See next section) used this type photoacid. The Indo-PhOH photoacids synthesized during the project are listed in Table 1. Study showed that electron donating groups including alkyl- and alkoxy groups on either PhOH or Indo moiety can lower the dark acidity and improve the stability of the molecules, and thus should be used. On the contrary, electron withdrawing groups should be avoided unless

necessary. Functional groups on PhOH side that are electron donating to the bridging double bond increase the reverse reaction rate significantly. Organic solvents or polymers with low hydrogen bond donor (HBD) acidity (Taft–Kamlet α scale) slow down the reverse reaction. However, it was found later that this rule is not true for other type of photoacids. Not all the Indo-PhOH molecules designed are photoactive. Molecule **24** is not photoactive, which was attributed to a low-lying triplet state, which deactivates the photo-induced trans-cis isomerization. None of the Indo-PhOH photoacids can be used in basic condition including PBS buffer (pH 7.4) due to deprotonation followed by thermo-induced cyclization in the dark.

Table 1. Indo-PhOH type photoacids synthesized

	1	2	3	4	5	6	7	8	9	10	11	12	13	14	15	16	17	18	19	20
R ₆	H	H	H	H	H	H	H	H	H	H	H	H	H	OMe	H	H	H	H	H	H
R ₅	H	H	Me	NO ₂	CO ₂ H	NO ₂	H	H	H	OH	OCOCHCH ₂	H	OMe	H	H	Me	OMe	OC ₁₈ H ₃₇	H	H
R ₄	H	OMe	H	H	H	H	H	H	OH	H	H	H	H	OMe	Me	Me	OMe	H	OC ₁₂ H ₂₅	H
R ₃	H	H	H	H	H	OMe	OMe	OH	H	H	H	Me	H	H	H	H	H	H	H	H
R _{5'}	H	H	H	H	H	H	H	H	H	H	H	H	H	H	H	H	H	H	H	OMe

21

22

23

24

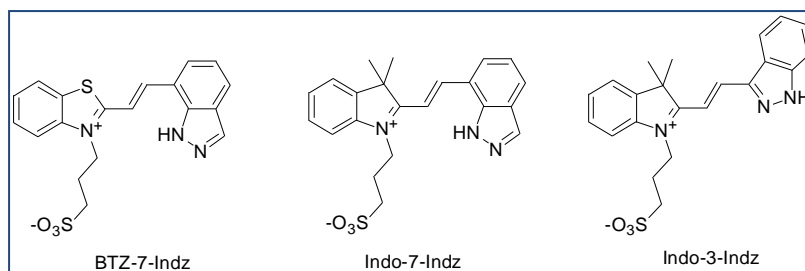
Photoacid **1** in Table 1 was the first metastable-state photoacid discovered and has been extensively studied. This photoacid possesses a high quantum yield of 0.37 and a moderate reverse reaction rate of $73 \text{ M}^{-1} \text{ s}^{-1}$ in water. It can reversibly change the proton concentration over 100 times under blue light (400-500 nm). Most of the applications demonstrated by our group and other groups used this photoacids. However, the reverse reaction of **1** in organic polymers is too slow for many applications and it decomposes slowly in water. Photoacid **2** in Table 1 has a reverse reaction rate ~ 2 orders of magnitudes higher than that of **1** and is stable in water. Therefore, photoacid **2** is considered as a better choice in many cases. Most of the Indo-PhOH can only work under blue light

while a longer activating wavelength is desirable of biological applications. Photoacid **23** absorbs at longer wavelength (λ_{max} 536 nm) than the others and can function under green light (525 nm). As mentioned above, Indo-PhOH type photoacids cannot function under basic condition, which substantially limits their applications in material and biological areas. Recently, we found that a BTZ-7-Indz photoacid (inserted figure) worked well in PBS buffer and thus can be applied to common biological systems. Indo-Indz (inserted figure) molecules are *basic photoacids*. They take protons in the dark and release protons under light, which results in a very large change of proton concentration. A pH change of 5 was recently demonstrated by our group.

3.2 Photoresponsive systems developed using metastable-state photoacids

The following photoresponsive systems have been achieved by our group:

Switching on and off an acid catalyzed reaction. Fisher



Esterification reaction is a textbook reaction that is often catalyzed by strong acid such as sulfuric acid. We have shown that when a metastable-state photoacid was added to a mixture of acetic acid and ethanol, the esterification reaction can be turned on by visible light and stopped by turning off the light. This demonstration showed that metastable-state photoacids can be applied to control acid-catalyzed reactions.

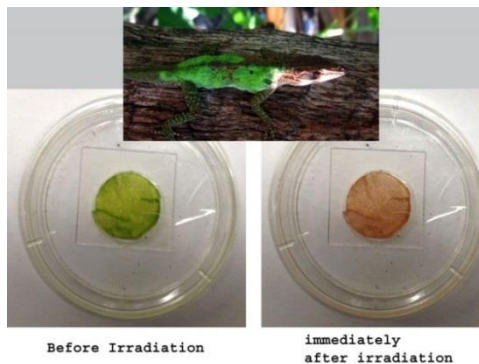
Visible-light controlled odor release material.

Development of digital scent technology will add another dimension to electronic industry. While significant



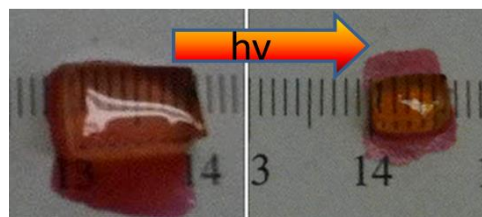
progress has been made in the area, the lack of a successful commercial product after half-century of development indicates challenges of fulfilling the requirements for commercialization. We have developed a material composed of a metastable-state photoacid and an acid-sensitive polymer. It can release fragrant under visible light with selective wavelengths and quickly stop releasing after the light is turned off. This material may be used for digital scent technology for quick switching among different odors and reducing the size of the device.

Highly tailorable photochromic material. Although photochromic compounds have been studied for decades, they often show color changes between white and a color. Changes between two colors, for example green to red, are very difficult (if possible) using conventional photochromic compounds. Combining metastable-state photoacids with pH indicators make the design of



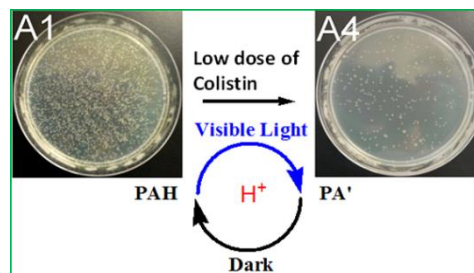
photochromic material with various color changes simple. The color change and the stimulating wavelength can be controlled by choosing different indicators and photoacids. Various color changes, e.g. yellow to blue, green to red, etc. have been demonstrated in solutions and polymer films under sunshine or LED light. Complicated visual effects such as multiple color changes can be achieved as well. One of the potential applications is dynamic camouflage coating.

Photo-responsive hydrogel that changes volume and mechanic strength under irradiation can be used to control valves, cantilevers etc. in micro-devices, and as novel biomedical materials. We demonstrated that combining a pH sensitive hydrogel and metastable-state photoacids



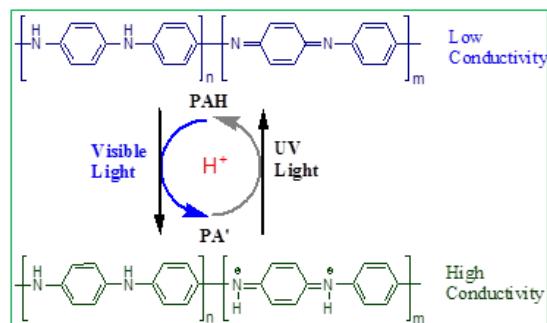
resulted in a hydrogel that greatly changed its volume under visible light. Thin films of such material have also been prepared and their volume and mechanical changes upon irradiation is under study.

Visible-light induced killing of bacterial mediated by metastable-state photoacids has been demonstrated. Experiments showed that a metastable-state photoacid killed 99% of a multidrug-resistant bacteria under visible light. Combining a metastable-state photoacid with colistin, which is a highly effective but somewhat toxic



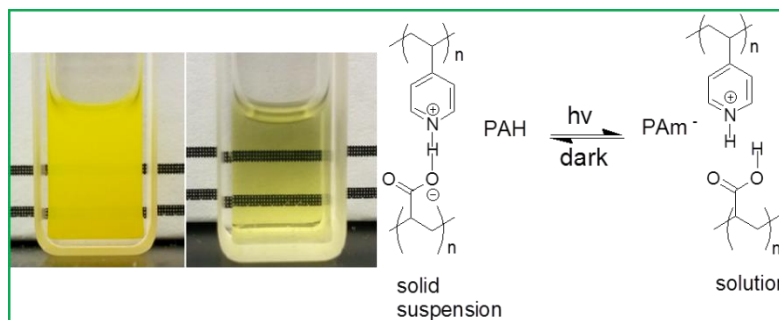
drug, significantly lowered the dose of colistin required for killing bacteria and thus increased its safety. These results showed that metastable-state photoacids can function in biological system. They may lead to sunlight-powered antibacterial coatings and novel phototherapeutic method.

Photo-switchable conducting material has been investigated. Composites of polyaniline and metastable-state photoacids were turned to a high-conductivity state after irradiation of visible light and switched back to a low conductivity state by UV irradiation. Several cycles of conductivity switch were demonstrated, but the conductivity change was



limited to ~ 1 fold. Fundamental study shows that the metastable-state photoacids used for the experiment, which were Indo-PhOH type photoacids, cannot function under the strong basic condition of polyaniline. Indazole type photoacids described in the last section are currently investigated due to their compatibility with basic conditions.

Photo-controlled ionic and hydrogen bonding between polymers. Controlling interactions between polymers and molecules with light has great potential in development of smart materials. Polyacrylic acid and polyvinyl pyridine form hydrogen bonding and ionic bonding between each other, which crosslink the two polymers. We showed that the crosslinking can be turned off by light in the presence of a metastable-state photoacid. A reversible phase change between solid suspension (in the dark) and solution (under light) have been demonstrated. Controlling crosslinking allows altering material properties with a small loading of a photoacid and thus is a promising approach for development of photoresponsive materials.



Recently, the metastable-state

photoacids reported by our group have been utilized by other groups for different purposes. For example, novel supramolecular gel (Maity et al. *Angew. Chem. Int. Ed.* 2015, 54, 998–1001), polymer sensor (Johns et al. *Anal Chem.* 2014, 86, 6184–7.) molecular switch (Tatum et al. *J. Am. Chem. Soc.* 2014, 136, 17438–17441), and microbial fuel cell (Bao et al. *RSC Adv.* 2014, 4, 27277–27280) using photoacid **1** in Table 1 have been reported in the last couple of years, which shows that photo-controlled proton transfer using metastable-state photoacids is indeed a useful approach that can be generally applied to various systems.

4.0 List of publications

4.1 Publications in Peer Reviewed Journals:

1. Chen, Hongbin, Liao, Yi, Photochromism based on reversible proton transfer, *J. Photochem. Photobio., A*: (2015), 300, 22-26.
2. Wang, Zhuozhi; Johns, Valentine K.; Liao, Yi, Controlled Release of Fragrant Molecules with Visible Light. *Chem. Eur. J.* (2014), 20(45), 14637-14640.
3. Chen, Hong-bin; Abeyrathna, Nawodi; Liao, Yi Alkyne-azide cycloaddition catalyzed by a dinuclear copper(I) complex, *Tetrahedron Lett.* (2014), 55(48), 6575-6576.
4. Johns, Valentine K.; Peng, Ping; DeJesus, Joseph; Wang, Zhuozhi; Liao, Yi Visible-Light-Responsive Reversible Photoacid Based on a Metastable Carbanion, *Chem. Eur. J.* (2014), 20(3), 689-692.
5. Johns, Valentine K.; Wang, Zhuozhi; Li, Xinxue; Liao, Yi, Physicochemical Study of a Metastable-State Photoacid, *J. Phys. Chem. A.* (2013), 117(49), 13101-13104.
6. Peng, Ping; Wang, Chaoming; Shi, Zheng; Johns, Valentine K.; Ma, Liyuan; Oyer, Jeremiah; Copik, Alicja; Igarashi, Robert; Liao, Yi Visible-light activatable organic CO-releasing molecules (PhotoCORMs) that simultaneously generate fluorophores. *Org. Biomol. Chem.* (2013) 11, 6671-6674.
7. Alber, Candace; Shi, Zheng; Johns, Valentine; Lafave, Sarah; Liao Yi Photo-induced Protonation and Conductivity of Polyaniline/Poly(ethylene glycol) and Polyaniline/[Poly(ethylene glycol)-grafted Polyaniline] Composites. *J. Appl. Poly. Sci.* (2013) 129, 3546-3550.
8. Luo, Yang; Wang, Chaoming; Peng, Ping; Hossain, Mainul; Jiang, Tianlun; Fu, Weiling; Liao, Yi, Ming Su Visible light mediated killing of multidrug-resistant bacteria using photoacids *J. Mater. Chem. B*, (2013)1, 997-1001.

4.2 Patent:

1. Liao, Yi, Photoacid compositions having extended lifetime of proton dissociation state. US 13/748,253.

4.3 Presentations and Proceedings:

1. Liao, Yi. Photo-control of pH-driving processes with reversible metastable-state photoacids. The 248th ACS National Meeting & Exposition, 2014.

2. Liao, Yi. Visible-light responsive materials based on metastable-state photoacids. The 3rd European Symposium of Photopolymer Science, 2014.
3. Liao, Yi. Visible-light responsive materials based on photo-induced proton transfer. AFOSR Organic Materials Chemistry Portfolio Review, 2014.
4. Alber, Candace; Shi, Zheng; Johns, Valentine; Lafave, Sarah; Liao, Yi Photo-induced protonation and conductivity of polyaniline/poly(ethylene glycol) and polyaniline/[poly(ethylene glycol)-grafted polyaniline] composites. Abstracts of Papers, 245th ACS National Meeting & Exposition, (2013), PMSE-327.
5. Shi, Zheng; Peng, Ping; Johns, Valentine K.; Liao, Yi. Novel photo-switchable conducting materials based on a reversible photoacid and polyaniline. Polymer Preprints (2012), 53(2), 125-126.
6. Johns, Valentine K.; Liao, Yi. Synthesis of visible light responsive reversible photoacid polymers. Polymer Preprints (2012), 53(2), 255-256.